Nucleon-nucleon scattering process in Lattice Chiral Effective Field Theory approach up to next-to-next-to-next-to-leading order

Dissertation

zur

Erlangung des Doktorgrades (Dr. rer. nat.)

der

Mathematisch-Naturwissenschaftlichen Fakultät

der

Rheinischen Friedrich-Wilhelms-Universität Bonn

von

Dechuan Du

aus

Tianjin, China

Bonn, 29.01.2018

Dieser Forschungsbericht wurde als Dissertation von der Mathematisch-Naturwissenschaftlichen Fakultät der Universität Bonn angenommen und ist auf dem Hochschulschriftenserver der ULB Bonn http://hss.ulb.uni-bonn.de/diss_online elektronisch publiziert.

1. Gutachter:	Prof. Dr. Ulf-G. Meißner
2. Gutachter:	Prof. Dr. Thomas Luu
Tag der Promotion:	05.04.2018
Erscheinungsjahr:	2018

ABSTRACT

We carry out a comprehensive analysis of the neutron-proton interaction up to the third order in the scheme of chiral effective field theory on the lattice. The complete two-pion exchange potential is taken into account to allow for a variation of the lattice spacing. We analyze the perturbative as well as the non-perturbative inclusion of the higher-order corrections and present a thorough analysis of the theoretical uncertainties.

In addition, a first attempt is made to include chiral contributions at the fourth order as well as the electromagnetic effects relevant for proton-proton scattering. For that, we include all fourth order local four-nucleon interactions and the dominant corrections to the two-pion exchanges. As expected, the higher order chiral corrections give an improved description for the scattering of two nucleons. This work should be extended by performing an uncertainty analysis and investigating the lattice spacing dependence in the future.

We further scrutinize nuclei with even and equal numbers of protons and neutrons using nuclear lattice effective field theory, based upon a set of highly improved (smeared) leading order interactions. We present numerical evidence that reveals a first-order transition at zero temperature from a Bose-condensed gas of alpha particles to the nuclear liquid, which is regulated by the strength and locality of the nucleon-nucleon interactions.

Contents

1 Introduction 1

2 Chiral Perturbative Theory and Nuclear Interactions 5

2.1 Chiral Symmetry . . . 5

2.2 Symmetry Breaking . . . 8

2.3 Chiral Lagrangian for Nuclear Interactions . . . 8

2.3.1 Chiral Effective Field Theory . . . 8

2.3.2 Hierarchy of Nuclear Force . . . 8

2.3.3 Leading Order Interations . . . 10

3 Lattice Methods 11

3.1 Lattice Conventions . . . 12

3.2 Chiral Effective Field Theory on the Lattice . . . 13

3.2.1 Nucleonic Fields on the Lattice . . . 15

3.2.2 Mesonic Fields on the Lattice . . . 17

3.2.3 Interactions on the Lattice: One-Pion Exchange and Transfer Matrix Operator . 19

3.2.4 Interactions on the Lattice: First Order Contact Interactions and Auxillary Fields 23

3.3 Interactions on the Lattice: Improvement of Contact Interactions . . . 27

3.3.1 High Order Contact Interactions in Position Space . . . 29

3.3.2 Contact Interactions in Spherical Harmonic Basis . . . 33

3.4 Two-Body Scattering on the Lattice . . . 36

3.4.1 Hamiltonian Projection onto the Spherical Harmonic Basis . . . 36

3.4.2 Spherical Wall Method to Determine Phase Shift on the Lattice . . . 37

3.4.3 More on the Spherical Wall Method . . . 39

4 Scattering of Two Nucleons: Numerical Result **41**

4.1 Lattice Notations . . . 42

4.2 Interactions on the Lattice: Improvement of Pion Exchange Potential . . . 45

4.3 Phase Shifts and Mixing Angles to N^2LO . . . 49

4.4 Variation of the Lattice Spacing . . . 56

4.5 Perturbative Treatment of Higher Orders . . . 58

4.6 Further Improvements . . . 64

4.7 Nuclear Binding Energies . . . 66

5 Two-Nucleon Scattering with Coulomb Potential: Numerical Results **69**

5.1 Lattice Notations . . . 70

5.2 Interactions on the Lattice: Coulomb Potential . . . 75

5.3 Neutron-Proton Scattering at N^3LO . . . 76

5.4 Proton-Proton Scattering up to N^3LO . . . 76

6 Nuclear Binding Near A Quantum Phase Transition **81**

6.1 A Leading Order Action with Local and Nonlocal Contact Interactions . . . 81

6.2 Neutron-Proton Scattering . . . 85

6.3 Ground State Engergies of Nuclei . . . 86

6.4 Ground State Energies as A Function of λ . . . 91

7 Summary **95**

Bibliography **97**

A Uncertainty Analysis **105**

B Two-Pion Exchange Potential **107**

C Contact Interactions in Spherical Harmonics Basis in Position Space **111**

List of Figures **115**

List of Tables **119**

Acronyms **121**

CHAPTER 1

Introduction

Atomic nuclei are complex, interacting many-body systems composed of protons and neutrons, which can be regarded as different isospin projections of a single particle, the nucleon. While a qualitative understanding of the properties of atomic nuclei can be reached by means of phenomenological descriptions of nucleons exchanging mesons (preferentially pions), any systematically improvable theoretical framework should account for the fact that the nucleons and pions themselves are composite particles, made up of quarks that interact by exchange of gauge bosons, referred to as gluons. The theory of quarks and gluons, quantum chromodynamics (QCD), has so far presented a formidable task for analytical methods that have been extremely successful for the weak and electromagnetic interactions. This situation is particularly troublesome at low energies, where quarks and gluons are confined and the running QCD coupling α_s becomes large. This has prompted the emergence of lattice Monte Carlo (MC) simulations of QCD (lattice QCD), whereby the properties of baryons and mesons (referred to collectively as hadrons) are extracted by stochastical methods on a discretized space-time lattice.

Since the emergence of lattice QCD in the 1980's, algorithms and computer hardware have evolved to the point where lattice QCD simulations are able to provide an accurate description of the properties of isolated hadrons, as well as of hadronic interactions (for instance meson-meson scattering) at low energies. Nevertheless, lattice QCD for nucleonic few- and many-body systems remains very challenging, as such simulations require pion masses M_π close to the physical value, and lattices significantly longer in each dimension than can be accommodated on presently available computers. Another significant

computational challenge is the exponentially unfavorable signal-to-noise ratio in simulations at large baryon number. In this situation, further progress can be made by working directly with theoretical frameworks written in terms of the composite degrees of freedom (nucleons and pions) on the hadronic level. However, care must be taken such that the connection to the fundamental theory (QCD) is not lost. Here, we will focus on the framework of chiral effective field theory (χEFT), which provides a systematically improvable, *a*b initio description of the nuclear forces, which is expressed in terms of a low-momentum expansion, valid below the chiral symmetry restoration scale $\Lambda_\chi \simeq 1$ GeV of QCD.

Given the nuclear Hamiltonian of χEFT, a choice has to be made as to the numerical methods by which the properties of nuclei are computed. For systems with four nucleons or less, a semi-analytic approach is provided by the Faddeev-Yakubovsky integral equations, and the nuclear lattice Hamiltonian may also be diagonalized exactly by numerical Lanzcos methods. However, for systems composed of more than four nucleons, methods such as MC simulations or basis-truncated eigenvector methods are required, due to the unfavorable scaling of Lanczos methods with nucleon number A. Here, we shall focus on combining the lattice MC approach with nuclear χEFT. This allows us to use efficient numerical methods already developed within lattice QCD and condensed matter physics, such as auxiliary-field transformations, pseudofermion methods, and non-local configuration updating schemes such as hybrid Monte Carlo (HMC). It should be noted that at each order in the χEFT expansion, a number of unknown short-range couplings appear, in addition to contributions from long-range one-pion exchange (OPE), two-pion exchange (TPE),... At a given lattice spacing (which functions as the momentum cut-off or regulator of the effective field theory (EFT)), these unknown coefficients can be determined by a least-squares fit of the lattice action to available data for the $A = 2$ and $A = 3$ systems (such as neutron-proton (np) scattering phase shifts and mixing angles). For $A \geq 4$, we may use these short-distance couplings in lattice MC calculations in order to obtain testable predictions for a wide range of light and medium-heavy atomic nuclei.

In the first part of this thesis, we show how to efficiently compute np phase shifts and mixing angles using an improved spherical wall method, which allows for an accurate and straightforward calculation at center-of-mass (CM) momenta close to the momentum cutoff, as well as for high angular momentum partial waves, where the Lüscher method popular in the lattice QCD community becomes increasingly cumbersome. Our method uses an "auxiliary potential" to modify the shape and strength of the spherical hard-wall boundary, which enables the discrete energy eigenvalues to be continuously shifted, and furthermore allows for a unique determination of the scattering phase shifts and mixing

angles in the Stapp parameterization. Our spherical wall method is also applicable to so-called adiabatic projection calculations, whereby a cluster Hamiltonian (for instance for alpha-alpha scattering) is computed numerically by MC simulation of χEFT. We also take the first steps in extending the lattice χEFT to next-to-next-to-next-to-leading order / NNNLO (N^3LO), by including the N^3LO two-nucleon operators in our analysis of np scattering. Finally, we extend our analysis to include the electromagnetic and isospin-breaking (IB) effects in proton-proton (pp) scattering.

In the second part of this thesis, we discuss how χEFT can be extended to account for medium-heavy nuclei in a competitive way. In this context, it should be noted that several other choices (besides nuclear lattice EFT) are routinely made for the nuclear forces and calculational methods used to describe interacting low-energy protons and neutrons. For $A = 3$ and $A = 4$, several studies have used the Nijmegen [1], CD-Bonn [2], and AV18 [3] two-nucleon forces, together with the Tucson-Melbourne [4] and Urbana-IX [5] three-nucleon forces. Light nuclei and neutron matter have also been extensively studied using these phenomenological potentials within the Green's Function MC and auxiliary-field diffusion MC methods. In addition to MC methods, a notable approach is the no-core shell model (NCSM), which produces approximate eigenvectors in a reduced vector space. The NCSM method has been applied to light nuclei both in terms of phenomenological potential models, as well as nuclear forces derived from χEFT. In this situation, the main advantages of lattice χEFT is the favorable $\sim A^2$ scaling with nucleon number, and the completely *ab initio* treatment of nuclear interactions and nucleon configurations. The main challenge of nuclear χEFT is to control the sign oscillations (akin to the infamous "sign problem" in MC simulations) of the MC probability weight for large A, and when the number of neutrons significantly exceeds the number of protons (so-called neutron-rich nuclei).We show that this can be achieved with a novel lattice formulation of the nuclear Hamiltonian, whereby a combination of locally and non-locally smeared operators are used.

This thesis is organized as follows: In Sec. 2, the chiral symmetry of the strong interactions and the emerging χEFT is briefly reviewed, with an eye on the nuclear Hamiltonian. In Sec. 3, the pertinent lattice methods are discussed. The nuclear Hamiltonian is rewritten in discrete variables and its is shown how on deals with nucleon-nucleon scattering in such a framework. Sec. 4 contains the results for np scattering up to next-to-next-to-leading order / NNLO (N^2LO) with a full inclusion of the leading two-pion exchange. In Sec. 5, results at N^3LO are displayed, in particular the inclusion of the Coulomb interaction in the pp systems is presented. Then, in Sec. 6, a novel leading order (LO) action is presented that shows promise to address nuclei up to the mid-mass region. Sec. 7 contains a short summary and

outlook.

CHAPTER 2

Chiral Perturbative Theory and Nuclear Interactions

2.1 Chiral Symmetry

QCD has achieved a great success in describing the interactions of quarks and gluons in the high-energy ($\Lambda \gg 1$ GeV) regime. It constitutes the strong interaction part of the so-called standard model (SM). The QCD Lagrangian has the form

$$\mathcal{L}_{\rm QCD} = \bar{q}(i\gamma_\mu D^\mu - \mathcal{M})q - \frac{1}{4}\mathcal{G}^a_{\mu\nu}\mathcal{G}^{a\mu\nu} \tag{2.1}$$

$$= \mathcal{L}^0_{\rm QCD} - \bar{q}\mathcal{M}q\,, \tag{2.2}$$

where $D_\mu = \partial_\mu - ig_s G^a_\mu \lambda^a$, with λ^a the SU(3) Gell-Mann matrices acting on the color space. Its algebra satisfies

$$[\lambda^a, \lambda^b] = if^{abc}\lambda^c\,, \tag{2.3}$$

with the structure constants f^{abc}. The quark field has Dirac μ, color a, and flavor f indices, which is written as $q^a_{\mu f}$.

The mass matrix M in flavor space is

$$\mathcal{M} = \mathrm{diag}(m_u, m_d, m_s, \cdots) \,. \tag{2.4}$$

G^a_μ is the gluon field. It serves to connect of the quark fields in spacetime. For the sake of building a gauge invariant action, we define the gluon field strength tensor as

$$\mathcal{G}^a_{\mu\nu} = \partial_\mu G^a_\nu - \partial_\nu G^a_\mu + g_s f^{abc} G^b_\mu G^c_\nu \,. \tag{2.5}$$

u, d, s are the light quarks, usually treated relativistically, while the other quarks (c, b, t) are heavy in the sense of a typical hadronic scale of about 1 GeV, and are not considered here. Light quarks are identical except for their mass and charges.

Using the definitions

$$\begin{aligned} q_\mathrm{R} &= \frac{1}{2}(1+\gamma_5)q \,, \\ q_\mathrm{L} &= \frac{1}{2}(1-\gamma_5)q \,, \end{aligned} \tag{2.6}$$

we rewrite the Lagrangian as follows

$$\mathcal{L}_\mathrm{QCD} = \bar{q}_\mathrm{L} i\not{D} q_\mathrm{L} + \bar{q}_\mathrm{R} i\not{D} q_\mathrm{R} - \bar{q}_\mathrm{L} \mathcal{M} q_\mathrm{R} - \bar{q}_\mathrm{L} c\mathcal{M} q_\mathrm{R} - \frac{1}{4} G^a_{\mu\nu} G^{a\mu\nu} \,, \tag{2.7}$$

$$\mathcal{L}^0_\mathrm{QCD} = \bar{q}_\mathrm{L} i\not{D} q_\mathrm{L} + \bar{q}_\mathrm{R} i\not{D} q_\mathrm{R} - \frac{1}{4} G^a_{\mu\nu} G^{a\mu\nu} \,. \tag{2.8}$$

The left- and right-handed fields are the eigenstates of the chirality operator γ_5 with eigenvalues -1 and 1, respectively. In the limit of vanishing quark mass, the Lagrangian $\mathcal{L}^0_\mathrm{QCD}$ has a global symmetry $\mathrm{SU(3)_L{\times}SU(3)_R{\times}U(1)_V{\times}U(1)_A}$.

According to Noether's theorem, there are 18 conserved currents: nine right-handed

$$R^a_\mu = \bar{q}_\mathrm{R} \gamma_\mu \frac{\lambda^a}{2} q_\mathrm{R} \,, \quad \partial^\mu R^a_\mu = 0 \,, \tag{2.9}$$

and nine left-handed ones,

$$L^a_\mu = \bar{q}_\mathrm{L} \gamma_\mu \frac{\lambda_a}{2} q_\mathrm{L} \,, \quad \partial^\mu L^a_\mu = 0 \,. \tag{2.10}$$

It is instructive to form linear combinations of these terms to obtain nine vector currents

$$V_\mu^a = R_\mu^a + L_\mu^a = \bar{q}\gamma_\mu \frac{\lambda^a}{2} q \,, \quad \partial^\mu V_\mu^a = 0 \,, \tag{2.11}$$

and nine axial-vector currents

$$A_\mu^a = R_\mu^a - L_\mu^a = \bar{q}\gamma_\mu\gamma_5 \frac{\lambda_a}{2} q \,, \quad \partial^\mu A_\mu^a = 0 \,. \tag{2.12}$$

In this manner, 18 conserved charges are obtained,

$$Q_{\mathrm{R}}^a = \int \mathrm{d}^3 x R_0^a \,, \quad \frac{\mathrm{d}Q_{\mathrm{R}}^a}{\mathrm{d}t} = 0 \,, \tag{2.13}$$

$$Q_{\mathrm{L}}^a = \int \mathrm{d}^3 x L_0^a \,, \quad \frac{\mathrm{d}Q_{\mathrm{L}}^a}{\mathrm{d}t} = 0 \,, \tag{2.14}$$

or, equivalently,

$$Q_{\mathrm{V}}^a = \int \mathrm{d}^3 x V_0^a \,, \quad \frac{\mathrm{d}Q_{\mathrm{V}}^a}{\mathrm{d}t} = 0 \,, \tag{2.15}$$

$$Q_{\mathrm{A}}^a = \int \mathrm{d}^3 x A_0^a \,, \quad \frac{\mathrm{d}Q_{\mathrm{A}}^a}{\mathrm{d}t} = 0 \,. \tag{2.16}$$

The algebra of the chiral group $\mathrm{SU(3)_L}\times\mathrm{SU(3)_R}$ is generated,

$$[Q_{\mathrm{R}}^a, Q_{\mathrm{R}}^b] = i f^{abc} Q_{\mathrm{R}}^c \,, \quad [Q_{\mathrm{L}}^a, Q_{\mathrm{L}}^b] = i f^{abc} Q_{\mathrm{L}}^c \,, \quad [Q_{\mathrm{R}}^a, Q_{\mathrm{L}}^b] = 0 \,. \tag{2.17}$$

For Q_{V}^a and Q_{A}^a, the commutation relations are

$$[Q_{\mathrm{V}}^a, Q_{\mathrm{V}}^b] = i f^{abc} Q_{\mathrm{V}}^c \,, \quad [Q_{\mathrm{A}}^a, Q_{\mathrm{A}}^b] = i f^{abc} Q_{\mathrm{V}}^c \,, \quad [Q_{\mathrm{V}}^a, Q_{\mathrm{A}}^b] = i f^{abc} Q_{\mathrm{A}}^c \,. \tag{2.18}$$

Note that the quark number symmetry $\mathrm{U(1)_V}$ is realized as the baryon number operator, while the axial $\mathrm{U(1)_A}$ is broken at the quantum level due to the axial anomaly.

2.2 Symmetry Breaking

The QCD Lagrangian is approximately invariant, namely in the limit of vanishing quark mass, under global chiral $SU(3)_L \times SU(3)_R$ transformations in flavor space. Chiral symmetry is broken explicitly due to the nonvanishing quark masses. Even with zero quark masses, QCD is spontaneously broken to the isospin group $SU(3)_V$ due to the formation of a quark condensate $\langle q\bar{q} \rangle$. The Nambu-Goldstone theorem predicts massless boson modes in this case, which are identified as the pions, kaoens and etc. of the theory. This is called spontaneous symmetry breaking. It means that the symmetry of the Lagrangian is not exactly realized in the groud state of the system.

2.3 Chiral Lagrangian for Nuclear Interactions

2.3.1 Chiral Effective Field Theory

As described above, χEFT is a low-energy effective theory of QCD where pions and nucleons are explicit degrees of freedom. It provides a theoretical framework for organizing the low energy interactions in powers of particle momenta. It is systematic, model-independent and based upon a local SU(3) gauge symmetry in the instrinsic color space. In the case of nuclear interactions, there are two different types of contributions. First, the one- and two-pion exchanges can be related to pion-nucleon scattering and thus this type of contribution is entirely fixed [6]. In addition, there are short-range interactions, whcih come with unknown low-energy constant (LEC)s. These new LECs must be determined from a fit to nuclear systems. For more details, see the review [7].

2.3.2 Hierarchy of Nuclear Force

The low-energy effective theory of QCD is constructed by identifying all operators that respect the underlying symmetries of QCD, and to use the relavant separation of scales to derive a hierarchy in such operators. This hierarchy is manifest in a power-counting scheme, typically demarcated as LO, next-to-leading order (NLO), and so on. As pointed out by Weinberg [8], in systems with two or more nucleons, the power counting does not apply to the T-matrix but rather to the interaction potential, as the

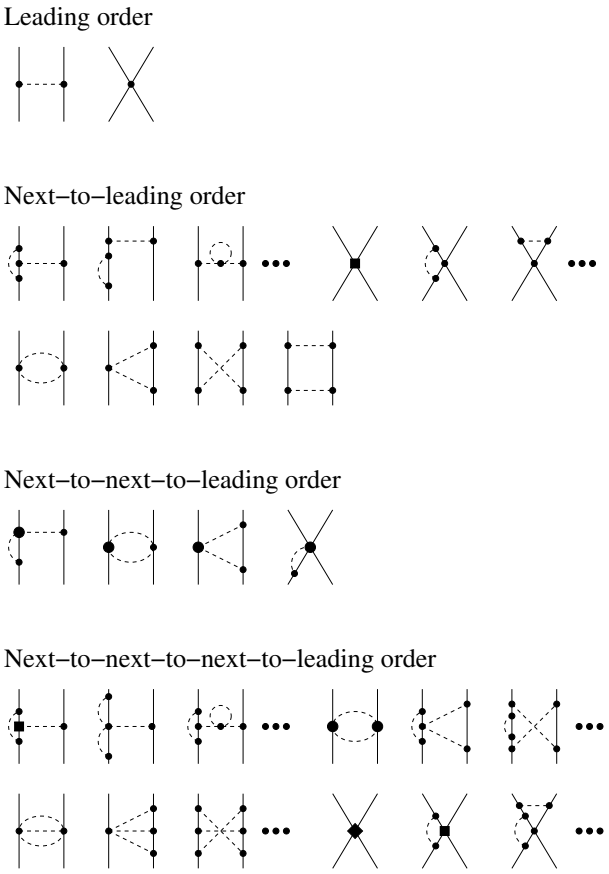

Figure 2.1: Chiral expansion of the two-nucleon force. Here solid/dashed lines denote nucleons/pions. The interactions of different dimensions are depicted by different symbols, see Ref. [7] for details.

nuclons in nuclei behave non-relativistically. The corresponding expansion takes the form:

$$\begin{aligned} V &= V_{\rm ct} + V_{1\pi} + V_{2\pi} + V_{3\pi} + \cdots \\ &= V_{\rm ct}^{(0)} + V_{1\pi}^{(0)} \\ &\quad + V_{\rm ct}^{(2)} + V_{1\pi}^{(2)} + V_{2\pi}^{(2)} \\ &\quad\quad + V_{1\pi}^{(3)} + V_{2\pi}^{(3)} \\ &\quad + V_{\rm ct}^{(4)} + V_{1\pi}^{(4)} + V_{2\pi}^{(4)} + V_{3\pi}^{(4)} + \cdots \end{aligned} \tag{2.19}$$

Note that three-body interations first appear at N^{2}LO. In Weinberg's scheme, the EFT power counting is equivalent to dimensional analysis for irreducible diagrams.

In the context of χEFT, one can study the potential systematically in powers of particle momenta p/Λ, where Λ is the typically around 500 MeV.

$$V = V^{(\rm NN)} + V^{(\rm 3N)} + V^{(\rm 4N)} + \cdots \,, \tag{2.20}$$

$$V = V^{(0)} + V^{(2)} + V^{(3)} + V^{(4)} \cdots , \tag{2.21}$$

$$V = V_{\text{ct}} + V_{1\pi} + V_{2\pi} + V_{3\pi} \cdots . \tag{2.22}$$

In this thesis, we will concentrate to the nucleon-nucleon / 2N / two-nucleon (NN) potential.

2.3.3 Leading Order Interations

Here, we briefly discuss the LO potential based on the Weinberg power counting. It consists of the long-ranged OPE potential and two four-nucleon terms without derivatives. All these terms count as $(p/\Lambda)^0$. The higher order contributions are given succesively in the course of this thesis.

One-Pion Exchange Potential

In momentum space, the static OPE potential takes the form

$$V_{1\pi}^{pp} = V_{1\pi}^{nn} = V_{1\pi}(M_{\pi^0}) , \tag{2.23}$$

$$V_{1\pi}^{np} = -V_{1\pi}(M_{\pi^0}) + 2(-1)^{I+1} V_{1\pi}(M_{\pi^\pm}) , \tag{2.24}$$

where I denotes the total isopin of the NN system and

$$V_{1\pi}(M_\pi) = -\left(\frac{g_{\text{A}}}{2f_\pi}\right)^2 \boldsymbol{\tau}_1 \cdot \boldsymbol{\tau}_2 \, \frac{\boldsymbol{\sigma}_1 \cdot \mathbf{q} \boldsymbol{\sigma}_2 \cdot \mathbf{q}}{\mathbf{q}^2 + M_\pi^2} . \tag{2.25}$$

Here, $\mathbf{q}$ is the transfer between initial and final relative momentum of the two nucleons. g_{A}, f_π, M_π are nucleon axial-vector constant, the pion decay constant and the pion mass, respectively. Their numerical values will be given later.

Contact Interactions without Derivatives

The LO four-nucleon contact interactions are given by

$$V_{\text{NN}}^{(0)} = \frac{1}{2} C_0 \, (N^\dagger N)^2 + \frac{1}{2} C_{\text{I}} \, (N^\dagger \tau N)^2 \tag{2.26}$$

in terms of the LECs C_0 and C_{I}. These must be determined form a fit to the NN system.

CHAPTER 3

Lattice Methods

Lattice field theory, born in the 70's after the pioneering work by K.G. Wilson [9] has become an important method in theoretical physics. With the great advancements of supercomputing resources, the growth of the field has been accelerated in recent years. The theoretical and numerical methods used in lattice field theory have been applied to many fields of physics: particle physics, field theory, statistical physics, condensed matter physics and non-linear phenomena. The lattice method used in Lattice field theory is a kind of regularization scheme of quantum field theory (QFT) which puts the quantum field on a space-time cubic lattice with some lattice spacing a, In this system the theory has a natural momentum cutoff $p_{\max} \sim 1/a$, so that the ultraviolet divergence problem can be avoided. Physical observables are extracted from the partition funtion via the Path Integral based upon first principles. Lattice field theory is a non-perturbative method.

QCD describes the strong interaction in the context of the SM. Here quarks and gluons are the explicit degrees of freedom, and the theory's non-perturbative behavior in the low-energy regime (< 1 GeV) is a big challenge. On the other hand, Lattice EFT, using nucleons as degrees of freedom, is applied to few- and many-body systems in low-energy nuclear physics. It combines lattice methods with the principles of χEFT described in the previous chapter. In this manner, we can build a self-consistent formalism on a lattice, which I describe below in more detail.

3.1 Lattice Conventions

A lattice means a $(3,1)$-dimensional (hyper-)cubic box, with a spatial lattice spacing a and a temporal spacing a_t. It spans L lattice spacings along each spatial direction and L_t temporal spacings along the fourth axis. A dimensionless parameter α_t is defined as a_t/a, which indicates an asymmetric lattice in terms of time and is used in our calculations. We make use of $n_\mathrm{s} = (n_\mathrm{x}, n_\mathrm{y}, n_\mathrm{z})$ to label integer-valued lattice sites along the 3-dimensional spatial axis, while n_t denotes the number of Euclidean time steps and $n = (n_\mathrm{s}, n_\mathrm{t})$ denoting the (3,1)- lattice site. In the corresponding Brillouin momentum space, $k_\mathrm{s} = (k_\mathrm{x}, k_\mathrm{y}, k_\mathrm{z})$ denotes some integer-valued momentum with a unit $\tilde{a} = 2\pi/La$ and $k = (k_\mathrm{s}, k_\mathrm{t})$ with a unit $\tilde{a}_\mathrm{t} = 2\pi/L_\mathrm{t}a_\mathrm{t}$ for k_t.

Here and in what follows, the symbol 'hat', when applied to variables, implies that they are dimensionless, that means a quantity is expressed in appropriate powers of the lattice spacing. In terms of derivatives, the symbol 'hat' refers to the finite differece approximation of the derivative in continuum so that $\hat{\nabla}_\mu = (a\nabla_i, a_\mathrm{t}\nabla_0)$. A common differencing scheme employed in lattice QCD is the symmetric forward-backward difference,

$$\hat{\nabla}_i f(x) = \frac{1}{2}\left[f\left(x + a\hat{i}\right) - f\left(x - a\hat{i}\right)\right] \ , \hat{\nabla}_0 f(x) = \frac{1}{2}\left[f\left(x + a_\mathrm{t}\hat{0}\right) - f\left(x - a_\mathrm{t}\hat{0}\right)\right] \ ,$$
$$\hat{\nabla}_i^2 f(x) = f\left(x + a\hat{i}\right) + f\left(x - a\hat{i}\right) - 2f(x) \ , \hat{\nabla}_0^2 f(x) = f\left(x + a_\mathrm{t}\hat{0}\right) + f\left(x - a_\mathrm{t}\hat{0}\right) - 2f(x) \ .$$

However, this definition deviates from the ideal one and induces an error originating from the finite lattice spacing. An improved method to deal with this systematic error uses higher order finite differences

$$\hat{\nabla}_l f(n) = \frac{1}{2}\sum_{j=1}^{\nu+1}(-)^{j+1}\theta_j\left[f(n + j\hat{l}) - f(n - j\hat{l})\right]\left[1 + O(a^{2\nu+2})\right] \ , \tag{3.1}$$

$$\hat{\nabla}_l^2 f(n) = -\sum_{j=0}^{\nu+1}(-)^{j}\omega_j\left[f(n + j\hat{l}) + f(n - j\hat{l})\right]\left[1 + O(a^{2\nu+2})\right] \tag{3.2}$$

with the hopping coefficients θ_j and ω_j in the Table 3.1 and $l = \{1,2,3\}$. An order ν of hopping coefficients indicates $O(a^{2\nu})$-improved. We use a standard plane-wave function $\exp\left[i\,2\pi k_\mathrm{s}\cdot n_\mathrm{s}/L\right]$ as a test acting on the differece operator

$$-i\,\hat{\nabla}_l \exp\left(i\frac{2\pi}{L}k_\mathrm{s}\cdot n_\mathrm{s}\right) = \left[\sum_{j=1}^{\nu+1}(-)^{j+1}\theta_j \sin\left(j\frac{2\pi}{L}[k_\mathrm{s}]_l\right)\right]\exp\left(i\frac{2\pi}{L}k_\mathrm{s}\cdot n_\mathrm{s}\right) + O(a^{2\nu+3}) \ ,$$

Table 3.1: Hopping coefficients ω_j and θ_j for ν-order of finite difference

ν	$\omega_0^{(\nu)}$	$\omega_1^{(\nu)}$	$\omega_2^{(\nu)}$	$\omega_3^{(\nu)}$	$\omega_4^{(\nu)}$
0	1	1	0	0	0
1	5/4	4/3	1/12	0	0
2	49/36	3/2	3/20	1/90	0
3	205/144	8/5	1/5	8/315	1/560
ν		$\theta_1^{(\nu)}$	$\theta_2^{(\nu)}$	$\theta_3^{(\nu)}$	$\theta_4^{(\nu)}$
0		1	0	0	0
1		4/3	1/6	0	0
2		3/2	3/10	1/30	0
3		8/5	2/5	8/105	1/140

$$-\frac{1}{2}\hat{\nabla}_l^2 \exp\left(i\frac{2\pi}{L}k_s \cdot n_s\right) = \left[\sum_{j=0}^{\nu+1}(-)^j\omega_j \cos\left(j\frac{2\pi}{L}[k_s]_l\right)\right]\exp\left(i\frac{2\pi}{L}k_s \cdot n_s\right) + O(a^{2\nu+4}) \,.$$

As a result, we obtain the correction of the physical momentum on a lattice

$$\frac{2\pi}{L}[\hat{k}_s]_l = \sum_{j=1}^{\nu+1}(-)^{j+1}\theta_j \sin\left(j\frac{2\pi}{L}[k_s]_l\right) \,, \tag{3.3}$$

$$\frac{1}{2}\left(\frac{2\pi}{L}[\hat{k}_s]_l\right)^2 = \sum_{j=0}^{\nu+1}(-)^j\omega_j \cos\left(j\frac{2\pi}{L}[k_s]_l\right) \,. \tag{3.4}$$

It should be mentioned that this correction depends on the definition of the discretized derivative.

3.2 Chiral Effective Field Theory on the Lattice

In chiral perturbation theory (χPT), and in particular χEFT, Lagrangians are expanded in increasing powers of pion masses and small momenta. Lattice χEFT is developed from the chiral expansion of the QCD Lagrangian. The LO Lagrangian contributes mostly to the χEFT whereas higher orders are perturbatively suppressed. The Lagrangian density at lowest order in χEFT scheme reads

$$\begin{aligned}\mathcal{L} = &\frac{1}{2}\partial_\mu\pi^I\partial^\mu\pi^I - \frac{1}{2}M_{\pi,I}^2\pi^I\pi^I + N^\dagger i\partial_0 N + N^\dagger\frac{\nabla^2}{2m_N}N \\ &- \frac{g_A}{2f_\pi}N^\dagger\tau^I\,\sigma_i\nabla_i\pi^I N - \frac{1}{2}C_0(N^\dagger N)(N^\dagger N) - \frac{1}{2}C_I(N^\dagger\tau^I N)(N^\dagger\tau^I N) \,.\end{aligned} \tag{3.5}$$

which is divided into three sectors: the free mesons and nucleons, as well as the interaction part. Here N is the nucleon field with spin and isospin indices, and the pion field π takes an isospin index. $\boldsymbol{\sigma}$ and $\boldsymbol{\tau}$ are Pauli matrics in spin and isospin space respectively, and repeated indices are implicitly summed over. Meanwhile, we write down the corresponding action

$$S = S_{\mathrm{b}} + S_{\mathrm{f}} + S_{\mathrm{int}} , \tag{3.6}$$

where

$$S_{\mathrm{b}} = \int \mathrm{d}^4x \left[\frac{1}{2}\partial_\mu \pi^I \partial^\mu \pi^I - \frac{1}{2} M_{\pi,I}^2 \pi^I \pi^I \right] , \tag{3.7}$$

$$S_{\mathrm{f}} = \int \mathrm{d}^4x \, N^\dagger \left[i\partial_0 + \frac{\nabla^2}{2m} \right] N , \tag{3.8}$$

$$S_{\mathrm{int}} = S_{\pi\mathrm{N}} + S_{\mathrm{NN}} , \tag{3.9}$$

$$S_{\pi\mathrm{N}} = \int \mathrm{d}^4x \left[-\frac{g_{\mathrm{A}}}{2f_\pi} N^\dagger \tau^I \, \sigma_i \nabla_i \pi^I N \right] , \tag{3.10}$$

$$S_{\mathrm{NN}} = \int \mathrm{d}^4x \left[-\frac{1}{2} C_0 (N^\dagger N)(N^\dagger N) - \frac{1}{2} C_{\mathrm{I}} (N^\dagger \tau^I N)(N^\dagger \tau^I N) \right] . \tag{3.11}$$

In the following sections, we build up the lattice version for this action. It is convienent to perform a Wick rotation, $t = x^0 \to -i\tau = -ix_0^{\mathrm{E}}$, so that one has a representation of the field theory in Euclicean space and the connection between the field theory and statistical physics is constructed. The rule of Wick rotation is

$$x^\mu = (x^0, \vec{x}) \to (-ix_0^{\mathrm{E}}, x_i^{\mathrm{E}}) , \tag{3.12}$$

$$x_\mu = (x_0, -\vec{x}) \to (-ix_0^{\mathrm{E}}, -x_i^{\mathrm{E}}) , \tag{3.13}$$

$$\partial_\mu = (\partial_0, \partial_i) \to (i\partial_0^{\mathrm{E}}, \partial_i^{\mathrm{E}}) , \tag{3.14}$$

$$\partial^\mu = (\partial_0, -\partial_i) \to (i\partial_0^{\mathrm{E}}, -\partial_i^{\mathrm{E}}) , \tag{3.15}$$

$$\mathrm{d}^4x \to -i\mathrm{d}^4x^{\mathrm{E}} , \tag{3.16}$$

where the upper letter ‘E’ indicates Euclicean space.

3.2.1 Nucleonic Fields on the Lattice

In continuious Minkowski space-time, the action of the free nucleonic fields reads

$$\begin{aligned} S_{\mathrm{f}}[N, N^{\dagger}] &= \int \mathrm{d}^4 x\, N^{\dagger}(x)(i\partial_0 + \frac{\nabla^2}{2m_{\mathrm{N}}})N(x) \\ &= \int (-i)\mathrm{d}^4 x^{\mathrm{E}}\, N^{\mathrm{E}\dagger}(x^{\mathrm{E}})(-\partial_0^{\mathrm{E}} + \frac{\nabla^{\mathrm{E}}\nabla^{\mathrm{E}}}{2m_{\mathrm{N}}})N^{\mathrm{E}}(x^{\mathrm{E}}) \\ &= i\left[\int \mathrm{d}^4 x^{\mathrm{E}}\, N^{\mathrm{E}\dagger}(x^{\mathrm{E}})\left(\partial_0^{\mathrm{E}} - \frac{\nabla^{\mathrm{E}}\nabla^{\mathrm{E}}}{2m_{\mathrm{N}}}\right)N^{\mathrm{E}}(x^{\mathrm{E}})\right], \end{aligned} \tag{3.17}$$

where

$$N^{\mathrm{E}}(x^{\mathrm{E}}) = N(x)\,, \quad N^{\mathrm{E}\dagger}(x^{\mathrm{E}}) = N^{\dagger}(x)\,,$$

and we define

$$S_{\mathrm{f}}^{\mathrm{E}}[N^{\mathrm{E}}, N^{\mathrm{E}\dagger}] = \int \mathrm{d}^4 x^{\mathrm{E}}\, N^{\mathrm{E}\dagger}(x^{\mathrm{E}})\left(\partial_0^{\mathrm{E}} - \frac{\nabla^{\mathrm{E}}\nabla^{\mathrm{E}}}{2m_{\mathrm{N}}}\right)N^{\mathrm{E}}(x^{\mathrm{E}})\,. \tag{3.18}$$

so that $S_{\mathrm{f}} = iS_{\mathrm{f}}^{\mathrm{E}}$. We show how to rotate the Minkowski time to Euclicean time in detail and discretize the Euclicean space-time by a replacement

$$x_\mu^{\mathrm{E}} \to (a_{\mathrm{t}}\hat{n}_{\mathrm{t}}, a\hat{n}_i) = a(\frac{1}{\alpha_{\mathrm{t}}}\hat{n}_{\mathrm{t}}, \hat{n}_i)\,, \tag{3.19}$$

$$N^{\mathrm{E}}(x^{\mathrm{E}}) \to N^{\mathrm{E}}(a\hat{n})\,, \quad N^{\mathrm{E}\dagger}(x^{\mathrm{E}}) \to N^{\mathrm{E}\dagger}(a\hat{n})\,, \tag{3.20}$$

$$\int \mathrm{d}^4 x^{\mathrm{E}} \to a_{\mathrm{t}} a^3 \sum_{\hat{n}}\,, \quad \partial_\mu^{\mathrm{E}} = \frac{1}{a}(\frac{1}{\alpha_{\mathrm{t}}}\hat{\partial}_0, \hat{\nabla})\,, \tag{3.21}$$

where $\hat{n} = (\hat{n}_{\mathrm{t}}/\alpha_{\mathrm{t}}, \hat{n}_i)$ and it is dimensionless. As a result,

$$\begin{aligned} S_{\mathrm{f}}^{\mathrm{E}} &= a^3 a_{\mathrm{t}} \sum_{\hat{n}} N^{\mathrm{E}\dagger}(a\hat{n})\left(\frac{1}{a_{\mathrm{t}}}\hat{\partial}_0 - \frac{\hat{\nabla}^2}{2a^2 m_{\mathrm{N}}}\right)N^{\mathrm{E}}(a\hat{n}) \\ &= \alpha_{\mathrm{t}} \sum_{\hat{n}} \hat{N}^{\dagger}(\hat{n})\left(\frac{1}{\alpha_{\mathrm{t}}}\hat{\partial}_0 - \frac{\hat{\nabla}^2}{2\hat{m}_{\mathrm{N}}}\right)\hat{N}(\hat{n})\,, \end{aligned} \tag{3.22}$$

where

$$\hat{N}(\hat{n}) = a^{3/2} N^{\mathrm{E}}(a\hat{n})\,, \quad \hat{N}^{\dagger}(\hat{n}) = a^{3/2} N^{\mathrm{E}\dagger}(a\hat{n})\,, \quad \hat{m}_{\mathrm{N}} = a m_{\mathrm{N}}\,. \tag{3.23}$$

Here we introduce the Grassmann fields η and η^* for nucleons. The Grassmann fields are periodic with respect to the spatial extent of the lattice

$$\begin{aligned} \eta(n_\mathrm{s} + L\hat{x}, n_\mathrm{t}) &= \eta(n_\mathrm{s} + L\hat{y}, n_\mathrm{t}) &&= \eta(n_\mathrm{s} + L\hat{z}, n_\mathrm{t}) &&= \eta(n_\mathrm{s}, n_\mathrm{t}) \,, \\ \eta^*(n_\mathrm{s} + L\hat{x}, n_\mathrm{t}) &= \eta^*(n_\mathrm{s} + L\hat{y}, n_\mathrm{t}) &&= \eta^*(n_\mathrm{s} + L\hat{z}, n_\mathrm{t}) &&= \eta^*(n_\mathrm{s}, n_\mathrm{t}) \,, \end{aligned} \tag{3.24}$$

and antiperiodic along the temporal axis

$$\begin{aligned} \eta(n_\mathrm{s}, n_\mathrm{t} + L_\mathrm{t}) &= -\eta(n_\mathrm{s}, n_\mathrm{t}) \,, \\ \eta^*(n_\mathrm{s}, n_\mathrm{t} + L_\mathrm{t}) &= -\eta^*(n_\mathrm{s}, n_\mathrm{t}) \,. \end{aligned} \tag{3.25}$$

The integral measure is written as $\mathcal{D}\eta\mathcal{D}\eta^*$ for short. η_n and η^*_m denote $\hat{\eta}(\hat{n})$ and $\hat{\eta}^*(\hat{m})$ respectively. Note that the nucleonic field carries spin and isopin index,

$$\mathcal{D}\eta\mathcal{D}\eta^* = \prod_{n_\mathrm{t}n_\mathrm{s},si} \mathrm{d}\eta_{si,n_\mathrm{t}n_\mathrm{s}} \mathrm{d}\eta^*_{si,n_\mathrm{t}n_\mathrm{s}} \,. \tag{3.26}$$

The convention for Grassmann integration is

$$\int \mathrm{d}\eta = \int \mathrm{d}\eta^* = 0 \,, \tag{3.27}$$

$$\int \mathrm{d}\eta \, \eta = \int \mathrm{d}\eta^* \, \eta^* = 1 \,, \tag{3.28}$$

$$\int \mathrm{d}\eta \mathrm{d}\eta^* \, \eta^* \eta = 1 \,. \tag{3.29}$$

The action for a single nucleon can be rewritten as

$$S^\mathrm{E}_\mathrm{f}(\eta, \eta^*) = \alpha_\mathrm{t} \sum_n \sum_{si} \eta^*_{si,n} \left(\frac{1}{\alpha_\mathrm{t}} \hat{\partial}_0 - \frac{\hat{\nabla}^2}{2\hat{m}_\mathrm{N}} \right) \eta_{si,n} \,, \tag{3.30}$$

and the two-point correlation function is

$$\langle \eta_{s_1 i_1, n} \eta^*_{s_2 i_2, m} \rangle = \frac{\int \mathcal{D}\eta\mathcal{D}\eta^* \eta_{s_1 i_1, n} \eta^*_{s_2 i_2, m} \exp(-S^\mathrm{E}_\mathrm{f})}{\int \mathcal{D}\eta\mathcal{D}\eta^* \exp(-S^\mathrm{E}_\mathrm{f})} \,. \tag{3.31}$$

The subscripts $s_1 s_2$ denote spin indics and $i_1 i_2$ isospin indics. We rewrite the nucleonic action in the form

$$S_{\mathrm{f}}^{\mathrm{E}} = \sum_{nm} \sum_{s_1 i_1 s_2 i_2} \eta^*_{s_1 i_1, n} \, K_{s_1 i_1 n, s_2 i_2 m} \eta_{s_2 i_2, m} \,, \tag{3.32}$$

where K is given by

$$\begin{aligned} K_{s_1 i_1 n, s_2 i_2 m} &= \delta_{s_1 s_2} \delta_{i_1 i_2} \left[\frac{1}{2} (\delta_{n_{\mathrm{t}}+1, m_t} - \delta_{n_{\mathrm{t}}-1, m_t}) \delta_{n_{\mathrm{s}}, m_{\mathrm{s}}} + \frac{\alpha_{\mathrm{t}}}{2 \hat{m}_{\mathrm{N}}} \sum_{\hat{l}} \sum_{\nu} (-)^{\nu} \omega_{\nu} (\delta_{n_{\mathrm{s}}+\nu \hat{l}, m_{\mathrm{s}}} + \delta_{n_{\mathrm{s}}-\nu \hat{l}, m_{\mathrm{s}}}) \right] \\ &= \delta_{s_1 s_2} \delta_{i_1 i_2} \frac{1}{L^3 L_{\mathrm{t}}} \sum_{k_{\mathrm{t}} k_{\mathrm{s}}} K(\hat{k}) \exp\left(i \frac{2\pi}{L_{\mathrm{t}}} k_{\mathrm{t}} (n_{\mathrm{t}} - m_t) \right) \exp\left(i \frac{2\pi}{L} k_{\mathrm{s}} \cdot (n_{\mathrm{s}} - m_{\mathrm{s}}) \right), \end{aligned} \tag{3.33}$$

and

$$K(\hat{k}) = i \sin\left(\frac{2\pi}{L_{\mathrm{t}}} k_{\mathrm{t}} \right) + \frac{\alpha_{\mathrm{t}}}{2 \hat{m}_{\mathrm{N}}} \sum_{\nu} (-)^{\nu} \omega_{\nu} \sum_{\hat{l}} 2 \cos\left(\nu \frac{2\pi}{L} [k_{\mathrm{s}}]_l \right). \tag{3.34}$$

We then have

$$\begin{aligned} \langle \eta_{s_1 i_1, n} \eta^*_{s_2 i_2, m} \rangle &= K^{-1}_{s_1 i_1 n, s_2 i_2 m} \\ &= \delta_{s_1 s_2} \delta_{i_1 i_2} \frac{1}{L^3 L_{\mathrm{t}}} \sum_{k_{\mathrm{t}} k_{\mathrm{s}}} K(\hat{k})^{-1} \exp\left(i \frac{2\pi}{L_{\mathrm{t}}} k_{\mathrm{t}} (n_{\mathrm{t}} - m_t) \right) \exp\left(i \frac{2\pi}{L} k_{\mathrm{s}} \cdot (n_{\mathrm{s}} - m_{\mathrm{s}}) \right). \end{aligned} \tag{3.35}$$

Meanwhile the equal-time Green's function is obtained

$$\langle \eta_{s_1 i_1, n_{\mathrm{s}}}(n_{\mathrm{t}}) \eta^*_{s_2 i_2, m_{\mathrm{s}}}(n_{\mathrm{t}}) \rangle = \delta_{s_1 s_2} \delta_{i_1 i_2} \frac{1}{L^3} \sum_{k_{\mathrm{s}}} K_{\mathrm{s}}(k_{\mathrm{s}})^{-1} \exp\left(i \frac{2\pi}{L} k_{\mathrm{s}} \cdot (n_{\mathrm{s}} - m_{\mathrm{s}}) \right), \tag{3.36}$$

where

$$K_{\mathrm{s}}(k_{\mathrm{s}}) = \frac{\alpha_{\mathrm{t}}}{2 \hat{m}_{\mathrm{N}}} \sum_{\nu} (-)^{\nu} \omega_{\nu} \sum_{\hat{l}} 2 \cos\left(\nu \frac{2\pi}{L} [k_{\mathrm{s}}]_l \right). \tag{3.37}$$

3.2.2 Mesonic Fields on the Lattice

Consider the equation of motion of the pion field

$$(\Box + M^2_{\pi, I}) \pi^I(x) = 0 \,, \tag{3.38}$$

where π^I is a pseudoscalar field with isospin degree of freedom, $\Box$ is the d'Alembert operator, and x stands for the space-time vector with components x_μ. This equation of motion follows from an action principle, $\delta S_\mathrm{b} = 0$, where

$$S_\mathrm{b} = \int \mathrm{d}^4x \left[\frac{1}{2}\partial_\mu \pi^I \partial^\mu \pi^I - \frac{1}{2} M_{\pi,I}^2 \pi^I \pi^I \right] \tag{3.39}$$

Any information about the pion field is contained in the Green functions

$$G_\pi^{II'}(x,y) = \langle \Omega | \mathcal{T}\{\pi^I(x)\pi^{I'}(y)\} | \Omega \rangle \,, \tag{3.40}$$

where $|\Omega\rangle$ is the ground state of the the system and $\mathcal{T}$ denotes the time-ordered product of the operators. The path integral representation of the Green functions is

$$G_\pi^{II'}(x,y) = \frac{\int \mathcal{D}\pi \; \pi^I(x)\pi^{I'}(y) \exp(iS)}{\int \mathcal{D}\pi \exp(iS)} = \langle \pi^I(x)\pi^{I'}(y) \rangle \,. \tag{3.41}$$

We derive the formulation continued to imaginary time,

$$S_\mathrm{b}^\mathrm{E} = \int \mathrm{d}^4x^\mathrm{E} \left(\frac{1}{2}\partial_\mu^\mathrm{E} \pi^{\mathrm{E}I} \partial_\mu^\mathrm{E} \pi^{\mathrm{E}I} + \frac{1}{2} M_{\pi,I}^2 \pi^{\mathrm{E}I} \pi^{\mathrm{E}I} \right) , \tag{3.42}$$

$$G_\pi^{II'}(x^\mathrm{E}, y^\mathrm{E}) = \frac{\int \mathcal{D}\pi^\mathrm{E} \; \pi^{\mathrm{E}I}(x^\mathrm{E}) \pi^{\mathrm{E}I'}(y^\mathrm{E}) \exp(-S^\mathrm{E})}{\int \mathcal{D}\pi^\mathrm{E} \exp(-S^\mathrm{E})} \,, \tag{3.43}$$

where $\pi^\mathrm{E}(x^\mathrm{E}) = \pi(x)$. We now put the pion field on the lattice,

$$\begin{aligned} S_\mathrm{b}^\mathrm{E} &\to \alpha_\mathrm{t} \sum_{\hat{n}} \frac{1}{2} \left[\frac{1}{\alpha_\mathrm{t}^2} \hat{\partial}_0 \hat{\pi}^I(\hat{n}) \hat{\partial}_0 \hat{\pi}^I(\hat{n}) + \hat{\partial}_i \hat{\pi}^I(\hat{n}) \hat{\partial}_i \hat{\pi}^I(\hat{n}) + \hat{M}_{\pi,I}^2 \hat{\pi}^I(\hat{n}) \hat{\pi}^I(\hat{n}) \right] \\ &= \frac{1}{2} \sum_{nm,II'} \pi_n^I D_{nm}^{II'} \pi_m^{I'} \,, \end{aligned} \tag{3.44}$$

where

$$\hat{\pi}(\hat{n}) = a\pi^\mathrm{E}(a\hat{n}) \,, \quad \hat{M}_{\pi,I} = aM_{\pi,I} \,. \tag{3.45}$$

It is convenient to take $\hat{\pi}(\hat{n})$ in its matrix form π_n, and then

$$D^{II'}_{nm} = \delta_{II'}\left[\frac{1}{\alpha_{\mathrm{t}}}(2\delta_{n_{\mathrm{t}},m_t} - \delta_{n_{\mathrm{t}}+1,m_t} - \delta_{n_{\mathrm{t}}-1,m_t})\delta_{n_{\mathrm{s}},m_{\mathrm{s}}} + \alpha_{\mathrm{t}}\delta_{n_{\mathrm{t}},m_t}\sum_{\hat{l}}\sum_{\nu}(-)^{\nu}\omega_{\nu}(\delta_{n_{\mathrm{s}}+\nu\hat{l},m_{\mathrm{s}}} + \delta_{n_{\mathrm{s}}-\nu\hat{l},m_{\mathrm{s}}}) + \alpha_{\mathrm{t}}\hat{M}^2_{\pi,I}\delta_{nm}\right]$$
$$= \delta_{II'}\frac{1}{L^3 L_{\mathrm{t}}}\sum_{k_{\mathrm{t}}k_{\mathrm{s}}} D^I(\hat{k})\exp\left(i\frac{2\pi}{L_{\mathrm{t}}}k_{\mathrm{t}}(n_{\mathrm{t}} - m_t)\right)\exp\left(i\frac{2\pi}{L}k_{\mathrm{s}}(n_{\mathrm{s}} - m_{\mathrm{s}})\right), \tag{3.46}$$

where

$$D^I(\hat{k}) = \frac{2}{\alpha_{\mathrm{t}}}\left(1 - \cos\frac{2\pi}{L_{\mathrm{t}}}k_{\mathrm{t}}\right) + 2\alpha_{\mathrm{t}}\sum_{\hat{l}}\sum_{\nu}(-)^{\nu}\omega_{\nu}\cos\nu\frac{2\pi}{L}[k_{\mathrm{s}}]_l + \alpha_{\mathrm{t}}\hat{M}^2_{\pi,I}\,. \tag{3.47}$$

The discretized two-point function is

$$\langle\pi^I_n\pi^{I'}_m\rangle = [D^{-1}]^{II'}_{nm}$$
$$= \delta_{II'}\frac{1}{L^3 L_{\mathrm{t}}}\sum_{k_{\mathrm{t}}k_{\mathrm{s}}} D^I(\hat{k})^{-1}\exp\left(i\frac{2\pi}{L_{\mathrm{t}}}k_{\mathrm{t}}(n_{\mathrm{t}} - m_t)\right)\exp\left(i\frac{2\pi}{L}k_{\mathrm{s}}(n_{\mathrm{s}} - m_{\mathrm{s}})\right). \tag{3.48}$$

The pion instantaneous correlation function at some certain spatial separation is then

$$\langle\pi^I_{n_{\mathrm{s}}}(n_{\mathrm{t}})\pi^{I'}_{m_{\mathrm{s}}}(n_{\mathrm{t}})\rangle = \delta_{II'}\frac{1}{L^3}\sum_{k_{\mathrm{s}}} D^I_{\mathrm{s}}(\hat{k}_{\mathrm{s}})^{-1}\exp\left(i\frac{2\pi}{L}k_{\mathrm{s}}(n_{\mathrm{s}} - m_{\mathrm{s}})\right), \tag{3.49}$$

where

$$D^I_{\mathrm{s}}(k_{\mathrm{s}}) = \alpha_{\mathrm{t}}\left(2\sum_{\hat{l}}\sum_{\nu}(-)^{\nu}\omega_{\nu}\cos\nu\frac{2\pi}{L}[k_{\mathrm{s}}]_l + \hat{M}^2_{\pi,I}\right). \tag{3.50}$$

3.2.3 Interactions on the Lattice: One-Pion Exchange and Transfer Matrix Operator

Consider the long-range interaction between the nucleonic field and pion.

$$S_{\pi\mathrm{N}} = \int \mathrm{d}^4x\left[-\frac{g_{\mathrm{A}}}{2f_\pi}N^\dagger\tau^I\,\sigma_i\nabla_i\pi^I N\right]. \tag{3.51}$$

At LO, the OPE contributions to the Lagrangian of the χEFT interaction on the lattice takes the form

$$S_{\pi\mathrm{N}}^{\mathrm{E}} = \alpha_{\mathrm{t}} \frac{g_{\mathrm{A}}}{2\hat{f}_\pi} \sum_{I,l} \sum_{\hat{n}} \sum_{s_1 s_2 i_1 i_2} \hat{\partial}_l \, \hat{\pi}^I(\hat{n}) \, \hat{N}^\dagger_{s_1 i_1}(\hat{n}) (\tau^I)_{i_1 i_2} (\sigma_l)_{s_1 s_2} \hat{N}_{s_2 i_2}(\hat{n}) \,, \tag{3.52}$$

where $\hat{f}_\pi = a f_\pi$. Now we write down the partition function with nucleonic field, pion field and their interactions

$$\mathcal{Z} = \int \mathcal{D}\eta \mathcal{D}\eta^* \mathcal{D}\pi \exp\left(-S_{\mathrm{f}}^{\mathrm{E}} - S_{\mathrm{b}}^{\mathrm{E}} - S_{\pi\mathrm{N}}^{\mathrm{E}}\right). \tag{3.53}$$

Here more details are presented for this system. $\mathcal{Z}$ has the following explicit form on a finite, periodic, Euclicean time lattice,

$$\begin{aligned} \mathcal{Z} &= \int \left\{ \prod_{\hat{n}} \prod_{si} \mathrm{d}\eta_{si,\hat{n}} \mathrm{d}\eta^*_{si,\hat{n}} \prod_I \mathrm{d}\pi^I_{\hat{n}} \right\} \exp\left(-S_{\mathrm{f}}^{\mathrm{E}} - S_{\mathrm{b}}^{\mathrm{E}} - S_{\pi\mathrm{N}}^{\mathrm{E}}\right) \\ &\to \int \prod_{n_{\mathrm{t}}} \left\{ \prod_{n_{\mathrm{s}}} \prod_{si} \mathrm{d}\eta_{si,\hat{n}} \mathrm{d}\eta^*_{si,\hat{n}} \prod_I \mathrm{d}\pi^I_{\hat{n}} \right\} \prod_{n_{\mathrm{t}}} \left\{ \exp\left(-H_{\mathrm{f}}^{(n_{\mathrm{t}})} - H_{\mathrm{b}}^{(n_{\mathrm{t}})}\right) \exp\left(-H_{\mathrm{f}} - H_{\mathrm{b}} - H_{\pi\mathrm{N}}\right) \right\} . \end{aligned} \tag{3.54}$$

The actions of the nucleons and pions are seperated into time-dependent parts and stationary parts

$$S_{\mathrm{f}}^{\mathrm{E}} = \sum_{n_{\mathrm{t}}} H_{\mathrm{f}}^{(n_{\mathrm{t}})} + \sum_{n_{\mathrm{t}}} H_{\mathrm{f}} \,, \tag{3.55}$$

$$S_{\mathrm{b}}^{\mathrm{E}} = \sum_{n_{\mathrm{t}}} H_{\mathrm{b}}^{(n_{\mathrm{t}})} + \sum_{n_{\mathrm{t}}} H_{\mathrm{b}} \,, \tag{3.56}$$

$$S_{\pi\mathrm{N}}^{\mathrm{E}} = \sum_{n_{\mathrm{t}}} H_{\pi\mathrm{N}} \,, \tag{3.57}$$

where

$$H_{\mathrm{f}} = \alpha_{\mathrm{t}} \sum_{n_{\mathrm{s}}} \hat{\eta}^*(\hat{n}) \left(\frac{1}{\alpha_{\mathrm{t}}} \hat{\partial}_0 - \frac{\hat{\nabla}^2}{2\hat{m}_{\mathrm{N}}} \right) \hat{\eta}(\hat{n}) \,, \tag{3.58}$$

$$H_{\mathrm{b}} = \alpha_{\mathrm{t}} \sum_{n_{\mathrm{s}}} \sum_I \frac{1}{2} \left[\frac{1}{\alpha_{\mathrm{t}}^2} \hat{\partial}_0 \hat{\pi}^I(\hat{n}) \hat{\partial}_0 \hat{\pi}^I(\hat{n}) + \sum_l \hat{\partial}_l \hat{\pi}^I(\hat{n}) \hat{\partial}_l \hat{\pi}^I(\hat{n}) + \hat{m}_\pi^2 \hat{\pi}^I(\hat{n}) \hat{\pi}^I(\hat{n}) \right] , \tag{3.59}$$

$$H_{\pi\mathrm{N}} = \alpha_{\mathrm{t}} \sum_{n_{\mathrm{s}}} \frac{g_{\mathrm{A}}}{2\hat{f}_\pi} \sum_{I,l} \sum_{s_1 s_2 i_1 i_2} \hat{\partial}_l \, \hat{\pi}^I(\hat{n}) \hat{\eta}^*_{s_1 i_1}(\hat{n}) [\tau^I]_{i_1 i_2} [\sigma_l]_{s_1 s_2} \hat{\eta}_{s_2 i_2}(\hat{n}) \,. \tag{3.60}$$

The partition function has a condensed form as

$$\mathcal{Z} \to \mathrm{Tr}\left(\prod_{n_\mathrm{t}} M^{(n_\mathrm{t})}\right) , \tag{3.61}$$

where

$$\begin{aligned} M^{(n_\mathrm{t})} &= \int \prod_{n_\mathrm{s}} \left\{ \prod_{si} \mathrm{d}\eta_{si,n_\mathrm{s}}(n_\mathrm{t}) \mathrm{d}\eta^*_{si,n_\mathrm{s}}(n_\mathrm{t}) \prod_I \mathrm{d}\pi^I_{n_\mathrm{s}}(n_\mathrm{t}) \right\} \exp\left(-H_\mathrm{f} - H_\mathrm{b} - H_{\pi\mathrm{N}}\right) \\ &= \int \left\{ \prod_{n_\mathrm{s}} \prod_I \mathrm{d}\pi^I_{n_\mathrm{s}}(n_\mathrm{t}) \right\} e^{-H_\mathrm{b}} \int \left\{ \prod_{n_\mathrm{s}} \prod_{si} \mathrm{d}\eta_{si,n_\mathrm{s}}(n_\mathrm{t}) \mathrm{d}\eta^*_{si,n_\mathrm{s}}(n_\mathrm{t}) \right\} \exp\left(-H_\mathrm{f} - H_{\pi\mathrm{N}}\right) \\ &= \int \mathcal{D}\pi(n_\mathrm{t})\, e^{-H_\mathrm{b}} \int \mathcal{D}\eta(n_\mathrm{t}) \mathcal{D}\eta^*(n_\mathrm{t}) \exp\left(-H_\mathrm{f} - H_{\pi\mathrm{N}}\right) \\ &= \int \mathcal{D}\pi(n_\mathrm{t})\, e^{-H_\mathrm{b}} \ [: \exp\left(-H_\mathrm{f} - H_{\pi\mathrm{N}}\right) :] \ . \end{aligned} \tag{3.62}$$

The double colon :: denotes normal-ordered operators. The transfer matrix indicates the evolution of a quantum system in an infinitesmal timestep ϵ, which means we may obtain the evolution operator between any two time points by accumulating the transfer matrix over the time interval. In this section we investigate further the transfer matrix of a nucleonic system from which spectral information can be extracted as well as any observations of interest in the scattering process, such as scattering lengths, effective ranges cross sections and phase shifts.

In non-relativistic χEFT with instantaneous interactions, the Hamiltonian, Eq. (3.58), becomes static

$$H_\mathrm{f} = \alpha_\mathrm{t} \sum_{n_\mathrm{s}} \hat{\eta}^*(\hat{n}) \left(-\frac{\hat{\nabla}^2}{2\hat{m}_\mathrm{N}} \right) \hat{\eta}(\hat{n}) \ , \tag{3.63}$$

$$H_\mathrm{b} = \alpha_\mathrm{t} \sum_{n_\mathrm{s}} \sum_I \frac{1}{2} \left[\sum_l \hat{\partial}_l \hat{\pi}^I(\hat{n}) \hat{\partial}_l \hat{\pi}^I(\hat{n}) + \hat{m}_\pi^2 \hat{\pi}^I(\hat{n}) \hat{\pi}^I(\hat{n}) \right] , \tag{3.64}$$

$$H_{\pi\mathrm{N}} = \alpha_\mathrm{t} \sum_{n_\mathrm{s}} \frac{g_\mathrm{A}}{2\hat{f}_\pi} \sum_{I,l} \sum_{s_1 s_2 i_1 i_2} \hat{\partial}_l \, \hat{\pi}^I(\hat{n}) \hat{\eta}^*_{s_1 i_1}(\hat{n}) [\tau^I]_{i_1 i_2} [\sigma_l]_{s_1 s_2} \hat{\eta}_{s_2 i_2}(\hat{n}) \ . \tag{3.65}$$

If only the NN system is of interest in the discussion, the transfer matrix can be written as

$$M^{(n_\mathrm{t})} \to : \exp\left\{ -\alpha_\mathrm{t} \sum_{n_\mathrm{s}} \sum_{\beta=\{1,2\}} \eta^{(\beta)*}_{n_\mathrm{s}}(n_\mathrm{t}) \left(-\frac{\hat{\nabla}^2}{2\hat{m}_\mathrm{N}} \right) \eta^{(\beta)}_{n_\mathrm{s}}(n_\mathrm{t}) \right. \tag{3.66}$$
$$\left. + \alpha_\mathrm{t}^2 \frac{g_\mathrm{A}^2}{4\hat{f}_\pi^2} \sum_{n_\mathrm{s} m_\mathrm{s}} \sum_{II'} \sum_{s_1 s_2} \langle \Delta_{s_1} \hat{\pi}^I_{n_\mathrm{s}}(n_\mathrm{t}) \Delta_{s_2} \hat{\pi}^{I'}_{m_\mathrm{s}}(n_\mathrm{t}) \rangle \, \eta^{(1)*}_{n_\mathrm{s}}(n_\mathrm{t}) \sigma^{(1)}_{s_1} \tau^{(1)I} \eta^{(1)}_{n_\mathrm{s}}(n_\mathrm{t}) \, \eta^{(2)*}_{m_\mathrm{s}}(n_\mathrm{t}) \sigma^{(2)}_{s_2} \tau^{(2)I'} \eta^{(2)}_{m_\mathrm{s}}(n_\mathrm{t}) \right\} : ,$$

where

$$\langle \Delta_{s_1} \hat{\pi}^I_{n_\mathrm{s}}(n_\mathrm{t}) \Delta_{s_2} \hat{\pi}^{I'}_{m_\mathrm{s}}(n_\mathrm{t}) \rangle = \frac{\int \mathcal{D}\pi(n_\mathrm{t}) \, \Delta_{s_1} \hat{\pi}^I_{n_\mathrm{s}}(n_\mathrm{t}) \Delta_{s_2} \hat{\pi}^{I'}_{m_\mathrm{s}}(n_\mathrm{t}) \exp(-H_\mathrm{b})}{\int \mathcal{D}\pi(n_\mathrm{t}) \exp(-H_\mathrm{b})}$$
$$= \delta_{II'} \frac{1}{L^3} \sum_{k_\mathrm{s}} \frac{[\hat{q}_\mathrm{s}]_{s_1} [\hat{q}_\mathrm{s}]_{s_2}}{\alpha_\mathrm{t}(\hat{q}_\mathrm{s}^2 + \hat{M}^2_{\pi,I})} \exp\left(i \frac{2\pi}{L} k_\mathrm{s} \cdot (n_\mathrm{s} - m_\mathrm{s}) \right) , \tag{3.67}$$

and in which

$$\hat{q}_\mathrm{s}^2 = \sum_l \sum_\nu (-)^\nu \omega_\nu 2 \cos \nu \frac{2\pi}{L} [k_\mathrm{s}]_l \, , \tag{3.68}$$

$$[\hat{q}_\mathrm{s}]_l = \sum_\nu (-)^{\nu+1} o_\nu \sin \nu \frac{2\pi}{L} [k_\mathrm{s}]_l \, . \tag{3.69}$$

We introduce the CM scheme (CMS) for two identical nucleons

$$R_\mathrm{s} = (n_\mathrm{s} + m_\mathrm{s})/2 \, , \quad r_\mathrm{s} = n_\mathrm{s} - m_\mathrm{s} \, . \tag{3.70}$$

R_s, r_s indicates motions of CM and the relative position of the nucleons, respectively. The transfer matrix is rewritten as

$$M^{(n_\mathrm{t})} \to : \exp\left\{ -\alpha_\mathrm{t} \sum_{r_\mathrm{s}} \eta^{(2)*}_{-r_\mathrm{s}/2}(n_\mathrm{t}) \eta^{(1)*}_{r_\mathrm{s}/2}(n_\mathrm{t}) \left(-\frac{\hat{\nabla}^2_r}{2(\hat{m}_\mathrm{N}/2)} \right) \eta^{(1)}_{r_\mathrm{s}/2}(n_\mathrm{t}) \eta^{(2)}_{-r_\mathrm{s}/2}(n_\mathrm{t}) \right.$$
$$\left. - \alpha_\mathrm{t} \sum_{r_\mathrm{s}} \sum_{II'} \sum_{s_1 s_2} [V_{1\pi}(r_\mathrm{s}, n_\mathrm{t})]^{II'}_{s_1 s_2} \, \eta^{(1)*}_{r_\mathrm{s}/2}(n_\mathrm{t}) \sigma^{(1)}_{s_1} \tau^{(1)I} \eta^{(1)}_{r_\mathrm{s}/2}(n_\mathrm{t}) \, \eta^{(2)*}_{-r_\mathrm{s}/2}(n_\mathrm{t}) \sigma^{(2)}_{s_2} \tau^{(2)I'} \eta^{(2)}_{-r_\mathrm{s}/2}(n_\mathrm{t}) \right\} : \, . \tag{3.71}$$

with

$$[V_{1\pi}(r_\mathrm{s}, n_\mathrm{t})]^{II'}_{s_1 s_2} = \delta_{II'} \frac{1}{L^3} \sum_{k_\mathrm{s}} \left(-\frac{g_\mathrm{A}^2}{4\hat{f}_\pi^2} \right) \frac{[\hat{q}_\mathrm{s}]_{s_1} [\hat{q}_\mathrm{s}]_{s_2}}{\alpha_\mathrm{t}(\hat{q}_\mathrm{s}^2 + \hat{M}^2_{\pi,I})} \exp\left(i \frac{2\pi}{L} k_\mathrm{s} \cdot r_\mathrm{s} \right) , \tag{3.72}$$

where we have integrated out the translational motion of the two-body system as a whole.

3.2.4 Interactions on the Lattice: First Order Contact Interactions and Auxillary Fields

Consider the contact interactions that appear at LO in χEFT.

$$S_{\mathrm{NN}} = \int \mathrm{d}^4x \left[-\frac{1}{2} C_0 (N^\dagger N)(N^\dagger N) - \frac{1}{2} C_{\mathrm{I}} (N^\dagger \tau^I N)(N^\dagger \tau^I N) \right] . \tag{3.73}$$

Following the routine shown previously, we can write down the action for contact term / contact operator / contact interaction (CT)s in Euclicean space,

$$S^{\mathrm{E}}_{\mathrm{NN}} = \alpha_{\mathrm{t}} \sum_{\hat{n}} \left[\frac{1}{2} \hat{C}_0 \hat{N}^\dagger(\hat{n}) \hat{N}(\hat{n}) \hat{N}^\dagger(\hat{n}) \hat{N}(\hat{n}) + \frac{1}{2} \hat{C}_{\mathrm{I}} \sum_I \hat{N}^\dagger(\hat{n}) \tau^I \hat{N}(\hat{n}) \hat{N}^\dagger(\hat{n}) \tau^I \hat{N}(\hat{n}) \right] , \tag{3.74}$$

where

$$\hat{C}_0 = a^{-2} C_0 , \tag{3.75}$$

$$\hat{C}_{\mathrm{I}} = a^{-2} C_{\mathrm{I}} . \tag{3.76}$$

We may easily include this zero-range contact interaction into the transfer matrix, Eq. (3.62)

$$M^{(n_{\mathrm{t}})} \to \int \mathcal{D}\pi(n_{\mathrm{t}})\, e^{-H_{\mathrm{b}}} \left[: \exp\left(-H_{\mathrm{f}} - H_{\pi\mathrm{N}} - H_{\mathrm{NN}} \right) : \right] . \tag{3.77}$$

with the static Hamiltonians

$$\begin{aligned}
H_{\mathrm{f}} &= \alpha_{\mathrm{t}} \sum_{n_{\mathrm{s}}} \eta^*_n \left(-\frac{\hat{\nabla}^2}{2\hat{m}_{\mathrm{N}}} \right) \eta_n , \\
H_{\mathrm{b}} &= \alpha_{\mathrm{t}} \sum_{n_{\mathrm{s}}} \sum_{I,l} \left[\frac{1}{2} \hat{\partial}_l \pi^I_n \hat{\partial}_l \pi^I_n + \frac{1}{2} \hat{m}^2_\pi \pi^I_n \pi^I_n \right] , \\
H_{\pi\mathrm{N}} &= \alpha_{\mathrm{t}} \sum_{n_{\mathrm{s}}} \frac{g_{\mathrm{A}}}{2\hat{f}_\pi} \sum_{I,l} \sum_{s_1 s_2 i_1 i_2} \hat{\partial}_l \, \pi^I_n \, \eta^*_{s_1 i_1, n} (\tau^I)_{i_1 i_2} (\sigma_l)_{s_1 s_2} \eta_{s_2 i_2, n} , \\
H_{\mathrm{NN}} &= \alpha_{\mathrm{t}} \sum_{n_{\mathrm{s}}} \frac{1}{2!} \sum_{\alpha \neq \beta} \left[\hat{C}_0 \, \eta^{(\alpha)*}_n \eta^{(\alpha)}_n \, \eta^{(\beta)*}_n \eta^{(\beta)}_n + \hat{C}_{\mathrm{I}} \sum_I \, \eta^{(\alpha)*}_n \tau^{(\alpha)a} \eta^{(\alpha)}_n \, \eta^{(\beta)*}_n \tau^{(\beta)a} \eta^{(\beta)}_n \right] .
\end{aligned} \tag{3.78}$$

Auxillary Fields

A formal integral relation in Gaussian form,

$$\int \frac{\mathrm{d}s}{\sqrt{2\pi}} \exp\left[-\frac{1}{2}s^2 + bs\right] = e^{\frac{1}{2}b^2} \,, \tag{3.79}$$

allows us to rewrite the operator $: \exp\left(-H_{\mathrm{NN}}\right) :$ into path integral form. As compared to the inversion of Eq. (3.79), we have

$$: \exp\left(-H_{\mathrm{NN}}\right) : \rightarrow \int \mathcal{D}s\mathcal{D}s_{\mathrm{I}} \exp\left[-H_{\mathrm{ss}} - H_{\mathrm{s_I s_I}} - H_{\mathrm{sN}} - H_{\mathrm{s_I N}}\right], \tag{3.80}$$

where

$$H_{\mathrm{ss}} = \frac{1}{2}\sum_{n_{\mathrm{s}}} s_n^2 \,, \tag{3.81}$$

$$H_{\mathrm{sN}} = \sqrt{-\alpha_{\mathrm{t}}\hat{C}_0}\sum_{n_{\mathrm{s}}} s_n\, \eta_n^* \eta_n \,, \tag{3.82}$$

$$H_{\mathrm{s_I s_I}} = \frac{1}{2}\sum_{n_{\mathrm{s}}} [s_{\mathrm{I}}]_n^2 \,, \tag{3.83}$$

$$H_{\mathrm{s_I N}} = \sqrt{-\alpha_{\mathrm{t}}\hat{C}_{\mathrm{I}}}\sum_{n_{\mathrm{s}}} [s_{\mathrm{I}}]_n\, \eta_n^* \tau \eta_n \,, \tag{3.84}$$

and $\mathcal{D}s\mathcal{D}s_{\mathrm{I}}$ is written as shorthand for the integral measure

$$\int \mathcal{D}s\mathcal{D}s_{\mathrm{I}} = \int \prod_n \frac{\mathrm{d}s_n}{\sqrt{2\pi}} \frac{\mathrm{d}[s_{\mathrm{I}}]_n}{\sqrt{2\pi}} \,. \tag{3.85}$$

The formula for the full transfer matrix at LO of χEFT is

$$M^{(n_{\mathrm{t}})} \rightarrow \int \mathcal{D}\pi(n_{\mathrm{t}})\mathcal{D}s(n_{\mathrm{t}})\mathcal{D}s_{\mathrm{I}}(n_{\mathrm{t}})\, e^{-H_{\mathrm{b}} - H_{\mathrm{ss}} - H_{\mathrm{s_I s_I}}} \left[: \exp\left(-H_{\mathrm{f}} - H_{\pi\mathrm{N}} - H_{\mathrm{sN}} - H_{\mathrm{s_I N}}\right) :\right] \,. \tag{3.86}$$

Ref. [10] demonstrates the physical meaning of the transfer matrix in Figs. 3.1 and 3.2, it also shows how the auxiliary field formalism makes the problem amenable to pralell computing.

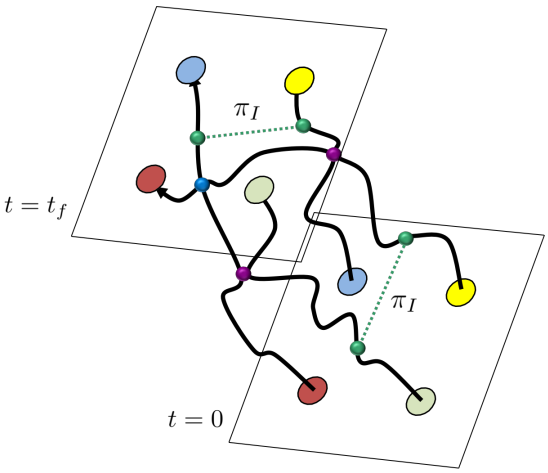

Figure 3.1: Worldline description of the interaction of four nucleons with explicit pion exchanges and contact interactions.

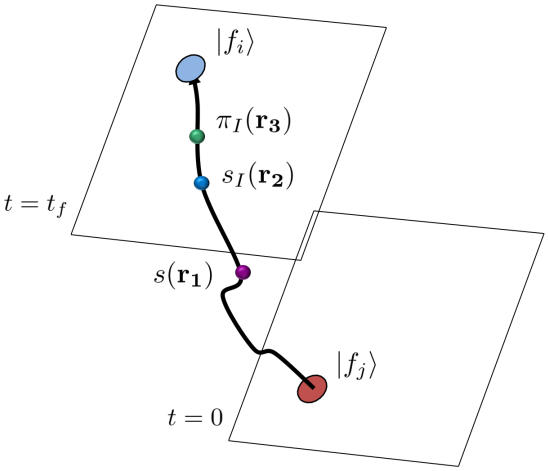

Figure 3.2: Worldline description in erms of auxiliary fields. As can be seen, such a description is particularly suited for paralell computing.

Transfer Matrix of 2-Body System at Leading Order

Note that the CT for the single nucleonic system vanishes due to the anticommutation relation for the nucleonic fields. When it comes to a NN system, we have

$$S_{\mathrm{NN}}^{\mathrm{E}}(\eta,\eta^*) = \alpha_{\mathrm{t}} \sum_n \left[\hat{C}_0\, \eta_n^{(1)*}\eta_n^{(1)}\, \eta_n^{(2)*}\eta_n^{(2)} + \hat{C}_{\mathrm{I}} \sum_I \eta_n^{(1)*}\tau^{(1)I}\eta_n^{(1)}\, \eta_n^{(2)*}\tau^{(2)I}\eta_n^{(2)} \right], \tag{3.87}$$

so that

$$
\begin{aligned}
:\exp\left(-H_{\mathrm{NN}}\right):\rightarrow :\exp\Bigg\{ & -\alpha_{\mathrm{t}}\sum_{n_{\mathrm{s}}}\ \hat{C}_0\eta^{(1)*}_{n_{\mathrm{s}}}(n_{\mathrm{t}})\eta^{(1)}_{n_{\mathrm{s}}}(n_{\mathrm{t}})\ \eta^{(2)*}_{n_{\mathrm{s}}}(n_{\mathrm{t}})\eta^{(2)}_{n_{\mathrm{s}}}(n_{\mathrm{t}}) \\
& -\alpha_{\mathrm{t}}\sum_{n_{\mathrm{s}}}\sum_{I}\hat{C}_{\mathrm{I}}\eta^{(1)*}_{n_{\mathrm{s}}}(n_{\mathrm{t}})\tau^{(1)I}\eta^{(1)}_{n_{\mathrm{s}}}(n_{\mathrm{t}})\ \eta^{(2)*}_{n_{\mathrm{s}}}(n_{\mathrm{t}})\tau^{(2)I}\eta^{(2)}_{n_{\mathrm{s}}}(n_{\mathrm{t}})\Bigg\}: \\
\rightarrow :\exp\Bigg\{ & -\alpha_{\mathrm{t}}\sum_{n_{\mathrm{s}}m_{\mathrm{s}}}\ \hat{C}_0\eta^{(1)*}_{n_{\mathrm{s}}}(n_{\mathrm{t}})\eta^{(1)}_{n_{\mathrm{s}}}(n_{\mathrm{t}})\ \eta^{(2)*}_{m_{\mathrm{s}}}(n_{\mathrm{t}})\eta^{(2)}_{m_{\mathrm{s}}}(n_{\mathrm{t}}) \\
& -\alpha_{\mathrm{t}}\sum_{n_{\mathrm{s}}m_{\mathrm{s}}}\sum_{I}\hat{C}_{\mathrm{I}}\eta^{(1)*}_{n_{\mathrm{s}}}(n_{\mathrm{t}})\tau^{(1)I}\eta^{(1)}_{n_{\mathrm{s}}}(n_{\mathrm{t}})\ \eta^{(2)*}_{m_{\mathrm{s}}}(n_{\mathrm{t}})\tau^{(2)I}\eta^{(2)}_{m_{\mathrm{s}}}(n_{\mathrm{t}})\Bigg\}: \\
\rightarrow :\exp\Bigg\{ & -\alpha_{\mathrm{t}}\sum_{r_{\mathrm{s}}}\ \eta^{(2)*}_{-r_{\mathrm{s}}/2}(n_{\mathrm{t}})\eta^{(1)*}_{r_{\mathrm{s}}/}(n_{\mathrm{t}})\left[V_{\mathrm{ct},0}(r_{\mathrm{s}},n_{\mathrm{t}})\right]\ \eta^{(1)}_{r_{\mathrm{s}}/2}(n_{\mathrm{t}})\eta^{(2)}_{-r_{\mathrm{s}}/2}(n_{\mathrm{t}})\Bigg\}:,
\end{aligned}
\tag{3.88}
$$

where

$$
\begin{aligned}
V_{\mathrm{ct},0}(r_{\mathrm{s}},n_{\mathrm{t}}) &= \hat{C}_0\delta_{r_{\mathrm{s}},0}+\hat{C}_{\mathrm{I}}\delta_{r_{\mathrm{s}},0}\sum_{I}\tau^{(1)I}\tau^{(2)I} \\
&= \frac{1}{L^3}\sum_{k_{\mathrm{s}}}\left[\hat{C}_0+\hat{C}_{\mathrm{I}}\sum_{I}\tau^{(1)I}\tau^{(2)I}\right]\exp\left(i\frac{2\pi}{L}k_{\mathrm{s}}\cdot r_{\mathrm{s}}\right)
\end{aligned}
\tag{3.89}
$$

with ‘ct’ indicating CTs of nucleon-nucleon (NN). Now we can write down the complete transfer matrix for the NN system at LO,

$$
\begin{aligned}
M^{(n_{\mathrm{t}})}\rightarrow :\exp\Bigg\{ & -\alpha_{\mathrm{t}}\sum_{r_{\mathrm{s}}}\eta^{(2)*}_{-r_{\mathrm{s}}/2}(n_{\mathrm{t}})\eta^{(1)*}_{r_{\mathrm{s}}/2}(n_{\mathrm{t}})\left(-\frac{\hat{\nabla}^2_r}{2(\hat{m}_{\mathrm{N}}/2)}\right)\eta^{(1)}_{r_{\mathrm{s}}/2}(n_{\mathrm{t}})\eta^{(2)}_{-r_{\mathrm{s}}/2}(n_{\mathrm{t}}) \\
& -\alpha_{\mathrm{t}}\sum_{r_{\mathrm{s}}}\ \eta^{(2)*}_{-r_{\mathrm{s}}/2}(n_{\mathrm{t}})\eta^{(1)*}_{r_{\mathrm{s}}/2}(n_{\mathrm{t}})\left[V_{1\pi}(r_{\mathrm{s}},n_{\mathrm{t}})\right]\ \eta^{(1)}_{r_{\mathrm{s}}/2}(n_{\mathrm{t}})\eta^{(2)}_{-r_{\mathrm{s}}/2}(n_{\mathrm{t}}) \\
& -\alpha_{\mathrm{t}}\sum_{r_{\mathrm{s}}}\ \eta^{(2)*}_{-r_{\mathrm{s}}/2}(n_{\mathrm{t}})\eta^{(1)*}_{r_{\mathrm{s}}/2}(n_{\mathrm{t}})\left[V_{\mathrm{ct},0}(r_{\mathrm{s}},n_{\mathrm{t}})\right]\ \eta^{(1)}_{r_{\mathrm{s}}/2}(n_{\mathrm{t}})\eta^{(2)}_{-r_{\mathrm{s}}/2}(n_{\mathrm{t}})\Bigg\}:
\end{aligned}
\tag{3.90}
$$

with

$$
V_{1\pi}(r_{\mathrm{s}},n_{\mathrm{t}})=\frac{1}{L^3}\sum_{k_{\mathrm{s}}}\exp\left(i\frac{2\pi}{L}k_{\mathrm{s}}\cdot r_{\mathrm{s}}\right)\left(-\frac{g_{\mathrm{A}}^2}{4\hat{f}_\pi^2}\right)\sum_{I}\frac{\tau^{(1)I}\tau^{(2)I}}{\hat{q}_{\mathrm{s}}^2+\hat{M}^2_{\pi,I}}\ \hat{q}_{\mathrm{s}}\cdot\sigma^{(1)}\ \hat{q}_{\mathrm{s}}\cdot\sigma^{(2)}\,.
\tag{3.91}
$$

3.3 Interactions on the Lattice: Improvement of Contact Interactions

In the previous sections we discussed the LO interactions, both pionic or contact, as well as long-ranged or short-ranged interactions due to pion exchange. Here we discuss, in general, a little about the structure of the interaction between two nucleons. When we focus on the position-spin structure of the potential, the vectors for individual nucleons can be only given by the position, momentum and spin: $\mathbf{r}_1, \mathbf{r}_2, \mathbf{p}_1, \mathbf{p}_2, \boldsymbol{\sigma}_1, \boldsymbol{\sigma}_2$. Due to the constraint of Galilean symmetry, the interactions are parameterized by the relative distance between the two particles, $\mathbf{r} = \mathbf{r}_1 - \mathbf{r}_2$, or the relative momentum, $\mathbf{p} = (\mathbf{p}_1 - \mathbf{p}_2)/2$, and must be independent of the CM motion. We therefore construct operators satisfying the following properties: rotational invariance, invariance under a parity operation, time reversal invariance, hermiticity, invariance in respect to interchanging the nucleon labels. Finally the form can be only taken as

$$\left\{\mathbf{1}_{\text{spin}}, \boldsymbol{\sigma}_1 \cdot \boldsymbol{\sigma}_2, S_{12}(\mathbf{r}), S_{12}(\mathbf{p}), \mathbf{L}\cdot\mathbf{S}, (\mathbf{L}\cdot\mathbf{S})^2\right\} \times \left\{\mathbf{1}_{\text{isospin}}, \boldsymbol{\tau}_1 \cdot \boldsymbol{\tau}_2\right\} , \tag{3.92}$$

where $\mathbf{L} = \mathbf{r} \times \mathbf{p}$, $\mathbf{S} = (\boldsymbol{\sigma}_1 + \boldsymbol{\sigma}_2)/2$ and $S_{12}(\mathbf{x}) = 3\boldsymbol{\sigma}_1 \cdot \hat{\mathbf{x}}\, \boldsymbol{\sigma}_2 \cdot \hat{\mathbf{x}} - \boldsymbol{\sigma}_1 \cdot \boldsymbol{\sigma}_2$ with $\hat{\mathbf{x}} = \mathbf{x}/|\mathbf{x}|$. The operators are built up with this position-spin-isospin structure multiplied by scalar functions of r^2, p^2 and L^2, which give contributions of higher order momentum.

In momentum space, the matrix of the interactions can be written in the basis of initial and final CM momenta of the two nucleons $\mathbf{p}$ and $\mathbf{p}'$. The same logic stated above lead to the most general form of the momentum-spin-isospin structure as

$$\left\{\mathbf{1}_{\text{spin}}, \boldsymbol{\sigma}_1 \cdot \boldsymbol{\sigma}_2, S_{12}(\mathbf{q}), S_{12}(\mathbf{k}), i\mathbf{S}\cdot\mathbf{q}\times\mathbf{k}, \boldsymbol{\sigma}_1 \cdot \mathbf{q}\times\mathbf{k}\, \boldsymbol{\sigma}_2 \cdot \mathbf{q}\times\mathbf{k}\right\} \times \left\{\mathbf{1}_{\text{isospin}}, \boldsymbol{\tau}_1 \cdot \boldsymbol{\tau}_2\right\} , \tag{3.93}$$

where $\mathbf{q} = \mathbf{p}' - \mathbf{p}$ is the transfer momentum and $\mathbf{k} = (\mathbf{p}' + \mathbf{p})/2$ is the average momentum. The operators are multiplied with the scalar functions that depend on $p^2, p'^2, \mathbf{p}\cdot\mathbf{p}'$.

In the scheme of χEFT, CTs have contributions at order Q^0, Q^2, Q^4, ... which correspond respectively to terms of LO, NLO, N^{3}LO ... with Q denoting the typical relative momentum of the two nucleons, $Q \sim p, p' \sim q, k$.

At LO, there are four operators with dimension Q^0

$$V_{\text{ct},0} = \alpha_1 + \alpha_2 \boldsymbol{\sigma}_1 \cdot \boldsymbol{\sigma}_2 + \alpha_3 \boldsymbol{\tau}_1 \cdot \boldsymbol{\tau}_2 + \alpha_4 \boldsymbol{\tau}_1 \cdot \boldsymbol{\tau}_2\, \boldsymbol{\sigma}_1 \cdot \boldsymbol{\sigma}_2 \, . \tag{3.94}$$

but only two of them are independent due to symmetry constraints, see Appendix E of Ref. [11]. We

therefore choose two of them to construct the LO potential

$$V_{\mathrm{ct},0} = C_0 + C_I \boldsymbol{\tau}_1 \cdot \boldsymbol{\tau}_2 \,. \tag{3.95}$$

At NLO, generally we have 14 operators of Q^2

$$\begin{aligned} V_{\mathrm{ct},2} = {} & \beta_1\, q^2 + \beta_2 q^2 \boldsymbol{\tau}_1 \cdot \boldsymbol{\tau}_2 + \beta_3 q^2 \boldsymbol{\sigma}_1 \cdot \boldsymbol{\sigma}_2 + \beta_4 q^2 \boldsymbol{\sigma}_1 \cdot \ \boldsymbol{\sigma}_2 \boldsymbol{\tau}_1 \cdot \boldsymbol{\tau}_2 \\ & + \beta_5\, k^2 + \beta_6 k^2 \boldsymbol{\tau}_1 \cdot \boldsymbol{\tau}_2 + \beta_7 k^2 \boldsymbol{\sigma}_1 \cdot \boldsymbol{\sigma}_2 + \beta_8 k^2 \boldsymbol{\sigma}_1 \cdot \ \boldsymbol{\sigma}_2 \boldsymbol{\tau}_1 \cdot \boldsymbol{\tau}_2 \\ & + \beta_9\, i\, \mathbf{S} \cdot \mathbf{q} \times \mathbf{k} + \beta_{10}\, i\, \mathbf{S} \cdot \mathbf{q} \times \mathbf{k}\, \boldsymbol{\tau}_1 \cdot \boldsymbol{\tau}_2 \\ & + \beta_{11} \boldsymbol{\sigma}_1 \cdot \mathbf{q} \boldsymbol{\sigma}_2 \cdot \mathbf{q} + \beta_{12} \boldsymbol{\sigma}_1 \cdot \mathbf{q} \boldsymbol{\sigma}_2 \cdot \mathbf{q} \boldsymbol{\tau}_1 \cdot \boldsymbol{\tau}_2 + \beta_{13} \boldsymbol{\sigma}_1 \cdot \mathbf{k} \boldsymbol{\sigma}_2 \cdot \mathbf{k} + \beta_{14} \boldsymbol{\sigma}_1 \cdot \mathbf{k} \boldsymbol{\sigma}_2 \cdot \mathbf{k} \boldsymbol{\tau}_1 \cdot \boldsymbol{\tau}_2 \,. \end{aligned} \tag{3.96}$$

from which, after symmetry considerations are taken into account, there remain 7 linearly independent operators

$$\begin{aligned} V_{\mathrm{ct},2} = {} & C_1\, q^2 + C_2 q^2 \boldsymbol{\tau}_1 \cdot \boldsymbol{\tau}_2 + C_3 q^2 \boldsymbol{\sigma}_1 \cdot \boldsymbol{\sigma}_2 + C_4 q^2 \boldsymbol{\sigma}_1 \cdot \ \boldsymbol{\sigma}_2 \boldsymbol{\tau}_1 \cdot \boldsymbol{\tau}_2 \\ & + C_5 \boldsymbol{\sigma}_1 \cdot \mathbf{q} \boldsymbol{\sigma}_2 \cdot \mathbf{q} + C_6 \boldsymbol{\sigma}_1 \cdot \mathbf{q} \boldsymbol{\sigma}_2 \cdot \mathbf{q} \boldsymbol{\tau}_1 \cdot \boldsymbol{\tau}_2 + C_7 i\, \mathbf{S} \cdot \mathbf{q} \times \mathbf{k} \,. \end{aligned} \tag{3.97}$$

At N^{3}LO, totally 30 operators with dimension Q^4 are available of which we have 15 free coefficients.

$$\begin{aligned} V_{\mathrm{ct},4} = {} & D_1\, q^4 + D_2\, q^4\, \boldsymbol{\tau}_1 \cdot \boldsymbol{\tau}_2 + D_3\, q^4 \boldsymbol{\sigma}_1 \cdot \boldsymbol{\sigma}_2 + D_4\, q^4 \boldsymbol{\tau}_1 \cdot \boldsymbol{\tau}_2\, \boldsymbol{\sigma}_1 \cdot \boldsymbol{\sigma}_2 \\ & + D_5 (\mathbf{q} \cdot \mathbf{k})^2 + D_6 (\mathbf{q} \cdot \mathbf{k})^2\, \boldsymbol{\tau}_1 \cdot \boldsymbol{\tau}_2 + D_7 (\mathbf{q} \cdot \mathbf{k})^2\, \boldsymbol{\sigma}_1 \cdot \boldsymbol{\sigma}_2 + D_8 (\mathbf{q} \cdot \mathbf{k})^2 \boldsymbol{\tau}_1 \cdot \boldsymbol{\tau}_2\, \boldsymbol{\sigma}_1 \cdot \boldsymbol{\sigma}_2 \\ & + D_9 q^2 i\, \mathbf{S} \cdot \mathbf{q} \times \mathbf{k} + D_{10} q^2 i\, \mathbf{S} \cdot \mathbf{q} \times \mathbf{k}\, \boldsymbol{\tau}_1 \cdot \boldsymbol{\tau}_2 + D_{11} q^2\, \boldsymbol{\sigma}_1 \cdot \mathbf{q} \boldsymbol{\sigma}_2 \cdot \mathbf{q} + D_{12} q^2\, \boldsymbol{\sigma}_1 \cdot \mathbf{q} \boldsymbol{\sigma}_2 \cdot \mathbf{q}\, \boldsymbol{\tau}_1 \cdot \boldsymbol{\tau}_2 \\ & + D_{13} q^2\, \boldsymbol{\sigma}_1 \cdot \mathbf{k} \boldsymbol{\sigma}_2 \cdot \mathbf{k} + D_{14} (\boldsymbol{\sigma}_1 \cdot \mathbf{q} \times \mathbf{k})\, (\boldsymbol{\sigma}_2 \cdot \mathbf{q} \times \mathbf{k}) + D_{15} (\boldsymbol{\sigma}_1 \cdot \mathbf{q} \times \mathbf{k})\, (\boldsymbol{\sigma}_2 \cdot \mathbf{q} \times \mathbf{k})\, \boldsymbol{\tau}_1 \cdot \boldsymbol{\tau}_2 \,. \end{aligned} \tag{3.98}$$

This basis can be further reduced, see Ref. [12]. This will, however, not be considered in what follows.

How do these interactions with high order momentum join in the transfer matrix? Perturbatively or non-perturbatively? In Sec. 3.2.3, we have presented how the Lagrangian of the LO interactions leads to the partition funtion and transfer matrix as an evolution operator for a general many-body system, as well as, especially in a two-body system, and how the fundamental pion-nucleon interactive vertex becomes an effective potential depending on the relative positions of the two nucleons.

χEFT allows us to investigate nuclear forces order by order in powers of particle momenta. The LO interactions contribute the most, the next important are included at NLO, and then the N^{2}LO, N^{3}LO and

so on.

In the following Sec. 4, we discuss separately the case of treating non-perturbatively the higher-order contributions, i.e.

$$\begin{aligned} M_{\mathrm{LO}} &= :\exp\left[-H_{\mathrm{f}}-\alpha_{\mathrm{t}}V_{\mathrm{LO}}\right]:, \\ M_{\mathrm{NLO}} &= :\exp\left[-H_{\mathrm{f}}-\alpha_{\mathrm{t}}V_{\mathrm{LO}}-\alpha_{\mathrm{t}}V_{\mathrm{NLO}}\right]:, \\ M_{\mathrm{N^2LO}} &= :\exp\left[-H_{\mathrm{f}}-\alpha_{\mathrm{t}}V_{\mathrm{LO}}-\alpha_{\mathrm{t}}V_{\mathrm{NLO}}-\alpha_{\mathrm{t}}V_{\mathrm{N^2LO}}\right]:, \\ M_{\mathrm{N^3LO}} &= :\exp\left[-H_{\mathrm{f}}-\alpha_{\mathrm{t}}V_{\mathrm{LO}}-\alpha_{\mathrm{t}}V_{\mathrm{NLO}}-\alpha_{\mathrm{t}}V_{\mathrm{N^2LO}}-\alpha_{\mathrm{t}}V_{\mathrm{N^3LO}}\right]:, \end{aligned} \tag{3.99}$$

and the case of a perturbative treatment of these, that is

$$\begin{aligned} M_{\mathrm{LO}} &= :\exp\left[-H_{\mathrm{f}}-\alpha_{\mathrm{t}}V_{\mathrm{LO}}\right]:, \\ M_{\mathrm{NLO}} &= M_{\mathrm{LO}}-\alpha_{\mathrm{t}}\ :V_{\mathrm{NLO}}M_{\mathrm{LO}}:, \\ M_{\mathrm{N^2LO}} &= M_{\mathrm{NLO}}-\alpha_{\mathrm{t}}\ :V_{\mathrm{N^2LO}}M_{\mathrm{LO}}:, \\ M_{\mathrm{N^3LO}} &= M_{\mathrm{N^2LO}}-\alpha_{\mathrm{t}}\ :V_{\mathrm{N^3LO}}M_{\mathrm{LO}}:, \end{aligned} \tag{3.100}$$

where H_{f} represents the kinetic energy of the nucleons, Eq. (3.63), and

$$\begin{aligned} V_{\mathrm{LO}} &= V_{1\pi}+V_{\mathrm{ct},0}\,, \\ V_{\mathrm{NLO}} &= V_{2\pi,2}+V_{\mathrm{ct},2}\,, \\ V_{\mathrm{N^2LO}} &= V_{2\pi,3}\,, \\ V_{\mathrm{N^3LO}} &= V_{2\pi,4}+V_{\mathrm{ct},4}\,. \end{aligned}$$

A perturbative analysis beyond LO is also adopted in practical MC simulations of heavier nuclei.

3.3.1 High Order Contact Interactions in Position Space

We now provide the form of these operators when discretized on a lattice.

Density and current operators

Following Ref. [13, 14], we define the point-like local density operator

$$\rho(\mathbf{n}) \equiv \sum_{i,j} a^{\dagger}_{i,j}(\mathbf{n}) a_{i,j}(\mathbf{n}) \,, \tag{3.101}$$

the local isospin density operator

$$\rho_I(\mathbf{n}) \equiv \sum_{i,j,j'} a^{\dagger}_{i,j}(\mathbf{n}) (\tau_I)_{j,j'} a_{i,j'}(\mathbf{n}) \,, \tag{3.102}$$

the local spin density operator

$$\rho_S(\mathbf{n}) \equiv \sum_{i,i',j} a^{\dagger}_{i,j'}(\mathbf{n}) (\sigma_S)_{i,i'} a_{i',j}(\mathbf{n}) \,, \tag{3.103}$$

and the local isospin-spin density operator

$$\rho_{S,I}(\mathbf{n}) \equiv \sum_{i,i',j,j'} a^{\dagger}_{i,j}(\mathbf{n}) (\sigma_S)_{i,i'} (\tau_I)_{j,j'} a_{i',j'}(\mathbf{n}) \,, \tag{3.104}$$

where σ_S and τ_I denote the Pauli matrices for spin and isospin, respectively. Similarly, we define the current density operator

$$\Pi_l(\mathbf{n}) \equiv \sum_{i,j} a^{\dagger}_{i,j}(\mathbf{n}) \nabla_l a_{i,j}(\mathbf{n}) - \sum_{i,j} \nabla_l a^{\dagger}_{i,j}(\mathbf{n}) a_{i,j}(\mathbf{n}) \,, \tag{3.105}$$

the isospin-current density operator

$$\Pi_{l,I}(\mathbf{n}) \equiv \sum_{i,j,j'} a^{\dagger}_{i,j}(\mathbf{n}) (\tau_I)_{j,j'} \nabla_l a_{i,j'}(\mathbf{n}) - \sum_{i,j,j'} \nabla_l a^{\dagger}_{i,j}(\mathbf{n}) (\tau_I)_{j,j'} a_{i,j'}(\mathbf{n}) \,, \tag{3.106}$$

the spin-current density operator

$$\Pi_{l,S}(\mathbf{n}) \equiv \sum_{i,i',j} a^{\dagger}_{i,j}(\mathbf{n}) (\sigma_S)_{i,i'} \nabla_l a_{i',j}(\mathbf{n}) - \sum_{i,i',j} \nabla_l a^{\dagger}_{i,j}(\mathbf{n}) (\sigma_S)_{i,i'} a_{i',j}(\mathbf{n}) \,, \tag{3.107}$$

and the spin-isospin-current density operator

$$\Pi_{l,S,I}(\mathbf{n}) \equiv \sum_{i,i',j,j'} a^\dagger_{i,j}(\mathbf{n})(\sigma_S)_{i,i'}(\tau_I)_{j,j'}\nabla_l a_{i',j'}(\mathbf{n}) - \sum_{i,i',j,j'} \nabla_l a^\dagger_{i,j}(\mathbf{n})(\sigma_S)_{i,i'}(\tau_I)_{j,j'} a_{i',j'}(\mathbf{n}), \tag{3.108}$$

At leading order

At this order we have the following operators

$$O_1^{(0)} \equiv \frac{1}{2} \; : \sum_{\mathbf{n}} \rho(\mathbf{n})\rho(\mathbf{n}) : , \tag{3.109}$$

$$O_2^{(0)} \equiv \frac{1}{2} \; : \sum_{\mathbf{n}} \sum_{I} \rho_I(\mathbf{n})\rho_I(\mathbf{n}) : , \tag{3.110}$$

At next-to-leading order

As discussed in the previous sections, there are seven independent contact operators with two derivatives at NLO. Here, we use the basis and lattice formulation of Ref. [14], which leads to the following NLO contact operators

$$O_1^{(2)} \equiv -\frac{1}{2} \; : \sum_{\mathbf{n}} \sum_{l} \rho(\mathbf{n})\nabla_l^2\rho(\mathbf{n}) : , \tag{3.111}$$

$$O_2^{(2)} \equiv -\frac{1}{2} \; : \sum_{\mathbf{n}} \sum_{I,l} \rho_I(\mathbf{n})\nabla_l^2\rho_I(\mathbf{n}) : , \tag{3.112}$$

$$O_3^{(2)} \equiv -\frac{1}{2} \; : \sum_{\mathbf{n}} \sum_{S,l} \rho_S(\mathbf{n})\nabla_l^2\rho_S(\mathbf{n}) : , \tag{3.113}$$

$$O_4^{(2)} \equiv -\frac{1}{2} \; : \sum_{\mathbf{n}} \sum_{SI,l} \rho_{S,I}(\mathbf{n})\nabla_l^2\rho_{S,I}(\mathbf{n}) : , \tag{3.114}$$

$$O_5^{(2)} \equiv \frac{1}{2} \; : \sum_{\mathbf{n}} \sum_{S} \nabla_S\rho_S(\mathbf{n}) \sum_{S'} \nabla_{S'}\rho_{S'}(\mathbf{n}) : , \tag{3.115}$$

$$O_6^{(2)} \equiv \frac{1}{2} \; : \sum_{\mathbf{n}} \sum_{S} \nabla_S\rho_{S,I}(\mathbf{n}) \sum_{S'} \nabla_{S'}\rho_{S'}(\mathbf{n}) : , \tag{3.116}$$

$$O_7^{(2)} \equiv -\frac{i}{2} \; : \sum_{\mathbf{n}} \sum_{l,S,l'} \varepsilon_{l,S,l'} \Big[\Pi_l(\mathbf{n})\nabla_{l'}\rho_S(\mathbf{n}) + \Pi_{l,S}(\mathbf{n})\nabla_{l'}\rho(\mathbf{n}) \Big] : , \tag{3.117}$$

where $\Pi_l(\mathbf{n})$ and $\Pi_{l,S}(\mathbf{n})$ denote current density and spin-current density operators.

At next-to-next-to-next-to-leading order

In order to deal with the N^{3}LO contact interactions on the lattice, tensor-current densities are introduced,

$$\begin{aligned}\Pi_{kl}(\mathbf{n}) \equiv & \sum_{i,j} a^\dagger_{i,j}(\mathbf{n})\nabla_k\nabla_l a_{i,j}(\mathbf{n}) - \sum_{i,j} \nabla_k a^\dagger_{i,j}(\mathbf{n})\nabla_l a_{i,j}(\mathbf{n}) \\ & - \sum_{i,j} \nabla_l a^\dagger_{i,j}(\mathbf{n})\nabla_k a_{i,j}(\mathbf{n}) + \sum_{i,j} \nabla_k\nabla_l a^\dagger_{i,j}(\mathbf{n}) a_{i,j}(\mathbf{n}) \,, \end{aligned} \tag{3.118}$$

$$\begin{aligned}\Pi_{kl,S}(\mathbf{n}) \equiv & \sum_{i,i',j} a^\dagger_{i,j}(\mathbf{n})(\sigma_S)_{i,i'}\nabla_k\nabla_l a_{i',j}(\mathbf{n}) - \sum_{i,i',j} \nabla_k a^\dagger_{i,j}(\mathbf{n})(\sigma_S)_{i,i'}\nabla_l a_{i',j}(\mathbf{n}) \\ & - \sum_{i,i',j} \nabla_l a^\dagger_{i,j}(\mathbf{n})(\sigma_S)_{i,i'}\nabla_k a_{i',j}(\mathbf{n}) + \sum_{i,i',j} \nabla_k\nabla_l a^\dagger_{i,j}(\mathbf{n})(\sigma_S)_{i,i'} a_{i',j}\mathbf{n}) \,, \end{aligned} \tag{3.119}$$

$$\begin{aligned}\Pi_{kl,I}(\mathbf{n}) \equiv & \sum_{i,j,j'} a^\dagger_{i,j}(\mathbf{n})(\tau_I)_{j,j'}\nabla_k\nabla_l a_{i,j'}(\mathbf{n}) - \sum_{i,j,j'} \nabla_k a^\dagger_{i,j}(\mathbf{n})(\tau_I)_{j,j'}\nabla_l a_{i,j'}(\mathbf{n}) \\ & - \sum_{i,j,j'} \nabla_l a^\dagger_{i,j}(\mathbf{n})(\tau_I)_{j,j'}\nabla_k a_{i,j'}(\mathbf{n}) + \sum_{i,j,j'} \nabla_k\nabla_l a^\dagger_{i,j}(\mathbf{n})(\tau_I)_{j,j'} a_{i,j'}\mathbf{n}) \,, \end{aligned} \tag{3.120}$$

$$\begin{aligned}\Pi_{kl,S,I}(\mathbf{n}) \equiv & \sum_{i,i',j,j'} a^\dagger_{i,j}(\mathbf{n})(\sigma_S)_{i,i'}(\tau_I)_{j,j'}\nabla_k\nabla_l a_{i',j'}(\mathbf{n}) - \sum_{i,i',j,j'} \nabla_k a^\dagger_{i,j}(\mathbf{n})(\sigma_S)_{i,i'}(\tau_I)_{j,j'}\nabla_l a_{i',j'}(\mathbf{n}) \\ & - \sum_{i,i',j,j'} \nabla_l a^\dagger_{i,j}(\mathbf{n})(\sigma_S)_{i,i'}(\tau_I)_{j,j'}\nabla_k a_{i',j'}(\mathbf{n}) + \sum_{i,i',j,j'} \nabla_k\nabla_l a^\dagger_{i,j}(\mathbf{n})(\sigma_S)_{i,i'}(\tau_I)_{j,j'} a_{i',j'}\mathbf{n}) \,, \end{aligned} \tag{3.121}$$

Based upon these tensor-current densities, as well as the local densities and current densities operators, we obtain the contact interactions at order Q^4 on the lattice

$$O^{(4)}_1 \equiv \frac{1}{2} \; : \sum_{\mathbf{n}} \sum_{kl} \rho(\mathbf{n})\nabla_k^2\nabla_l^2\rho(\mathbf{n}) : \,, \tag{3.122}$$

$$O^{(4)}_2 \equiv \frac{1}{2} \; : \sum_{\mathbf{n}} \sum_{I,kl} \rho_I(\mathbf{n})\nabla_k^2\nabla_l^2\rho_I(\mathbf{n}) : \,, \tag{3.123}$$

$$O^{(4)}_3 \equiv \frac{1}{2} \; : \sum_{\mathbf{n}} \sum_{S,kl} \rho_S(\mathbf{n})\nabla_k^2\nabla_l^2\rho_S(\mathbf{n}) : \,, \tag{3.124}$$

$$O^{(4)}_4 \equiv \frac{1}{2} \; : \sum_{\mathbf{n}} \sum_{SI,kl} \rho_{S,I}(\mathbf{n})\nabla_k^2\nabla_l^2\rho_{S,I}(\mathbf{n}) : \,, \tag{3.125}$$

$$O^{(4)}_5 \equiv \frac{1}{4} \; : \sum_{\mathbf{n}} \sum_{kl} \Big[\Pi_{kl}(\mathbf{n})\nabla_k\nabla_l\rho(\mathbf{n}) + \nabla_k\Pi_l(\mathbf{n})\nabla_l\Pi_k(\mathbf{n}) \Big] : \,, \tag{3.126}$$

$$O^{(4)}_6 \equiv \frac{1}{4} \; : \sum_{\mathbf{n}} \sum_{I,kl} \Big[\Pi_{kl,I}(\mathbf{n})\nabla_k\nabla_l\rho_I(\mathbf{n}) + \nabla_k\Pi_{l,I}(\mathbf{n})\nabla_l\Pi_{k,I}(\mathbf{n}) \Big] : \,, \tag{3.127}$$

$$O_7^{(4)} \equiv \frac{1}{4} \; : \sum_{\mathbf{n}} \sum_{S,kl} \Big[\Pi_{kl,S}(\mathbf{n}) \nabla_k \nabla_l \rho_S(\mathbf{n}) + \nabla_k \Pi_{l,S}(\mathbf{n}) \nabla_l \Pi_{k,S}(\mathbf{n}) \Big] : , \tag{3.128}$$

$$O_8^{(4)} \equiv \frac{1}{4} \; : \sum_{\mathbf{n}} \sum_{SI,kl} \Big[\Pi_{kl,SI}(\mathbf{n}) \nabla_k \nabla_l \rho_{SI}(\mathbf{n}) + \nabla_k \Pi_{l,SI}(\mathbf{n}) \nabla_l \Pi_{k,SI}(\mathbf{n}) \Big] : , \tag{3.129}$$

$$O_9^{(4)} \equiv -\frac{i}{2} \; : \sum_{\mathbf{n}} \sum_{k,lSl'} \varepsilon_{l,S,l'} \Big[\Pi_l(\mathbf{n}) \nabla_k^2 \nabla_{l'} \rho_S(\mathbf{n}) + \Pi_{l,S}(\mathbf{n}) \nabla_k^2 \nabla_{l'} \rho(\mathbf{n}) \Big] : , \tag{3.130}$$

$$O_{10}^{(4)} \equiv -\frac{i}{2} \; : \sum_{\mathbf{n}} \sum_{I,k,lSl'} \varepsilon_{l,S,l'} \Big[\Pi_{l,I}(\mathbf{n}) \nabla_k^2 \nabla_{l'} \rho_{S,I}(\mathbf{n}) + \Pi_{l,S,I}(\mathbf{n}) \nabla_k^2 \nabla_{l'} \rho_I(\mathbf{n}) \Big] : , \tag{3.131}$$

$$O_{11}^{(4)} \equiv \frac{1}{2} \; : \sum_{\mathbf{n}} \sum_{l,S,S'} \nabla_S \rho_S(\mathbf{n}) \nabla_l^2 \nabla_{S'} \rho_{S'}(\mathbf{n}) : , \tag{3.132}$$

$$O_{12}^{(4)} \equiv \frac{1}{2} \; : \sum_{\mathbf{n}} \sum_{l,I,S,S'} \nabla_S \rho_{S,I}(\mathbf{n}) \nabla_l^2 \nabla_{S'} \rho_{S',I}(\mathbf{n}) : , \tag{3.133}$$

$$O_{13}^{(4)} \equiv -\frac{1}{8} \; : \sum_{\mathbf{n}} \sum_{l,S,S'} \Big[\Pi_{S;S}(\mathbf{n}) \nabla_l^2 \Pi_{S';S'}(\mathbf{n}) + \Pi_{S;S'}(\mathbf{n}) \nabla_l^2 \Pi_{S';S}(\mathbf{n}) - 2\, \Pi_{SS';S}(\mathbf{n}) \nabla_l^2 \rho_{S'}(\mathbf{n}) \Big] : , \tag{3.134}$$

$$\begin{aligned} O_{14}^{(4)} \equiv \frac{1}{8} \; : \sum_{\mathbf{n}} \sum_{ijS,klS'} \varepsilon_{ijS} \varepsilon_{klS'} \Big[& \Pi_{jl,S}(\mathbf{n}) \nabla_i \nabla_k \rho_{S'}(\mathbf{n}) + \Pi_{jl,S'}(\mathbf{n}) \nabla_i \nabla_k \rho_S(\mathbf{n}) \\ & + \nabla_i \Pi_{jl,S}(\mathbf{n}) \nabla_k \rho_{S'}(\mathbf{n}) + \nabla_i \Pi_{jl,S'}(\mathbf{n}) \nabla_k \rho_S(\mathbf{n}) \Big] : , \end{aligned} \tag{3.135}$$

$$\begin{aligned} O_{15}^{(4)} \equiv \frac{1}{8} \; : \sum_{\mathbf{n}} \sum_{I,ijS,klS'} \varepsilon_{ijS} \varepsilon_{klS'} \Big[& \Pi_{jl,S,I}(\mathbf{n}) \nabla_i \nabla_k \rho_{S',I}(\mathbf{n}) + \Pi_{jl,S',I}(\mathbf{n}) \nabla_i \nabla_k \rho_{S,I}(\mathbf{n}) \\ & + \nabla_i \Pi_{jl,S,I}(\mathbf{n}) \nabla_k \rho_{S',I}(\mathbf{n}) + \nabla_i \Pi_{jl,S',I}(\mathbf{n}) \nabla_k \rho_{S,I}(\mathbf{n}) \Big] : , \end{aligned} \tag{3.136}$$

3.3.2 Contact Interactions in Spherical Harmonic Basis

In this section, the contact operators are reconstructed in a spherical harmonic basis. Operators in this form can be easily projected onto specific angular momenta, which is convenient when comparing with experimental NN scattering data that are separated into different partial waves.

At order Q^{2N} there are totally $2N$ momenta p or p' multiplied together in the amplitude of each operator. For the sake of maintaining rotational invarience, $\mathbf{p}$ and $\mathbf{p}'$ have to be combined to generate a basis of representations of the rotation group SO(3). It is natural to construct this basis from spherical harmonics.

Let us define $a_{i,j,\mathbf{p}}$ and $a^\dagger_{i,j,\mathbf{p}}$ as the lattice annihilation and creation operators for a specific momentum state with spin $i = 0, 1$ (up, down) and isospin $j = 0, 1$ (proton, neutron). The operator $[a_{\mathbf{p}}]_{S,S_z;I,I_z}$ is

combination of $\{a_{ij,\mathbf{p}}\}$ which has some certain total spin and isospin.

$$[a_{\mathbf{p}}]_{S,S_z;I,I_z} = \sum_{ii'jj'} a_{ij,\mathbf{p}} M_{ii'}(S,S_z) M_{jj'}(I,I_z) a_{i'j',-\mathbf{p}} \,. \tag{3.137}$$

with

$$M_{ii'}(0,0) = \frac{1}{\sqrt{2}}[\delta_{i0}\delta_{i'1} - \delta_{i1}\delta_{i'0}] \tag{3.138}$$

$$M_{ii'}(1,0) = \frac{1}{\sqrt{2}}[\delta_{i0}\delta_{i'1} + \delta_{i1}\delta_{i'0}] \tag{3.139}$$

$$M_{ii'}(1,1) = \delta_{i0}\delta_{i'0} \tag{3.140}$$

$$M_{ii'}(1,-1) = \delta_{i1}\delta_{i'1} \,. \tag{3.141}$$

We define

$$[O_{\mathbf{p}}]^{2M}_{S,L,J,J_z;I,I_z} = \sum_{S_z L_z} C^{J,J_z}_{L,L_z,S,S_z} [P_{\mathbf{p}}]^{2M}_{S,S_z;L,L_z;I,I_z} \tag{3.142}$$

$$[P_{\mathbf{p}}]^{2M}_{S,S_z;L,L_z;I,I_z} = p^{2M} R^*_{L,L_z}(\mathbf{p})\, [a_{\mathbf{p}}]_{S,S_z;I,I_z} \,. \tag{3.143}$$

with the spherical solid harmonics

$$R_{L,L_z}(\mathbf{p}) = \sqrt{\frac{4\pi}{2L+1}} p^L Y_{L,L_z}(\theta,\phi) \,. \tag{3.144}$$

and Clebsch-Gordan (CG) coefficiencts C^{J,J_z}_{L,L_z,S,S_z}. The even integer $2M$ gives higher powers of the momentum.

A set of CTs on the basis of spherical harmonics is constructed as:

$$[V_{2N}]^{\{2m_o,2m_i\}}_{S,I,I_z,J,J_z;\{L_o,L_i\}}(\mathbf{p}',\mathbf{p}) = \frac{1}{2}\left(\left[O_{\mathbf{p}'}\right]^{2m_o}_{S,L_o,J,J_z;I,I_z}\right)^\dagger \left[O_{\mathbf{p}}\right]^{2m_i}_{S,L_i,J,J_z;I,I_z} + \frac{1}{2}\left\{(L_o,m_o) \leftrightarrow (L_i,m_i)\right\} \,. \tag{3.145}$$

A specific operator is completely characterized by a set of quantum numbers (J,S,I,L_i,L_o,m_i,m_o), where J ,S and I are total angular momentum, total spin and total isospin. L_i and L_o are orbital momentum. m_i and m_o provide necessary powers of momentum. The subindex i and o denote incoming and outgoing states of the scattering process, respectively. Note that J,S,I are good quantum numbers, whereas L_i and L_o can be different for the spin-triplet case where different orbital state are mixed due to the spin-orbital

coupling, such as ${}^3\mathrm{S}_1 - {}^3\mathrm{D}_1$ and ${}^3\mathrm{P}_2 - {}^3\mathrm{F}_2$. In addition, due to the odd parity of the two-particle system, the total isospin I can be obtained from the parities of total spin S and orbital momentum L.

We are interested in how many groups of quantum numbers $(J, S, I, L_\mathrm{i}, L_\mathrm{o}, m_\mathrm{i}, m_\mathrm{o})$ there exist at any Q^{2N}. They have to satisfy the following conditions that

$$\begin{aligned}
&2N = 2m_\mathrm{i} + L_\mathrm{i} + 2m_\mathrm{o} + L_\mathrm{o} \\
&\text{if } S = 0, \text{then } \begin{cases} L_\mathrm{o} = L_\mathrm{i} \\ J = L_\mathrm{i} \end{cases} \\
&\text{if } S = 1 \text{ and } L_\mathrm{o} = L_\mathrm{i}, \text{then } J = \{L_\mathrm{i} + 1, L_\mathrm{i}, L_\mathrm{i} - 1\} \\
&\text{if } S = 1 \text{ and } |L_\mathrm{i} - L_\mathrm{o}| = 2, \text{then } J = (L_\mathrm{i} + L_\mathrm{o})/2
\end{aligned} \tag{3.146}$$

At Q^0, Q^2, Q^4, there are 2, 7 and 15 independent operators respectively. All of the cases are listed in Tab. 3.2. Generally, the number of independent operators at order Q^{2N} is $(N + 1)(3N + 4)/2$. This respresentation of the operators into the angular momentum basis with spin and isospin structure $\mathbf{q}, \mathbf{k}, \sigma, \tau$ is exactly equivalent in the continuum limit. The coefficients of CTs are therefore linearly dependent. Taking the LO terms as an example

$$V_{\mathrm{ct},0} = C_0 + C_\mathrm{I} \boldsymbol{\tau}_1 \cdot \boldsymbol{\tau}_2 \,, \tag{3.147}$$

when in the angular momentum basis, the form will be taken as

$$V_{\mathrm{ct},0} = C_{0,{}^1\mathrm{S}_0} [V_0]^{\{0,0\}}_{0,1,Iz,0,0;\{0,0\}} + C_{0,{}^3\mathrm{S}_1} [V_0]^{\{0,0\}}_{1,0,0,1,J_z;\{0,0\}} \,. \tag{3.148}$$

They satisfy a simple relation that

$$\begin{bmatrix} C_0 \\ C_\mathrm{I} \end{bmatrix} = 4\pi \begin{bmatrix} 3/4 & 1/4 \\ 1/4 & -1/4 \end{bmatrix} \begin{bmatrix} C_{0,{}^1\mathrm{S}_0} \\ C_{0,{}^3\mathrm{S}_1} \end{bmatrix}, \tag{3.149}$$

so are the higher order coefficients. Using the improved definition of momentum on a lattice with finite spacing, Eq. (3.1), the relation between transfer/average momentum $\mathbf{q}, \mathbf{k}$ and initial/final momentum $\mathbf{p}, \mathbf{p}'$ becomes complicated for that $\sin q \neq \sin p' - \sin p$ simply, despite that $q = p' - p$. The dependence of coeffients in angular momentum basis on ones in spin-isospin basis is not linear any more. Fortunately

Table 3.2: Operator basis for the contact interactions at various orders.

Q^{2N}	S	J	L_o	L_i	$2m_\mathrm{o}$	$2m_\mathrm{i}$
Q^0	0	0	0	0	0	0
	1	1	0	0	0	0
Q^2	0	0	0	0	2	0
	0	1	1	1	0	0
	1	1	0	0	2	0
	1	0	1	1	0	0
	1	1	1	1	0	0
	1	2	1	1	0	0
	1	1	2	0	0	0
Q^4	0	0	0	0	4	0
	0	0	0	0	2	2
	0	1	1	1	2	0
	0	2	2	2	0	0
	1	1	0	0	4	0
	1	1	0	0	2	2
	1	0	1	1	2	0
	1	1	1	1	2	0
	1	2	1	1	2	0
	1	1	2	2	0	0
	1	2	2	2	0	0
	1	3	2	2	0	0
	1	1	2	0	2	0
	1	1	2	0	0	2
	1	2	3	1	0	0

the linear relationship will be restored when we take the lattice spacing to zero. This limit is, however, actually not taken, so one must deal with these artefacts as described e.g. in Ref. [15].

3.4 Two-Body Scattering on the Lattice

In this section, we investigate the transfer matrix of the NN system from which we obtain properties of the NN scattering states.

3.4.1 Hamiltonian Projection onto the Spherical Harmonic Basis

We have the form of the Hamiltonian, as well as the transfer matrix, of the nucleonic system on the lattice including any information for observable quantities. We are interested in spectrum so that diagnolizing

the transfer matrix is a feasible path to those physical states but not elegent for the huge dimension of matrix $\sim L^3 \times L^3 \times \ldots$.

The case for two-body systems seems clear: due to rotational invariance, the eigenstates of the Hamiltonian are degenerate with numerous degrees of freedom. We classify those position bases $\{|\mathbf{r}\rangle\}$ playing symmetric roles under rotational transformation to separate redundancy. The new basis set is characterized by the representation of a SO(3) group, namely angular momentum.

Let $|\mathbf{n}\rangle \otimes |S_z\rangle$ be the NN scattering state with lattice separation vector $\mathbf{n}$ and z-component of total intrinsic spin S_z. We define radial coordinates on the lattice by grouping together lattice mesh points with the same radial distance to define radial position states and project onto states with total angular momentum J, J_z in the continuum limit, see Ref. [16]. Using spherical harmonics Y_{ℓ,ℓ_z} with orbital angular momentum ℓ, ℓ_z and Clebsch-Gordan coefficients $C^{J,J_z}_{\ell,\ell_z,S,S_z}$, we define

$$|r\rangle_L^{J,J_z} = \sum_{\mathbf{r}',\ell_z,S_z} C^{J,J_z}_{\ell,\ell_z,S,S_z} Y_{\ell,\ell_z}(\hat{\mathbf{r}}')\delta_{r,|\mathbf{r}'|}|\mathbf{r}'\rangle \otimes |S_z\rangle, \tag{3.150}$$

where $\delta_{r,|\mathbf{r}'|}$ is a Kronecker delta function that selects lattice points where $|\mathbf{r}'| = r$. The Hamiltonian is reducible into a sparse matrix as compared to the case using the normal position basis,

$$H \to H^{J,J_z}_{r',r} = \begin{bmatrix} {}^{J,J_z}_{J-1}\langle r'|H|r\rangle^{J,J_z}_{J-1} & {}^{J,J_z}_{J-1}\langle r'|H|r\rangle^{J,J_z}_{J+1} \\ {}^{J,J_z}_{J+1}\langle r'|H|r\rangle^{J,J_z}_{J-1} & {}^{J,J_z}_{J+1}\langle r'|H|r\rangle^{J,J_z}_{J+1} \end{bmatrix} \tag{3.151}$$

3.4.2 Spherical Wall Method to Determine Phase Shift on the Lattice

In the CM frame, a two-body nonrelativistic system can have several discrete bound states ($E < 0$) and a continuum of scattering states ($E > 0$). Phase shifts can be extracted from the wave functions which include all information of the collision and has an asymptotic behavior of a spherical wave at distances large compared to the range of interactions.

Lüscher's formula [17–20], widely used in lattice QCD, relates the S-wave scattering phase shifts to the energy levels below the inelastic threshold calculated within a finite cubic volume. There also exists extensions of Lüscher's formular for higher partial waves, see Ref. [21].

In a spherical wave case, phase shifts are determined when the wave function propagates to the asymptotical region, greater than the range of interactions and less than the lattice size, see Ref. [22]

$$\psi(\mathbf{r}) \cong Ah_J^-(kr) - Bh_J^+(kr)\,, \tag{3.152}$$

Where k is linked with energy lever by $E = k^2/m$. A,B, which is obtained by least square fitting and satisfies the simple relation $B = SA$ with S indicating the scattering matrix, $S = e^{2i\delta_J}$.

In the spin triplet case, spin-orbit coupling generates mixing between partial waves states of similar parity, but separated by two units of angular momentum, e.g. S-D wave, P-F wave, D-G wave, ... ψ has two compoents with orbital quantum number $L = J \pm 1$, both behave as a spherical bessel function at asymmptotical region,

$$\psi(\mathbf{r}) \cong \begin{bmatrix} A_{J-1}h^-_{J-1}(kr) \\ A_{J+1}h^-_{J+1}(kr) \end{bmatrix} - \begin{bmatrix} B_{J-1}h^+_{J-1}(kr) \\ B_{J+1}h^+_{J+1}(kr) \end{bmatrix}. \tag{3.153}$$

In the Stapp parameteriztion Ref. [23], the scattering matrix S takes the form as

$$S = \begin{bmatrix} \exp(i\delta_{J-1}) & \\ & \exp(i\delta_{J+1}) \end{bmatrix} \times \begin{bmatrix} \cos(2\epsilon_1) & i\sin(2\epsilon_1) \\ i\sin(2\epsilon_1) & \cos(2\epsilon_1) \end{bmatrix} \times \begin{bmatrix} \exp(i\delta_{J-1}) & \\ & \exp(i\delta_{J+1}) \end{bmatrix} \tag{3.154}$$

For each total angular momentum J, there exists a pair of independent wave functions $\{\psi, \psi'\}$ degenerate for spin-orbital coupling, so that we have

$$\begin{bmatrix} A_{J-1}A'_{J-1} \\ A_{J+1}A'_{J+1} \end{bmatrix} = S \begin{bmatrix} B_{J-1}B'_{J-1} \\ B_{J+1}B'_{J+1} \end{bmatrix}. \tag{3.155}$$

and then $S = (BB')(AA')^{-1}$

In practice it is not necessary to determine the complete set of eigenstates of the system. What we need is a series of typical sampling points on the diagram of phase shifts vs. energy levels. Thus we impose a hard spherical wall potential as a "pick-up" machine at some large enough separation of nucleons, R_{wall}, to calculate lattice phase shifts, Ref. [22, 24], see Fig. 3.3(a).

$$V_{\text{wall}}(r) = \begin{cases} 0, & \text{if } r < R_{\text{wall}}\ ; \\ \infty, & \text{else}\ . \end{cases} \tag{3.156}$$

After entering the wall, the spectrum of the nucleonic system shrinks to a subset of the original one, for the wall removes the copies of the interactions arising from the periodic boundaries of the lattice and suppresses those of scattering states which are still dancing at the foot of the wall, while but not influencing their behavior inside. Certainly the wall does not exist, it is a fictitious "pick-up" tool so that

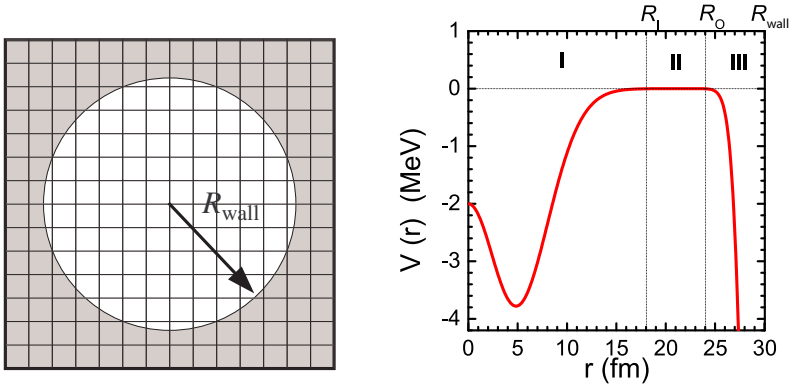

(a) (b)

Figure 3.3: (a)spherical wall (b)Auxiliary potential for the improved spherical wall as described in the text.

we may adjust the position of the wall to extract another set of the scattering states.

3.4.3 More on the Spherical Wall Method

In Ref. [16], the distance between two particles are divided into 3 parts, see Fig. 3.3(b). The innermost (labeled by Region I) is interactive region where the particles influence each other. The intermediate (labeled by Region II) is asymptotical region where the distance of two particles is large enough so that the interaction between them vanishes Although this region II may extend to infinite, an extra potential can be imposed artificially outside the intermediate region, labeled by Region III, which serves as a filter without change of the inner part.

In the case that the potential in Region III does not exist, the 2-particle system has a continuous spectrum of scattering states in continuous space or has a relatively high-dense spectrum on a lattice. Choosing a specific potential in Region III has no impact on interactive region and asymptotical region but picks up several certain energy levels due to the boundary restriction in Region III.

As described in Ref. [16], we impose a hard spherical wall boundary at some large radius R_{wall} and a smooth auxiliary Gaussian potential in front of the wall, which we call $V_{\text{aux}}(r)$. The auxiliary potential has the form

$$V_{\text{aux}}(r) = V_0 \exp\left[-(r - R_{\text{wall}})^2\right] , \tag{3.157}$$

with adjustable coefficient V_0 that is used to probe different values of the scattering energy. The auxiliary potential is non-negligible only when r is a few lattice units away from the wall at R_{wall}. We determine the

asymptotic phase shifts from the radial wave function at points where r is large but $V_{\text{aux}}(r)$ is negligible. For coupled partial waves such as the ${}^3\text{S}_1 - {}^3\text{D}_1$ channel, we determine the two phase shifts and mixing angle using an additional auxiliary potential $U_{\text{aux}}(r)$ with the same functional form as $V_{\text{aux}}(r)$, but with imaginary Hermitian off-diagonal couplings between the two partial waves,

$$\begin{bmatrix} 0 & iU_{\text{aux}}(r) \\ -iU_{\text{aux}}(r) & 0 \end{bmatrix}. \tag{3.158}$$

This complex-valued auxiliary potential breaks time-reversal invariance and allows us to extract information about the two independent phase shifts and mixing angle from the real and imaginary parts of the complex-valued wave functions.

CHAPTER 4

Scattering of Two Nucleons: Numerical Result

In this section[1], the LECs of the NN force at LO, NLO and N^{2}LO in nuclear lattice EFT (NLEFT) are determined by means of a chi-square (χ^2) minimization with respect to np phase shifts and mixing angles. This procedure allows us to provide quantitative estimates of the uncertainties of the NLO constants in the scheme of NLEFT, along with estimates of their systematical errors and the impact of such errors on the binding energies of nuclei. The LO interaction consists of smeared, local CTs and static OPE. We show results for a fully non-perturbative analysis up to N^{2}LO, followed by a perturbative treatment of contributions beyond LO. The pioneering calculations of Ref. [13, 14] (and almost all calcuations of nuclear properties) were performed with a coarse lattice spacing of $a = 1.97$ fm, which corresponds to a relatively low momentum cutoff of $\pi/a = 314$ MeV [2]. We also study the effects of decreasing the lattice spacing to $a \simeq 1$ fm, which greatly decreases the impact of lattice artifacts and systematical errors, and discuss the possibility of further improving the lattice action to decrease remaining discretization effects. The first study of discretization errors and lattice spacing variation at LO has been performed in Ref. [27]. In prior work at $a = 1.97$ fm, the TPE potential at NLO and N^{2}LO contributions were integrated out by means of a Taylor expansion in powers of $q/2M_\pi$. Since we now use lattice spacings as small as $a \simeq 1$ fm, the full structure of the TPE potential needs to be included.

[1] This section is based on the publication [25].

[2] Note that such soft nucleon-nucleon interactions lead to better convergence properties in the calculations of many-nucleon systems and nuclear matter, see e.g. [26].

4.1 Lattice Notations

The free part of NN Hamiltonian is given by [13]

$$
\begin{aligned}
H_{\text{free}} \equiv & \frac{6\omega_0}{2m_{\text{N}}} \sum_{\mathbf{n}} \sum_{i,j=0,1} a^{\dagger}_{i,j}(\mathbf{n}) a_{i,j}(\mathbf{n}) \\
& - \frac{\omega_1}{2m_{\text{N}}} \sum_{\mathbf{n}} \sum_{l=1}^{3} \sum_{i,j=0,1} a^{\dagger}_{i,j}(\mathbf{n}) \Big[a_{i,j}(\mathbf{n}+\hat{e}_l) + a_{i,j}(\mathbf{n}-\hat{e}_l) \Big] \\
& + \frac{\omega_2}{2m_{\text{N}}} \sum_{\mathbf{n}} \sum_{l=1}^{3} \sum_{i,j=0,1} a^{\dagger}_{i,j}(\mathbf{n}) \Big[a_{i,j}(\mathbf{n}+2\hat{e}_l) + a_{i,j}(\mathbf{n}-2\hat{e}_l) \Big] \\
& - \frac{\omega_3}{2m_{\text{N}}} \sum_{\mathbf{n}} \sum_{l=1}^{3} \sum_{i,j=0,1} a^{\dagger}_{i,j}(\mathbf{n}) \Big[a_{i,j}(\mathbf{n}+3\hat{e}_l) + a_{i,j}(\mathbf{n}-3\hat{e}_l) \Big] ,
\end{aligned}
\tag{4.1}
$$

where the $\hat{e}_l$ with $l = 1, 2, 3$ are unit vectors in the spatial directions, and m_{N} is the nucleon mass. Here we introduce the so-called stretched action to correct the lattice dispersion relation so as not to diviate from continuum too much, see Ref. [28]. The stretched hopping coefficients are defined in terms of the $O(a^4)$- and $O(a^2)$-improved hopping coefficients, see Table 3.1,

$$
\omega_k^{\text{str}} \equiv \omega_k^{(2)} + \mathcal{N} \left(\omega_k^{(2)} - \omega_k^{(1)} \right) , \tag{4.2}
$$

where $\mathcal{N} = 10$ is adopted in this study.

Ref. [13] showed that an on-site interaction such as those in Eq. (3.109) and (3.110) do not suffice to provide a favorable description of the S-wave phase shifts except at very low momenta. Hence, smeared contact operators were introduced according to

$$
O_1^{(0)} \to \frac{1}{2L^3} : \sum_{\mathbf{q}} f(\mathbf{q}) \rho(\mathbf{q}) \rho(-\mathbf{q}) : \tag{4.3}
$$

and

$$
O_2^{(0)} \to \frac{1}{2L^3} : \sum_{\mathbf{q}} f(\mathbf{q}) \rho_I(\mathbf{q}) \rho_I(-\mathbf{q}) : , \tag{4.4}
$$

where the smearing factor $f(\mathbf{q})$ is

$$
f(\mathbf{q}) \equiv f_0^{-1} \exp\left(-b_{\text{s}} \frac{\mathbf{q}^4}{4} \right) , \tag{4.5}
$$

with b_s an adjustable parameter detemined in the fit procedure, and normalized by

$$f_0 \equiv \frac{1}{L^3}\sum_{\mathbf{q}} \exp\left(-b_s \frac{\mathbf{q}^4}{4}\right) \tag{4.6}$$

with

$$\begin{aligned}\frac{\mathbf{q}^2}{2} \equiv & \sum_{l=1}^{3}\left[\omega_0 - \omega_1 \cos\left(\frac{2\pi}{L}q_l\right) + \omega_2 \cos\left(\frac{4\pi}{L}q_l\right)\right. \\ & \left. - \omega_3 \cos\left(\frac{6\pi}{L}q_l\right)\right],\end{aligned} \tag{4.7}$$

where the q_l are lattice momentum components, and the $O(a^4)$-improved hopping coefficients ω_i are listed in Table 3.1.

In the analysis of the Ref. [29], smeared contact operators were found to dramatically improve the convergence of the NLEFT expansion in the S-wave channels, at the price of introducing unwanted attractive forces in the P-wave channels. By means of the projection operators [30],

$$P^{(0,1)} \equiv \left(\frac{1}{4} - \frac{\boldsymbol{\sigma}_1\cdot\boldsymbol{\sigma}_2}{4}\right)\left(\frac{3}{4} + \frac{\boldsymbol{\tau}_1\cdot\boldsymbol{\tau}_2}{4}\right), \tag{4.8}$$

$$P^{(1,0)} \equiv \left(\frac{3}{4} + \frac{\boldsymbol{\sigma}_1\cdot\boldsymbol{\sigma}_2}{4}\right)\left(\frac{1}{4} - \frac{\boldsymbol{\tau}_1\cdot\boldsymbol{\tau}_2}{4}\right), \tag{4.9}$$

for the $(S, I) = (0, 1)$ and $(1, 0)$ channels, good agreement at LO in the P-wave channels can be recovered (although a similar problem of unwanted forces in the D-wave channels persists). In the present work, we use the corresponding smeared LO contact operators

$$\begin{aligned}O^{(0)}_{(0,1)} \equiv & \frac{3}{32L^3} : \sum_{\mathbf{q}} f(\mathbf{q})\,\rho(\mathbf{q})\,\rho(-\mathbf{q}) : - \frac{3}{32L^3} : \sum_{\mathbf{q}} f(\mathbf{q}) \sum_{S} \rho_S(\mathbf{q})\,\rho_S(-\mathbf{q}) : \\ & + \frac{1}{32L^3} : \sum_{\mathbf{q}} f(\mathbf{q}) \sum_{I} \rho_I(\mathbf{q})\,\rho_I(-\mathbf{q}) : - \frac{1}{32L^3} : \sum_{\mathbf{q}} f(\mathbf{q}) \sum_{S,I} \rho_{S,I}(\mathbf{q})\,\rho_{S,I}(-\mathbf{q}) : ,\end{aligned} \tag{4.10}$$

for $(S, I) = (0, 1)$, and

$$\begin{aligned}O^{(0)}_{(1,0)} \equiv & \frac{3}{32L^3} : \sum_{\mathbf{q}} f(\mathbf{q})\,\rho(\mathbf{q})\,\rho(-\mathbf{q}) : + \frac{1}{32L^3} : \sum_{\mathbf{q}} f(\mathbf{q}) \sum_{S} \rho_S(\mathbf{q})\,\rho_S(-\mathbf{q}) : \\ & - \frac{3}{32L^3} : \sum_{\mathbf{q}} f(\mathbf{q}) \sum_{I} \rho_I(\mathbf{q})\,\rho_I(-\mathbf{q}) : - \frac{1}{32L^3} : \sum_{\mathbf{q}} f(\mathbf{q}) \sum_{S,I} \rho_{S,I}(\mathbf{q})\,\rho_{S,I}(-\mathbf{q}) : ,\end{aligned} \tag{4.11}$$

for $(S, I) = (1, 0)$, where $\rho_S(\mathbf{n})$ and $\rho_{S,I}(\mathbf{n})$ are local spin density and local spin-isospin density operators, defined in Sec. 3.3.1. The NLO CTs are taken as Eq. (3.111) – (3.116) except the spin-orbit operator $O_7^{(2)}$ projected onto $I = 1$ following the treatment of Ref. [14],

$$\begin{aligned} O_7^{(2)} \;\rightarrow\; -\frac{i}{2}\Bigg[\frac{3}{4} : \sum_{\mathbf{n}} \sum_{l,S,l'} \varepsilon_{l,S,l'} \Big(\Pi_l(\mathbf{n}) \nabla_{l'} \rho_S(\mathbf{n}) + \Pi_{l,S}(\mathbf{n}) \nabla_{l'} \rho(\mathbf{n})\Big) : \\ + \frac{1}{4} : \sum_{\mathbf{n}} \sum_{l,S,l',I} \varepsilon_{l,S,l'} \Big(\Pi_{l,I}(\mathbf{n}) \nabla_{l'} \rho_{S,I}(\mathbf{n}) + \Pi_{l,S,I}(\mathbf{n}) \nabla_{l'} \rho_I(\mathbf{n})\Big) : \Bigg] , \end{aligned} \tag{4.12}$$

which eliminates lattice artifacts in the $S = 1$ even-parity channels. For the derivative operator ∇_l in the NLO CTs, we use a simplified definition

$$\nabla_l f(\mathbf{n}) \equiv \frac{1}{2}[f(\mathbf{n} + a\hat{e}_l) - f(\mathbf{n} - a\hat{e}_l)] , \tag{4.13}$$

where a is the spatial lattice spacing, and $\hat{e}_l$ is a unit vector in spatial direction l. For the double derivative operator ∇_l^2, we take

$$\nabla_l^2 f(\mathbf{n}) \equiv \nabla_l[\nabla_l f(\mathbf{n})] = \frac{1}{4}[f(\mathbf{n} + 2a\hat{e}_l) + f(\mathbf{n} - 2a\hat{e}_l) - 2f(\mathbf{n})] . \tag{4.14}$$

In the radial transfer matrix formalism, we project each of the NLO contact operators onto the NN partial waves under consideration, such that V_X^i is the matrix element of operator i in channel X. If we denote the complete set of NLO contact interactions by $V_{\rm ct}^{(2)}$, we find

$$\langle {}^1\mathrm{S}_0 | V_{\rm ct}^{(2)} | {}^1\mathrm{S}_0 \rangle = \widetilde{C}_1 V^1_{{}^1\mathrm{S}_0} , \tag{4.15}$$

$$\langle {}^1\mathrm{P}_1 | V_{\rm ct}^{(2)} | {}^1\mathrm{P}_1 \rangle = \widetilde{C}_4 V^1_{{}^1\mathrm{P}_1} , \tag{4.16}$$

$$\langle {}^3\mathrm{P}_0 | V_{\rm ct}^{(2)} | {}^3\mathrm{P}_0 \rangle = \widetilde{C}_5 V^1_{{}^3\mathrm{P}_0} + \widetilde{C}_6 V^5_{{}^3\mathrm{P}_0} + \widetilde{C}_7 V^7_{{}^3\mathrm{P}_0} , \tag{4.17}$$

$$\langle {}^3\mathrm{P}_1 | V_{\rm ct}^{(2)} | {}^3\mathrm{P}_1 \rangle = \widetilde{C}_5 V^1_{{}^3\mathrm{P}_1} + \widetilde{C}_6 V^5_{{}^3\mathrm{P}_1} + \widetilde{C}_7 V^7_{{}^3\mathrm{P}_1} , \tag{4.18}$$

for the uncoupled channels, and

$$\langle {}^3\mathrm{SD}_1 | V_{\rm ct}^{(2)} | {}^3\mathrm{SD}_1 \rangle = \widetilde{C}_2 V^1_{{}^3\mathrm{SD}_1} + \widetilde{C}_3 V^5_{{}^3\mathrm{SD}_1} , \tag{4.19}$$

$$\langle {}^3\mathrm{PF}_2 | V_{\rm ct}^{(2)} | {}^3\mathrm{PF}_2 \rangle = \widetilde{C}_5 V^1_{{}^3\mathrm{PF}_2} + \widetilde{C}_6 V^5_{{}^3\mathrm{PF}_2} + \widetilde{C}_7 V^7_{{}^3\mathrm{PF}_2} , \tag{4.20}$$

for the coupled ones. It is clear that only certain combinations of the contact operators contribute to each partial wave, which allows for a simplified fitting procedure. Specifically, we determine $C_{^1S_0}$ and $\widetilde{C}_1$ by fitting the $^1S_0$ channel, $\widetilde{C}_4$ by means of the $^1P_1$ channel, $\widetilde{C}_5$, $\widetilde{C}_6$ and $\widetilde{C}_7$ from a simultaneous fit to the $^3P_0$, $^3P_1$ and $^3P_2$-$^3F_2$ channels, and finally $C_{^3S_1}$, $\widetilde{C}_2$ and $\widetilde{C}_3$ by fitting the $^3S_1$-$^3D_1$ channel.

We note that the fitted LECs $\widetilde{C}_i$ are given in terms of those of the NLO operators in Eq. (3.111) through (3.116) and (4.12) by the relation

$$\begin{bmatrix} \widetilde{C}_1 \\ \widetilde{C}_2 \\ \widetilde{C}_3 \\ \widetilde{C}_4 \\ \widetilde{C}_5 \\ \widetilde{C}_6 \\ \widetilde{C}_7 \end{bmatrix} = \begin{bmatrix} 1 & 1 & -3 & -3 & -1 & -1 & 0 \\ 1 & -3 & 1 & -3 & 0 & 0 & 0 \\ 0 & 0 & 0 & 0 & 1 & -3 & 0 \\ 1 & -3 & -3 & 9 & -1 & 3 & 0 \\ 1 & 1 & 1 & 1 & 0 & 0 & 0 \\ 0 & 0 & 0 & 0 & 1 & 1 & 0 \\ 0 & 0 & 0 & 0 & 0 & 0 & 1 \end{bmatrix} \begin{bmatrix} C_{q^2} \\ C_{I^2,q^2} \\ C_{S^2,q^2} \\ C_{S^2,I^2,q^2} \\ C_{(q\cdot S)^2} \\ C_{I^2,(q\cdot S)^2} \\ C^{I=1}_{(q\times S)\cdot k} \end{bmatrix}, \tag{4.21}$$

which can be inverted in order to find the original LECs C_i, once the $\widetilde{C}_i$ have been determined.

4.2 Interactions on the Lattice: Improvement of Pion Exchange Potential

The TPE contributes at NLO and N^{2}LO. At LO, the OPE potential is given by Ref. [13, 28]

$$V^{(0)}_{1\pi}(M_\pi) \;=\; \frac{1}{2} : \sum_{S_1,S_2,I} \sum_{\mathbf{n}_1,\mathbf{n}_2} \left(-\frac{g_A^2}{4f_\pi^2}\right) G_{S_1,S_2}(\mathbf{n}_1-\mathbf{n}_2, M_\pi)\, \rho_{S_1,I}(\mathbf{n}_1)\rho_{S_2,I}(\mathbf{n}_2) : , \tag{4.22}$$

where the pion propagator is

$$G_{S_1,S_2}(\mathbf{n}_1-\mathbf{n}_2, M_\pi) \equiv \frac{1}{L^3}\sum_{\mathbf{k}} \exp\left[i\frac{2\pi}{L}\mathbf{k}\cdot(\mathbf{n}_1-\mathbf{n}_2)\right] \times G_{S_1,S_2}(\mathbf{k}, M_\pi)\,, \tag{4.23}$$

with

$$G_{S_1,S_2}(\mathbf{k}, M_\pi) \equiv \frac{q_{S_1} q_{S_2}}{M_\pi^2 + q^2}\,, \tag{4.24}$$

we take

$$q^2 \equiv 2\sum_{l=1}^{3}\left[\omega_0 - \omega_1 \cos\left(\frac{2\pi}{L}k_l\right) + \omega_2 \cos\left(\frac{4\pi}{L}k_l\right) - \omega_3 \cos\left(\frac{6\pi}{L}k_l\right)\right], \tag{4.25}$$

using the $O(a^4)$-improved hopping coefficients ω_i of Table 3.1. For the numerator of Eq. (4.24), we take

$$q_i \equiv \sin\left(\frac{2\pi}{L}k_i\right), \tag{4.26}$$

which coincides with the choice of derivative operator in Eq. (4.13). We also include the isospin-breaking (IB) effects due to the pion mass differences, Eq. (3.91). Specifically, we take

$$V_{1\pi}^{(0)}(I=1) = 2V_{1\pi}^{(0)}(M_{\pi^\pm}) - V_{1\pi}^{(0)}(M_{\pi^0}), \tag{4.27}$$

$$V_{1\pi}^{(0)}(I=0) = -2V_{1\pi}^{(0)}(M_{\pi^\pm}) - V_{1\pi}^{(0)}(M_{\pi^0}), \tag{4.28}$$

for the isospin-triplet and isospin-singlet channels, respectively. This approach is consistent with the conventions of the Nijmegen partial wave analysis (PWA). For more details on the IB corrections to the NN interaction, see Ref. [7, 31] (and references therein).

The first contribution from the TPE potential appears at NLO in χEFT. We note that several prior continuum calculations including TPE exist. For instance, in Ref. [32, 33], dimensional regularization (DR) was used to remove the divergence appearing in the loop integral, and a non-local momentum-dependent form factor was applied to suppress the high-momentum contributions when solving the Lippmann-Schwinger equation. In Ref. [34], another regularization called spectral function regularization (SFR) was proposed. Compared to DR, the SFR method introduces an additional cutoff to remove the short-range components of the TPE potential. Recently, a new position-space regularization was proposed in Ref. [35–37]. The study of effects in nuclear lattice EFT due to different choices of regularization of the TPE is beyond the scope of the current work. In this work, we use the DR expressions with discretized lattice momenta. We also note that the lattice spacing serves as a natural ultraviolet (UV) cut-off.

Thus far, nuclear lattice EFT calculations have been performed with a lattice spacing of $a = 1.97$ fm, and hence the TPE potentials at NLO and N^{2}LO have not been included explicitly, but rather been absorbed into the CTs. Since we are here studying the effects of reducing the lattice spacing to $a \simeq 1$ fm, we shall for the first time include the full TPE structure. As for the smeared LO CTs and the OPE potential, we define the lattice formulation of the TPE potential in momentum space, and Fourier transform the results to coordinate space. The TPE potential is of the form

$$V_{2\pi}^{(2)} = \frac{1}{2} : \sum_{\mathbf{n}_1,\mathbf{n}_2} \sum_{S_1,S_2} T_{S_1,S_2}^{(2)}(\mathbf{n}_1-\mathbf{n}_2)\rho_{S_1}(\mathbf{n}_1)\rho_{S_2}(\mathbf{n}_2) : + \frac{1}{2} : \sum_{\mathbf{n}_1,\mathbf{n}_2} \sum_{I} W_{\mathrm{C}}^{(2)}(\mathbf{n}_1-\mathbf{n}_2)\rho_I(\mathbf{n}_1)\rho_I(\mathbf{n}_2) :$$
$$+ \frac{1}{2} : \sum_{\mathbf{n}_1,\mathbf{n}_2} \sum_{S} V_{\mathrm{S}}^{(2)}(\mathbf{n}_1-\mathbf{n}_2)\rho_S(\mathbf{n}_1)\rho_S(\mathbf{n}_2) : , \tag{4.29}$$

at NLO. The explicit expressions for the components of Eq. (4.29) are

$$T_{S_1,S_2}^{(2)}(\mathbf{n}_1-\mathbf{n}_2) \equiv \frac{1}{L^3}\sum_{\mathbf{k}} \exp\left[i\frac{2\pi}{L}\mathbf{k}\cdot(\mathbf{n}_1-\mathbf{n}_2)\right] \times T_{S_1,S_2}^{(2)}(\mathbf{k}) , \tag{4.30}$$

where

$$T_{S_1,S_2}^{(2)}(\mathbf{k}) \equiv 18 g_{\mathrm{A}}^4 F^{(2)}(q)\, q_{S_1} q_{S_2} , \tag{4.31}$$

and

$$W_{\mathrm{C}}^{(2)}(\mathbf{n}_1-\mathbf{n}_2) \equiv \frac{1}{L^3}\sum_{\mathbf{k}} \exp\left[i\frac{2\pi}{L}\mathbf{k}\cdot(\mathbf{n}_1-\mathbf{n}_2)\right] \times W_{\mathrm{C}}^{(2)}(\mathbf{k}) , \tag{4.32}$$

with

$$W_{\mathrm{C}}^{(2)}(\mathbf{k}) \equiv F^{(2)}(q)\left[\frac{48 g_{\mathrm{A}}^2 M_\pi^4}{4M_\pi^2+q^2} + 4M_\pi^2\left(5g_{\mathrm{A}}^4 - 4g_{\mathrm{A}}^2 - 1\right) + q^2\left(23 g_{\mathrm{A}}^4 - 10 g_{\mathrm{A}}^2 - 1\right)\right], \tag{4.33}$$

and

$$V_{\mathrm{S}}^{(2)}(\mathbf{n}_1-\mathbf{n}_2) \equiv \frac{1}{L^3}\sum_{\mathbf{k}} \exp\left[i\frac{2\pi}{L}\mathbf{k}\cdot(\mathbf{n}_1-\mathbf{n}_2)\right] \times V_{\mathrm{S}}^{(2)}(\mathbf{k}) , \tag{4.34}$$

with

$$V_{\mathrm{S}}^{(2)}(\mathbf{k}) \equiv -18 g_{\mathrm{A}}^4 F^{(2)}(q)\, q^2 , \tag{4.35}$$

where the function $F^{(2)}(q)$ is given by

$$F^{(2)}(q) \equiv -\frac{1}{384\pi^2 f_\pi^4} L(q) , \tag{4.36}$$

and $L(q)$ is the loop function

$$L(q) \equiv \frac{\sqrt{4M_\pi^2+q^2}}{2q} \log\left(\frac{\sqrt{4M_\pi^2+q^2}+q}{\sqrt{4M_\pi^2+q^2}-q}\right) , \tag{4.37}$$

in DR. In order to coincide with the definitions of the derivative operator Eq. (4.13) and the double-derivative operator Eq. (4.14), we take

$$q_i \to \sin\left(\frac{2\pi}{L}k_i\right) \ , \tag{4.38}$$

$$q_i^2 \to \left[\sin\left(\frac{2\pi}{L}k_i\right)\right]^2 \ , \tag{4.39}$$

which ensures that the divergences appearing in the loop diagrams can be absorbed by tuning the contact interaction LECs C_i.

Similarly, we parameterize the sub-leading (N^2LO) contribution to the TPE as

$$\begin{aligned} V_{2\pi}^{(3)} &= \frac{1}{2} : \sum_{\mathbf{n}_1,\mathbf{n}_2} \sum_{S_1,S_2,I} T_{S_1,S_2}^{(3)}(\mathbf{n}_1-\mathbf{n}_2)\rho_{S_1,I}(\mathbf{n}_1)\rho_{S_2,I}(\mathbf{n}_2) : \\ &+ \frac{1}{2} : \sum_{\mathbf{n}_1,\mathbf{n}_2} \sum_{S,I} W_{\mathrm{S}}^{(3)}(\mathbf{n}_1-\mathbf{n}_2)\rho_{S,I}(\mathbf{n}_1)\rho_{S,I}(\mathbf{n}_2) : \\ &+ \frac{1}{2} : \sum_{\mathbf{n}_1,\mathbf{n}_2} V_{\mathrm{C}}^{(3)}(\mathbf{n}_1-\mathbf{n}_2)\rho(\mathbf{n}_1)\rho(\mathbf{n}_2) : , \end{aligned} \tag{4.40}$$

where

$$T_{S_1,S_2}^{(3)}(\mathbf{n}_1-\mathbf{n}_2) \equiv \frac{1}{L^3}\sum_{\mathbf{k}} \exp\left[i\frac{2\pi}{L}\mathbf{k}\cdot(\mathbf{n}_1-\mathbf{n}_2)\right] \times T_{S_1,S_2}^{(3)}(\mathbf{k}) \ , \tag{4.41}$$

with

$$T_{S_1,S_2}^{(3)}(\mathbf{k}) \equiv c_4 F^{(3)}(q)\,(4M_\pi^2+q^2)\,q_{S_1}q_{S_2} \ , \tag{4.42}$$

and

$$W_{\mathrm{S}}^{(3)}(\mathbf{n}_1-\mathbf{n}_2) \equiv \frac{1}{L^3}\sum_{\mathbf{k}} \exp\left[i\frac{2\pi}{L}\mathbf{k}\cdot(\mathbf{n}_1-\mathbf{n}_2)\right] \times W_{\mathrm{S}}^{(3)}(\mathbf{k}) \ , \tag{4.43}$$

with

$$W_{\mathrm{S}}^{(3)}(\mathbf{k}) \equiv -c_4 F^{(3)}(q)\,q^2 \ , \tag{4.44}$$

and

$$V_{\mathrm{C}}^{(3)}(\mathbf{n}_1-\mathbf{n}_2) \equiv \frac{1}{L^3}\sum_{\mathbf{k}} \exp\left[i\frac{2\pi}{L}\mathbf{k}\cdot(\mathbf{n}_1-\mathbf{n}_2)\right] \times V_{\mathrm{C}}^{(3)}(\mathbf{k}) \ , \tag{4.45}$$

with

$$V_{\mathrm{C}}^{(3)}(\mathbf{k}) \equiv 6F^{(3)}(q)\,(2M_\pi^2+q^2)\left[2M_\pi^2(2c_1-c_3)-c_3q^2\right] \ , \tag{4.46}$$

Table 4.1: Summary of lattice spacings a (spatial) and a_t (temporal) and box dimensions L. The physical spatial lattice volume V is kept constant at $(La)^3 \simeq (63\text{ fm})^3$.

a^{-1} [MeV]	a_t^{-1} [MeV]	a [fm]	L	La [fm]
100	150	1.97	32	63.14
120	216	1.64	38	62.48
150	337.5	1.32	48	63.14
200	600	0.98	64	63.14

where the function $F^{(3)}(q)$ is given by

$$F^{(3)}(q) \equiv -\frac{g_A^2}{32\pi f_\pi^4} A(q)\,, \tag{4.47}$$

and $A(q)$ is the loop function

$$A(q) \equiv \frac{1}{2q} \arctan\left(\frac{q}{2M_\pi}\right)\,, \tag{4.48}$$

in DR. For the momenta $\mathbf{q}$, we again apply the conventions of Eq. (4.26) and (4.39).

4.3 Phase Shifts and Mixing Angles to N^{2}LO

We now turn to a description of our calculational methods. We take $f_\pi = 92.2$ MeV for the pion decay constant, and $g_A = 1.29$ for the nucleon axial coupling constant to account for the Goldberger-Treiman relation (GTR) Ref. [31]. For the nucleon mass, we use $m_N = 938.38$ MeV, and for the charged and neutral pion masses, we take $M_{\pi^\pm} = 139.57$ MeV and $M_{\pi^0} = 134.98$ MeV, respectively. We use the isospin-averaged pion mass

$$M_\pi \equiv \frac{2}{3} M_{\pi^\pm} + \frac{1}{3} M_{\pi^0} = 138.03\text{ MeV}\,, \tag{4.49}$$

in the TPE potential expressions at NLO and N^{2}LO. For the constants c_1, c_3 and c_4 that appear in the TPE potential at N^{2}LO, we use $c_1 = -1.10(3)\text{ GeV}^{-1}$, $c_3 = -5.54(6)\text{ GeV}^{-1}$ and $c_4 = 4.17(4)\text{ GeV}^{-1}$ from the accurate Roy-Steiner analysis of pion-nucleon scattering adopted to the counting of the nucleon mass used here Ref. [6]. Also, as the uncertainties of these LECs are very small, we only consider the central values in the following.

We determine the optimal parameter values for the NLEFT action up to N^{2}LO by performing a chi-square fit to np phase shifts and mixing angles. For this purpose, we define the uncertainties of the

Table 4.2: Summary of the fitting procedure, indicating which parameters are fitted to what scattering channel at each order in NLEFT, and the resulting χ^2/N_{dof} (for $a = 0.98$ fm).

order	fit channels	fit parameters	χ^2/N_{dof}
LO	$^1S_0$, $^3S_1$	$C_{^1S_0}$, $C_{^3S_1}$, b_s	30.38
NLO	$^1S_0$	$C_{^1S_0}$, $\widetilde{C}_1$	1.77
	$^3S_1$, ϵ_1	$C_{^3S_1}$, $\widetilde{C}_2$, $\widetilde{C}_3$	88.81
	$^1P_1$	$\widetilde{C}_4$	11.94
	$^3P_0$, $^3P_1$, $^3P_2$	$\widetilde{C}_5$, $\widetilde{C}_6$, $\widetilde{C}_7$	6.51
N^{2}LO	$^1S_0$	$C_{^1S_0}$, $\widetilde{C}_1$	0.36
	$^3S_1$, ϵ_1	$C_{^3S_1}$, $\widetilde{C}_2$, $\widetilde{C}_3$	28.81
	$^1P_1$	$\widetilde{C}_4$	2.79
	$^3P_0$, $^3P_1$, $^3P_2$	$\widetilde{C}_5$, $\widetilde{C}_6$, $\widetilde{C}_7$	25.59

empirical scattering observables (in each partial wave) according to Ref. [37, 39], which gives

$$\Delta_i \equiv \max\left[\Delta_i^{\text{PWA}}, \left|\delta_i^{\text{NijmI}} - \delta_i^{\text{PWA}}\right|, \left|\delta_i^{\text{NijmII}} - \delta_i^{\text{PWA}}\right|, \left|\delta_i^{\text{Reid93}} - \delta_i^{\text{PWA}}\right|\right], \tag{4.50}$$

where Δ_i^{PWA} denotes the uncertainty of the PWA, while δ_i^{PWA} signifies the phase shift (or mixing angle) in channel i of the PWA (see also Ref. [40]). Furthermore, δ_i^{NijmI}, δ_i^{NijmII} and δ_i^{Reid93} refer to the PWA results based on the Nijmegen I, Nijmegen II and Reid93 NN potentials, respectively. Hence, a measure of systematical error in the PWA is accounted for in our analysis. The χ^2 function to be minimized is defined as

$$\chi^2 \equiv \sum_i \frac{\left(\delta_i^{\text{PWA}} - \delta_i^{\text{cal}}\right)^2}{\Delta_i^2}, \tag{4.51}$$

where i runs over all values of p_{CM} and channels included in the analysis. In Eq. (4.51), δ_i^{PWA} is the phase shift (or mixing angle) at a given momentum p_{CM} from the PWA, δ_i^{cal} is the corresponding calculated NLEFT value, and Δ_i is given by Eq. (4.50).

When fitting the phase shifts and mixing angles of the Nijmegen PWA, we note certain simplifying features. Specifically, at LO we determine $C_{^1S_0}$, $C_{^3S_1}$, and the smearing parameter b_s, by fitting the $^1S_0$ and $^3S_1$ phase shifts. At NLO and N^{2}LO, we no longer update the value of b_s. At NLO, we determine $C_{^1S_0}$ and $\widetilde{C}_1$ by fitting the $^1S_0$ phase shift, $C_{^3S_1}$, $\widetilde{C}_2$ and $\widetilde{C}_3$ by fitting the $^3S_1$ phase shift and the mixing

Table 4.3: Fitted constants and low-energy parameters for $a = 0.98$ fm. The LO constants $C_{^1S_0}$ and $C_{^3S_1}$ are given in units of $[10^{-4}\ \mathrm{MeV}^{-2}]$, and the C_i of the NLO interaction in units of $[10^{-8}\ \mathrm{MeV}^{-4}]$. Due to the large lattice ($L = 64$) for $a = 0.98$ fm, an uncertainty analysis using the variance-covariance matrix as in Table 4.4 was numerically unfeasible. Hence, an estimated uncertainty of 2% has been assigned, which is consistent with the uncertainties for larger a. For entries with a dagger (†), the deuteron energy E_d has been included as an additional constraint.

	LO	NLO	N^{2}LO
$C_{^1S_0}$	−0.101(2)	−0.105(2)	−0.106(2)
$C_{^3S_1}$	−0.118(2)	−0.087(2)	−0.088(2)
b_s	0.399(8)	–	–
C_{q^2}	–	0.00440(8)	0.135(2)
$C_{\mathrm{I}^2,\mathrm{q}^2}$	–	0.0373(8)	0.0303(6)
$C_{\mathrm{S}^2,\mathrm{q}^2}$	–	−0.0292(6)	−0.0301(6)
$C_{\mathrm{S}^2,\mathrm{I}^2,\mathrm{q}^2}$	–	−0.00190(4)	−0.0254(5)
$C_{(\mathrm{q}\cdot\mathrm{S})^2}$	–	0.0378(8)	0.0360(7)
$C_{\mathrm{I}^2,(\mathrm{q}\cdot\mathrm{S})^2}$	–	0.00200(4)	0.0212(4)
$C^{I=1}_{(\mathrm{q}\times\mathrm{S})\cdot\mathrm{k}}$	–	0.0150(3)	0.0165(3)
E_d [MeV]	2.16(4)	2.22(4)†	2.22(4)†
$r_{^1S_0}$ [fm]	2.12(4)	2.50(5)	2.63(5)
$a_{^1S_0}$ [fm]	−22.5(4)	−23.4(5)	−23.7(5)
$r_{^3S_1}$ [fm]	1.73(3)	1.70(3)	1.74(3)
$a_{^3S_1}$ [fm]	5.4(1)	5.4(1)	5.4(1)

angle ϵ_1, $\widetilde{C}_4$ by fitting the $^1P_1$ phase shift, and finally $\widetilde{C}_5$, $\widetilde{C}_6$ and $\widetilde{C}_7$ by fitting the the $^3P_0$, $^3P_1$ and $^3P_2$ phase shifts. The N^{2}LO fits are similar, apart from the inclusion of the N^{2}LO TPE potential operators. We do not take the deuteron binding energy E_d as an additional constraint in the LO fits, as we do not expect E_d to be accurately reproduced in an LO calculation. At NLO and N^{2}LO, the experimental value $E_\mathrm{d} = 2.224575(9)$ MeV is taken as an additional constraint. At LO, we fit up to center-of-mass momenta of $p_\mathrm{CM}^\mathrm{max} = 100$ MeV, while at NLO and N^{2}LO we fit up to $p_\mathrm{CM}^\mathrm{max} = 150$ MeV. Our fitting procedure at each order in NLEFT is summarized in Table 4.2.

Prior NLEFT work has used a relatively coarse lattice spacing of $a = 1.97$ fm, which corresponds to a momentum cutoff $\Lambda \sim \pi/a = 314$ MeV. This relatively low cutoff may induce significant lattice artifacts, particularly at high momenta. With this in mind, we here aim to study the NN scattering problem for $a = (200\ \mathrm{MeV})^{-1} = 0.98$ fm, with a temporal lattice spacing of $a_\mathrm{t} = (600\ \mathrm{MeV})^{-1}$. The number of lattice points in each spatial dimension is $L = 64$, thus the physical volume is $V = (La)^3 \simeq (63\ \mathrm{fm})^3$, which is expected to be large enough to accommodate the NN system without introducing significant finite volume

Table 4.4: Fitted constants and low-energy S-wave parameters for $a = 0.98$ fm. The LO constants $C_{^1S_0}$ and $C_{^3S_1}$ are given in units of $[10^{-4}\ \mathrm{MeV}^{-2}]$, and the C_i of the NLO interaction in units of $[10^{-8}\ \mathrm{MeV}^{-4}]$. The smearing parameter b_s of the LO contact interactions is determined by the LO fit, and thereafter kept fixed at NLO and N^{2}LO. The values in parentheses are the uncertainties calculated using the variance-covariance matrix according to Eq. (A.5).

order	fit parameters	$a = 1.97$ fm	$a = 1.64$ fm	$a = 1.32$ fm
LO	$C_{^1S_0}$	−0.4676(2)	−0.3290(7)	−0.201(5)
	$C_{^3S_1}$	−0.6377(2)	−0.4482(2)	−0.265(5)
	b_s	0.0524(2)	0.0917(2)	0.173(6)
NLO	$C_{^1S_0}$	−0.5(1)	−0.35(2)	−0.220(2)
	$C_{^3S_1}$	−0.44(7)	−0.21(1)	−0.152(4)
	C_{q^2}	−0.05(3)	−0.032(9)	−0.006(1)
	C_{I^2,q^2}	0.08(2)	0.075(2)	0.052(1)
	C_{S^2,q^2}	−0.06(3)	−0.046(3)	−0.0341(7)
	C_{S^2,I^2,q^2}	0.03(2)	0.029(2)	0.0081(2)
	$C_{(q\cdot S)^2}$	0.11(2)	0.091(4)	0.0553(2)
	$C_{I^2,(q\cdot S)^2}$	−0.11(2)	−0.074(4)	−0.0240(8)
	$C^{I=1}_{(q\times S)\cdot k}$	0.037(8)	0.026(4)	0.019(2)
N^{2}LO	$C_{^1S_0}$	−0.5(1)	−0.33(4)	−0.21(2)
	$C_{^3S_1}$	−0.5(1)	−0.22(1)	−0.15(2)
	C_{q^2}	0.08(3)	0.093(7)	0.118(7)
	C_{I^2,q^2}	0.07(2)	0.0668(4)	0.045(4)
	C_{S^2,q^2}	−0.06(3)	−0.05(2)	−0.036(7)
	C_{S^2,I^2,q^2}	0.01(2)	0.005(3)	−0.014(4)
	$C_{(q\cdot S)^2}$	0.10(3)	0.086(7)	0.056(4)
	$C_{I^2,(q\cdot S)^2}$	−0.10(3)	−0.055(4)	−0.006(4)
	$C^{I=1}_{(q\times S)\cdot k}$	0.031(8)	0.025(4)	0.018(2)

effects for the energy region $p_{\mathrm{CM}} < 200$ MeV studied here. Our lattice parameters are summarized in Table 4.1.

First, we consider the problem of np scattering by treating all orders in NLEFT up to N^{2}LO non-perturbatively, similar to what is done in the continuum. This means that we construct the transfer matrix according to

$$M \equiv :\exp\left[-\alpha_t(H_{\mathrm{free}} + V_{\mathrm{LO}} + V_{\mathrm{NLO}} + V_{\mathrm{N^2LO}})\right]:, \tag{4.52}$$

Table 4.5: Low-energy S-wave parameters, as a function of the lattice spacing a and the order of the NLEFT expansion. E_d is the deuteron binding energy, and the a_i and r_i denote the scattering lengths and effective ranges in channel i. The experimental value of E_d is from Ref. [38], and the scattering lengths and effective ranges are from Ref. [2]. For entries marked with a dagger (†), the empirical deuteron energy E_d has been included in the fit as an additional constraint.

order	a [fm]	E_d [MeV]	$r_{^1\mathrm{S}_0}$ [fm]	$a_{^1\mathrm{S}_0}$ [fm]	$r_{^3\mathrm{S}_1}$ [fm]	$a_{^3\mathrm{S}_1}$ [fm]
LO	1.97	2.00(1)	2.041(1)	−22.4(4)	1.686(1)	5.46(1)
	1.64	2.07(1)	2.093(5)	−22.5(7)	1.6932(8)	5.45(1)
	1.32	2.12(2)	2.11(2)	−22.5(5)	1.71(1)	5.44(1)
NLO	1.97	2.2246(3)†	2.4(6)	−23(4)	1.79(3)	5.31(2)
	1.64	2.2246(1)†	2.3(1)	−23(2)	1.73(1)	5.33(1)
	1.32	2.2246(1)†	2.47(3)	−23(1)	1.70(1)	5.336(9)
N^{2}LO	1.97	2.2246(3)†	2.6(6)	−24(4)	1.82(3)	5.35(2)
	1.64	2.2246(1)†	2.5(3)	−23(2)	1.74(1)	5.36(1)
	1.32	2.22457(7)†	2.6(2)	−23(1)	1.744(7)	5.382(5)
experiment	–	2.224575(9)	2.77(5)	−23.740(20)	1.753(8)	5.419(7)

where the potential terms are given by

$$V_\mathrm{LO} = C_{^1\mathrm{S}_0} O^{(0)}_{(0,1)} + C_{^3\mathrm{S}_1} O^{(0)}_{(1,0)} + V^{(0)}_\mathrm{OPE} \,, \tag{4.53}$$

at LO,

$$\begin{aligned} V_\mathrm{NLO} \;=\; & C_{\mathrm{q}^2} O^{(2)}_1 + C_{\mathrm{I}^2,\mathrm{q}^2} O^{(2)}_2 + C_{\mathrm{S}^2,\mathrm{q}^2} O^{(2)}_3 + C_{\mathrm{S}^2,\mathrm{I}^2,\mathrm{q}^2} O^{(2)}_4 + C_{(\mathrm{q}\cdot\mathrm{S})^2} O^{(2)}_5 \\ & + C_{\mathrm{I}^2,(\mathrm{q}\cdot\mathrm{S})^2} O^{(2)}_6 + C^{I=1}_{(\mathrm{q}\times\mathrm{S})\cdot\mathrm{k}} O^{(2)}_7 + V^{(2)}_\mathrm{TPE} \,, \end{aligned} \tag{4.54}$$

at NLO, and

$$V_{\mathrm{N^2LO}} = V^{(3)}_\mathrm{TPE} \,, \tag{4.55}$$

at N^{2}LO. Our results for the smallest lattice spacing, $a = 0.98$ fm, are shown in Fig. 4.1. Clearly, the description of the S-wave channels is quite good even at LO, particularly for $^3\mathrm{S}_1$. Compared to LO, significant improvements occur at NLO and N^{2}LO, in particular for the $^1\mathrm{P}_1$, $^3\mathrm{P}_0$ and $^3\mathrm{P}_2$ channels, as well as for the mixing angle ϵ_1. While the NLO contributions appear central for a good description of the P-waves and ϵ_1, the TPE contributions at N^{2}LO do not appear to produce a significant systematical effect, although we note that certain channels (such as $^3\mathrm{P}_2$) show marked improvement at N^{2}LO. While

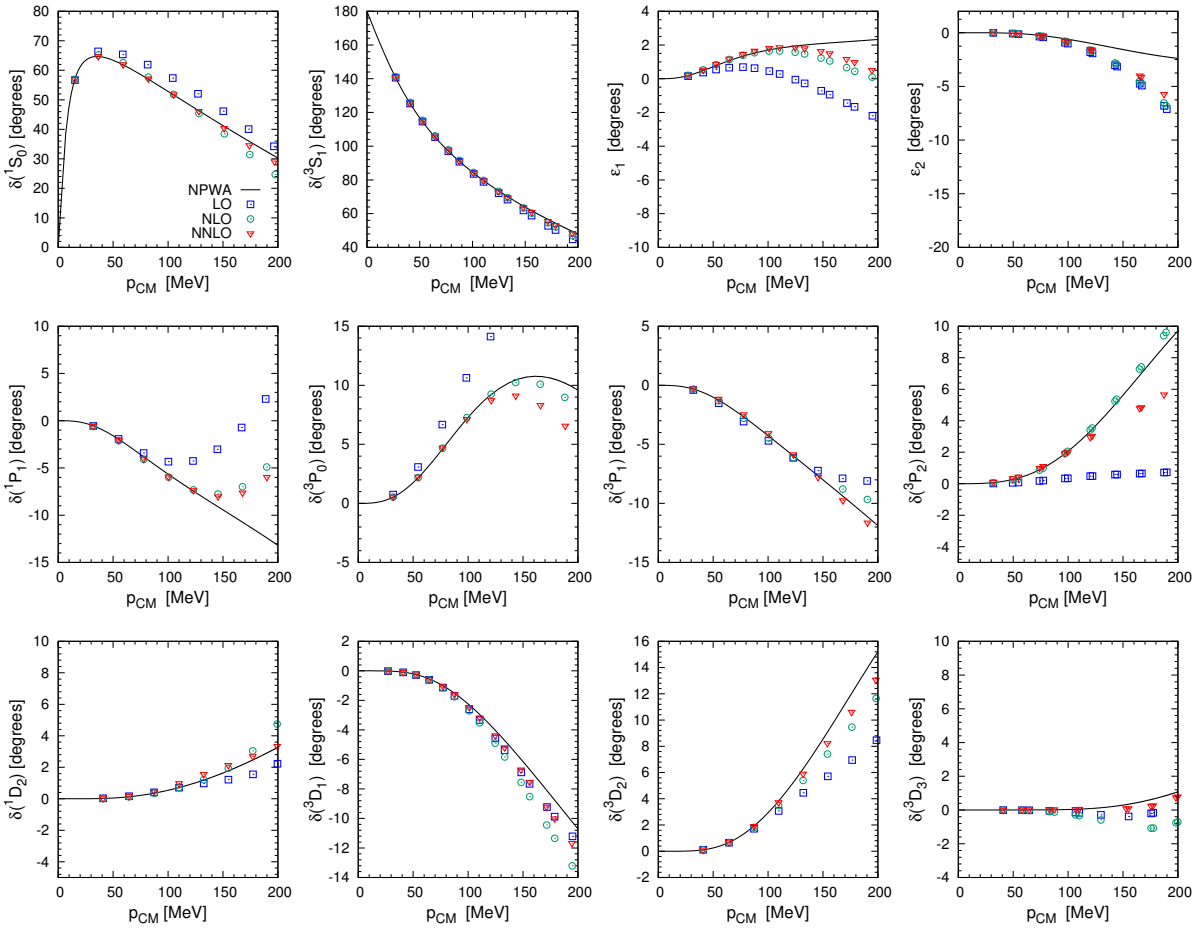

Figure 4.1: Phase shifts and mixing angles for np scattering up to N^{2}LO in NLEFT, for our smallest (spatial) lattice spacing of $a = 0.98$ fm $= (200\ \text{MeV})^{-1}$ and a temporal lattice spacing $a_t = (600\ \text{MeV})^{-1}$. The (blue) squares, (green) circles and (red) triangles denote LO, NLO and N^{2}LO results, respectively. The NPWA is shown by the solid black line.

the results for the D-waves appear rather accurate, we note that the current way of smearing the LO contact interactions does produce unwanted additional forces in the D-wave channels, which should be dominated by OPE alone.

In Table 4.2, we also give the value of χ^2/N_{dof} for each of our fits ($a = 0.98$ fm), where N_{dof} equals to the number of fitted data points (phase shifts or mixing angles at a given momentum) minus the number of adjustable parameters. At LO with $a = 0.98$ fm, we find $\chi^2/N_{\text{dof}} \simeq 30$, which is reasonable given the rather stringent uncertainty criterion (4.50) of the PWA. This indicates that we have a satisfactory description of the $^1S_0$ and $^3S_1$ channels in the range $p_{\text{CM}} < 100$ MeV. At NLO, the main contribution to χ^2/N_{dof} arises from ϵ_1 with $p_{\text{CM}} > 100$ MeV, while at N^{2}LO ϵ_1 and the P-wave channels contribute

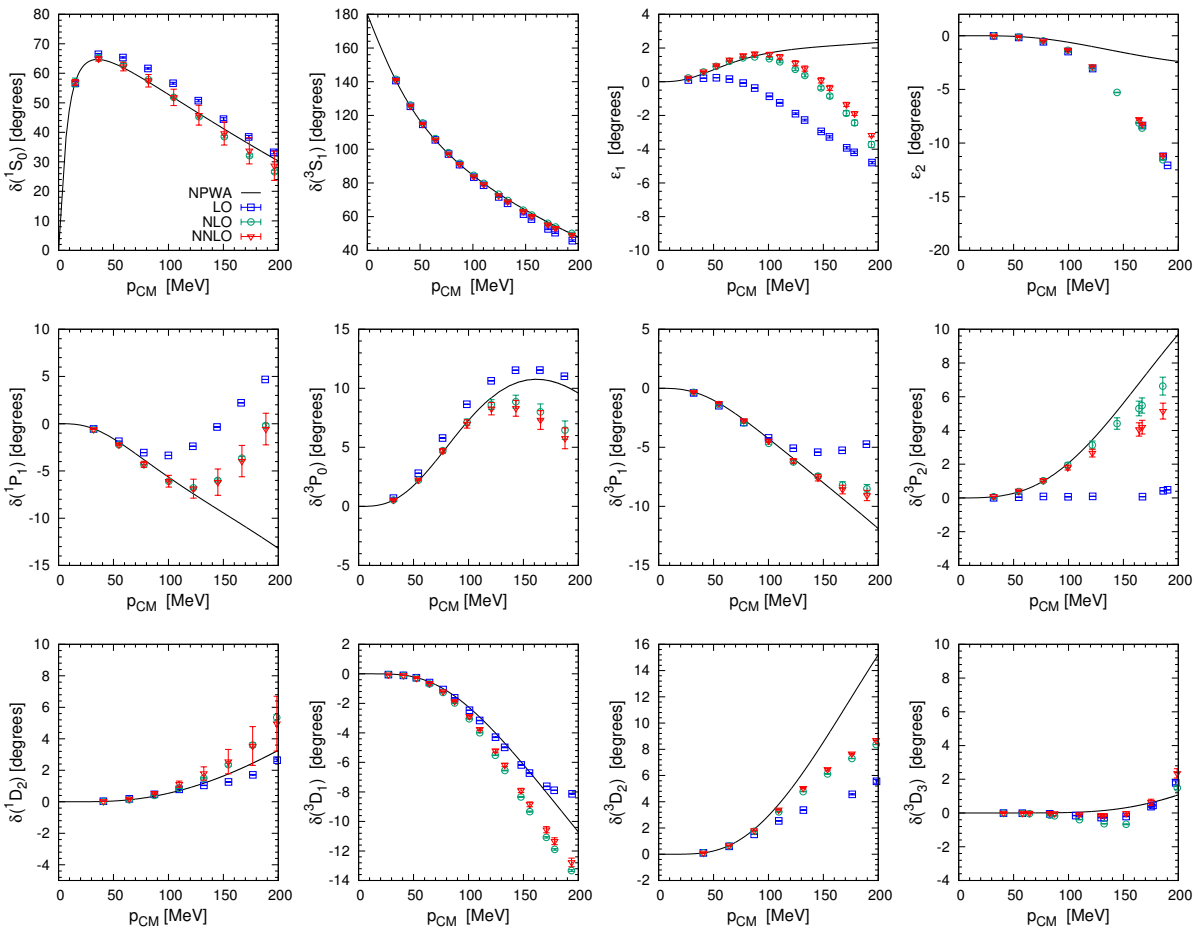

Figure 4.2: Phase shifts and mixing angles for np scattering up to N^{2}LO in NLEFT, for $a = 1.32$ fm = $(150\ \text{MeV})^{-1}$. For notations, see Fig. 4.1.

roughly equally. These observations are consistent with the results shown in Fig. 4.1.

We also give the S-wave low-energy parameters for $a = 0.98$ fm in Table 4.3, along with a summary of the fitted parameters. We find that the NLO and N^{2}LO results clearly provide the closest agreement with the empirical scattering lengths and effective ranges, taken from Ref. [2]. We note that $a_{^3\text{S}_1}$ and $r_{^3\text{S}_1}$ are both stable at various orders in NLEFT, and reasonably close to the empirical values. This is easily understood since the phase shift in the $^3\text{S}_1$ channel is accurately reproduced already at LO. For $a_{^1\text{S}_0}$ and $r_{^1\text{S}_0}$, a clear improvement is observed at NLO and N^{2}LO compared to the results at LO. We also find that at NLO and N^{2}LO, E_d can be accommodated without sacrificing any accuracy in the other low-energy parameters. Finally, $C_{^1\text{S}_0}$ and $C_{^3\text{S}_1}$ for $a = 0.98$ fm are in reasonably close agreement with the continuum results of Ref. [37] for a cutoff of $R = 1.0$ fm, which suggests that lattice artifacts are under control.

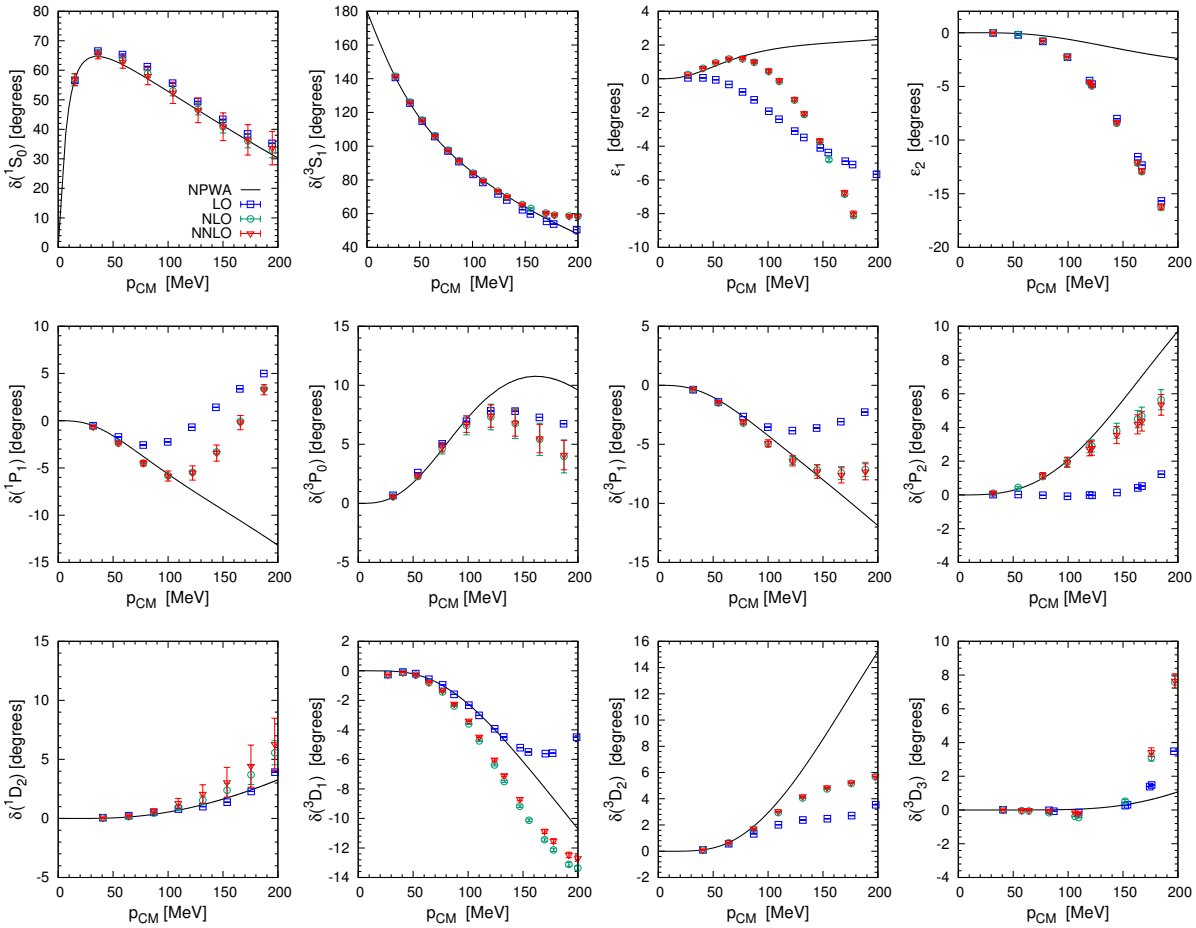

Figure 4.3: Phase shifts and mixing angles for np scattering up to N^{2}LO in NLEFT, for $a = 1.64$ fm $= (120\ \text{MeV})^{-1}$. For notations, see Fig. 4.1.

4.4 Variation of the Lattice Spacing

Up to this point, we have mostly elaborated on our results for $a = 0.98$ fm, which is the smallest lattice spacing we have considered. We shall next comment on our findings when the lattice spacing is varied in the range $1.97 \geq a \geq 0.98$ fm, while the physical lattice volume is kept constant at $V = (La)^3 \simeq (63\ \text{fm})^3$ (see Table 4.1 for a summary of lattice parameters). As we work within the transfer matrix formalism, the temporal lattice spacing a_t should also be varied when a is changed. Here, we choose a_t such that a_t/a^2 is kept constant. This is motivated by the fact that the Hamiltonian scales with the lattice spacing as $H \sim 1/a^2$. For a pioneering LO calculation of the effects of varying a, see also Ref. [27].

In Table 4.4, we summarize the fitted constants of the NN interaction as a function of a, along with the S-wave low-energy parameters in Table 4.5. We note that the uncertainties of the fitted constants

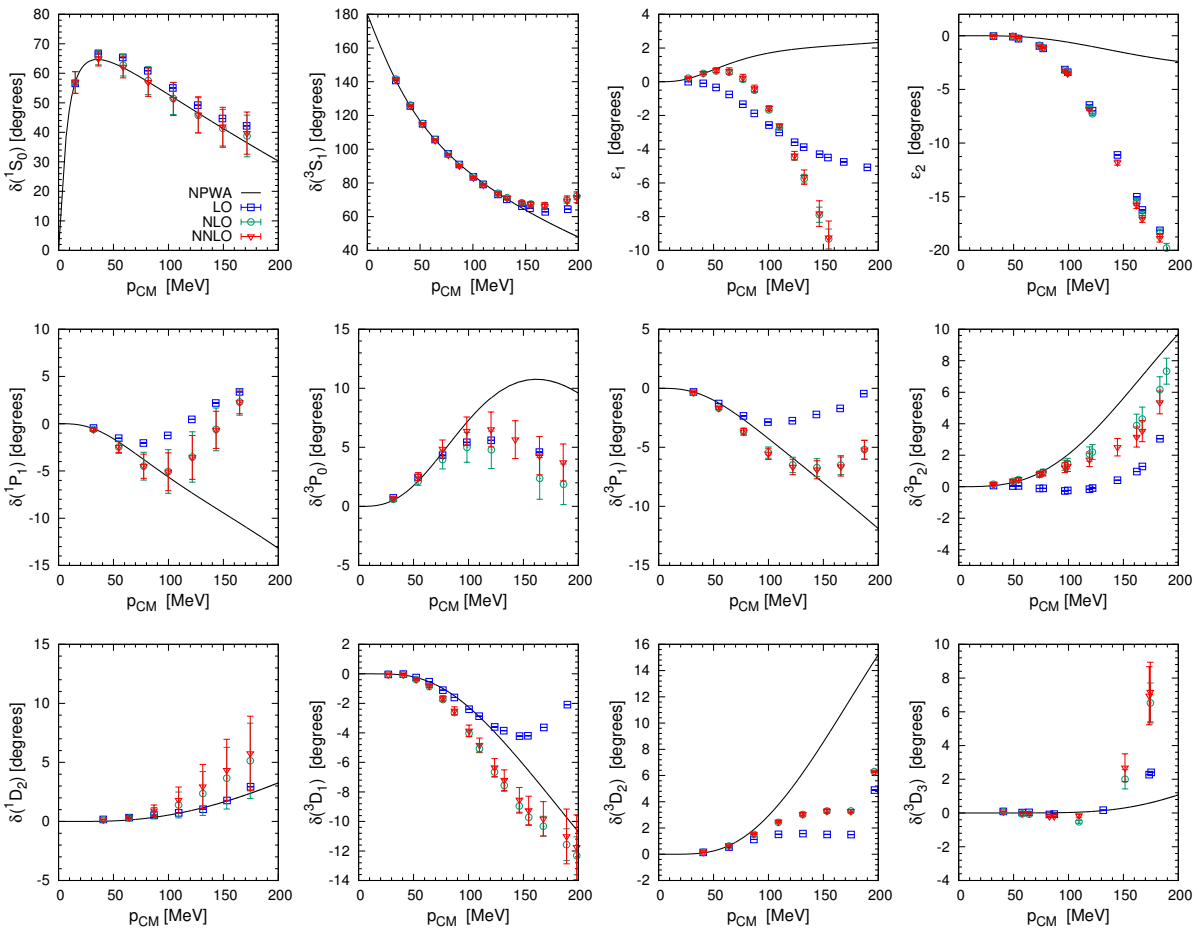

Figure 4.4: Phase shifts and mixing angles for np scattering up to N^2LO in NLEFT, for a (spatial) lattice spacing $a = 1.97$ fm $= (100\ \text{MeV})^{-1}$ and a temporal lattice spacing $a_t = (150\ \text{MeV})^{-1}$. For notations, see Fig. 4.1.

are obtained by an analysis of the variance-covariance matrix according to Eq. (A.5), while those of the S-wave parameters are obtained using Eq. (A.8). Our computed S-wave parameters appear very stable with respect to lattice spacing variation, which suggests that lattice spacing effects are small in the S-wave channels.

Our results for np phase shifts and mixing angles for $a = 1.32$ fm are shown in Fig. 4.2, for $a = 1.64$ fm in Fig. 4.3, and finally for $a = 1.97$ fm in Fig. 4.4. Together with the results for $a = 0.98$ fm shown in Fig. 4.1, it is immediately apparent that lattice spacing effects are small for the S-waves in the range $0 < p_{\text{CM}} < 200$ MeV, which is consistent with the behavior of the S-wave parameters. On the other hand, this situation is quite different for the P-waves and D-waves. For these higher partial waves, as well as for the mixing angles ϵ_1 and ϵ_2, the lattice spacing effects remain small only up to $p_{\text{CM}} < 100$ MeV.

Table 4.6: Summary of fit results (in units of a) for the perturbative NLO+N^{2}LO analysis at $a = 1.97$ fm. Fitted values of E_d are indicated by a dagger (†). Note that the values of $C_{^1\mathrm{S}_0}$, $C_{^3\mathrm{S}_1}$ and b_s are fixed by the LO fit.

	LO	NLO	N^{2}LO
$C_{^1\mathrm{S}_0}$	−0.462(8)	–	–
$C_{^3\mathrm{S}_1}$	−0.633(6)	–	–
b_s	0.054(3)	–	–
ΔC	–	−0.2(2)	−0.0(2)
ΔC_{I^2}	–	−0.02(9)	0.03(9)
C_{q^2}	–	0.03(5)	0.12(5)
$C_{\mathrm{I}^2,\mathrm{q}^2}$	–	0.04(2)	0.03(3)
$C_{\mathrm{S}^2,\mathrm{q}^2}$	–	−0.05(5)	−0.02(5)
$C_{\mathrm{S}^2,\mathrm{I}^2,\mathrm{q}^2}$	–	0.00(2)	−0.01(2)
$C_{(\mathrm{q}\cdot\mathrm{S})^2}$	–	0.06(2)	−0.05(2)
$C_{\mathrm{I}^2,(\mathrm{q}\cdot\mathrm{S})^2}$	–	−0.10(2)	−0.07(2)
$C^{I=1}_{(\mathrm{q}\times\mathrm{S})\cdot\mathrm{k}}$	–	0.039(5)	0.038(5)
E_d [MeV]	−2.02(4)	−2.224(3)†	−2.224(3)†

For $p_\mathrm{CM} > 100$ MeV, the deviations from the Nijmegen PWA increase rapidly, but are nevertheless systematically reduced when a is decreased.

To conclude, for the S-waves the lattice spacing effects remain small throughout the range of p_CM considered here, even for the (rather coarse) lattice spacing of $a = 1.97$ fm. For the P-waves and D-waves, this situation holds only up to $p_\mathrm{CM} \simeq 100$ MeV. However, we note that $a = 0.98$ fm suffices to give an accurate description for $p_\mathrm{CM} \simeq 200$ MeV, regardless of the channel under consideration. This suggests that the observed discrepancies could be eliminated by a combination of improved lattice momentum operators and N^{3}LO effects, possibly taken together with a lattice spacing somewhat smaller than $a = 1.97$ fm. We would like to stress that the phase shifts agree within uncertainties below 150 MeV (with a few exceptions) for the lattice spacings considered. This validates the statements made in Ref. [27] about the lattice spacing independence of observables in the NN sector.

4.5 Perturbative Treatment of Higher Orders

We have thus far demonstrated that non-perturbative fits to np scattering data are feasible to any given order in NLEFT, provided that the requisite potential operators have been worked out. Nevertheless, for

Table 4.7: Summary of fit results (in units of a) for the perturbative NLO+N^{2}LO analysis at $a = 1.64$ fm. Notation as in Table 4.6.

	LO	NLO	N^{2}LO
$C_{^1S_0}$	−0.47(1)	–	–
$C_{^3S_1}$	−0.64(1)	–	–
b_s	0.091(5)	–	–
ΔC	–	−0.2(2)	0.3(3)
ΔC_{I^2}	–	−0.00(9)	0.1(1)
C_{q^2}	–	0.04(6)	0.18(6)
C_{I^2,q^2}	–	0.08(3)	0.06(3)
C_{S^2,q^2}	–	−0.05(5)	0.00(6)
C_{S^2,I^2,q^2}	–	−0.01(3)	−0.01(3)
$C_{(q\cdot S)^2}$	–	0.06(3)	0.08(4)
$C_{I^2,(q\cdot S)^2}$	–	−0.07(3)	−0.06(4)
$C^{I=1}_{(q\times S)\cdot k}$	–	0.051(9)	0.05(1)
E_d [MeV]	−2.13(4)	$-2.224(2)^\dagger$	$-2.224(2)^\dagger$

practical reasons (such as sign oscillations and increased computational complexity) the contributions of NLO and higher orders are usually treated perturbatively in MC simulations of nuclear many-body systems. With this in mind, we show here how our analysis of phase shifts and mixing angles can be applied in a way consistent with current lattice MC work.

Before discussing our results, we briefly summarize the differences between the perturbative and non-perturbative analyses. We again start with a LO fit, the parameters of which are fixed by fitting the $^1S_0$ and $^3S_1$ channels (but not E_d). As in the non-perturbative analysis, for the LO fits we consider data up to $p_{\rm CM}^{\rm max} = 100$ MeV. For higher-order (NLO and N^{2}LO) fits, we include data up to $p_{\rm CM}^{\rm max} = 150$ MeV. Since higher orders in NLEFT are treated perturbatively, the transfer matrix is constructed in a different way than in Eq. (4.52). To be specific, in the perturbative analysis the transfer matrix is and as in previous MC studies of NLEFT, we introduce the additional operators Ref. [14]

$$\Delta V \equiv \Delta C \tag{4.56}$$

$$\Delta V_{I^2} \equiv \Delta C_{I^2}\, \boldsymbol{\tau}_1 \cdot \boldsymbol{\tau}_2 \,, \tag{4.57}$$

which we classify as NLO perturbations and add to the NLO potential in Eq. (4.54) when $M^{\rm pert}$ is

Table 4.8: Summary of fit results (in units of a) for the perturbative NLO+N^{2}LO analysis at $a = 1.32$ fm. Notation as in Table 4.6.

	LO	NLO	N^{2}LO
$C_{^1S_0}$	−0.44(1)	–	–
$C_{^3S_1}$	−0.59(1)	–	–
b_s	0.18(1)	–	–
ΔC	–	0.0(2)	0.4(2)
ΔC_{I^2}	–	0.05(9)	0.30(9)
C_{q^2}	–	0.04(6)	0.62(6)
C_{I^2,q^2}	–	0.19(4)	0.07(3)
C_{S^2,q^2}	–	−0.03(5)	0.07(5)
C_{S^2,I^2,q^2}	–	−0.01(3)	−0.12(3)
$C_{(q\cdot S)^2}$	–	0.09(4)	0.02(4)
$C_{I^2,(q\cdot S)^2}$	–	−0.05(4)	0.12(4)
$C^{I=1}_{(q\times S)\cdot k}$	–	0.12(1)	0.11(1)
E_d [MeV]	−2.14(3)	−2.224(1)†	−2.224(1)†

computed. This is achieved because the LO LECs are kept fixed and thus fitting these finite shifts is equivalent to a refit of the LO LECs, as it is done in the non-perturbative case. Additionally, ΔV and ΔV_{I^2} absorb part of the (sizable) short-distance contributions from TPE at NLO and N^{2}LO. At NLO, we also studied an operator of the form $\sum_i \tau_{1,i}\tau_{2,i}q_i^2$ which accounts for rotational symmetry breaking effects on the lattice, but no significant effects were observed.

As for the non-perturbative case, we give results for a range of lattice spacings for the perturbative analysis. The fitted parameters for $a = 1.97$ fm, $a = 1.64$ fm and $a = 1.32$ fm are given in Tables 4.6, 4.7 and 4.8, respectively. The corresponding phase shifts and mixing angles are shown in Figs. 4.5, 4.6 and 4.7. For each computed phase shift, we provide an estimated uncertainty according to

$$\Delta\delta \equiv \sqrt{(J_\delta^T)_i \mathcal{E}_{ij} (J_\delta)_j} \times \sqrt{\chi^2_{\text{min}}/N_{\text{dof}}}\,, \tag{4.58}$$

where $\mathcal{E}_{ij}$ denotes the variance-covariance matrix of the fitted parameters, according to Eq. (A.4), and J_δ is the Jacobian vector of the phase shift (or mixing angle) in question. The last factor in Eq. (4.58) is the so-called Birge factor described in App. A, which approximately accounts for the systematical errors in the analysis.

At LO, we reproduce well the low-momentum region, and obtain a realistic deuteron binding energy.

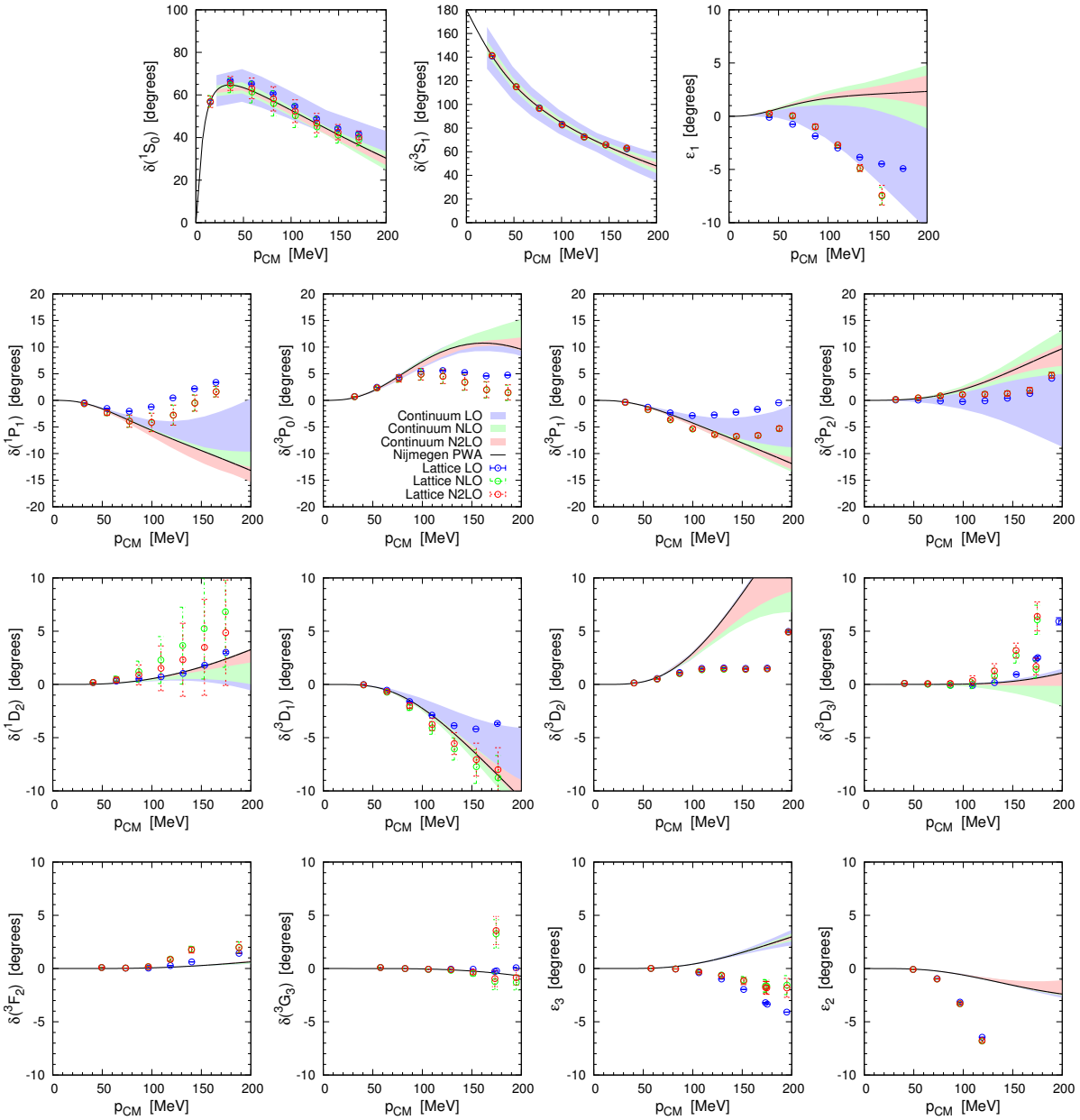

Figure 4.5: Fitted LO + perturbative NLO/N^{2}LO np phase shifts and mixing angles for $a = 1.97$ fm. The shaded bands denote the continuum results of Ref. [37], and the NPWA is given by the black line.

In particular, we note that the $^3S_1$ PWA data are almost perfectly reproduced. This is largely caused by the very accurate PWA data of this channel, which gives this channel a relatively high weight in the χ^2 function. We note that this may potentially worsen the agreement in other channels, where a comparable accuracy of the PWA data is not available. Also, the expectation is that the P-waves should be well described at LO, since they are dominated by the OPE potential contribution. The reason why this is

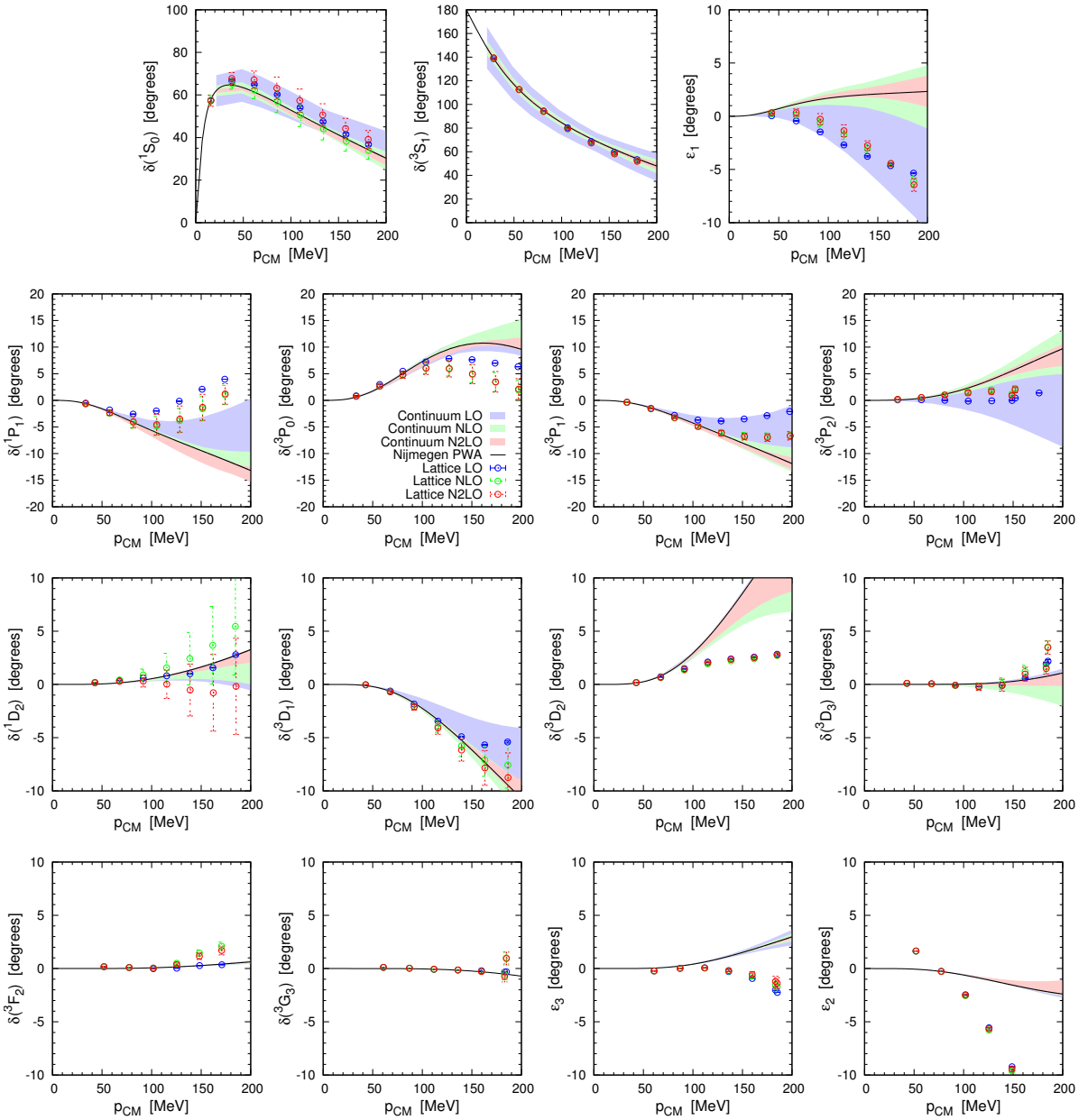

Figure 4.6: Fitted LO + perturbative NLO/N^{2}LO np phase shifts and mixing angles for $a = 1.64$ fm. The shaded bands denote the continuum results of Ref. [37], and the NPWA is given by the black line.

not the case for our LO results is that, in the perturbative calculation, and in order to be consistent with the MC simulations, we treat the momentum $\mathbf{q}^2$ in the denominator of the OPE as in Eq. (4.25), and factors of $\mathbf{q}$ as in Eq. (4.26). This choice considerably suppresses the OPE potential contribution already at intermediate momenta, which worsens the description of the P-waves.

Moving to NLO, a significant improvement is found in some channels, particularly for ^{1}P$_1$ and ^{3}P$_1$,

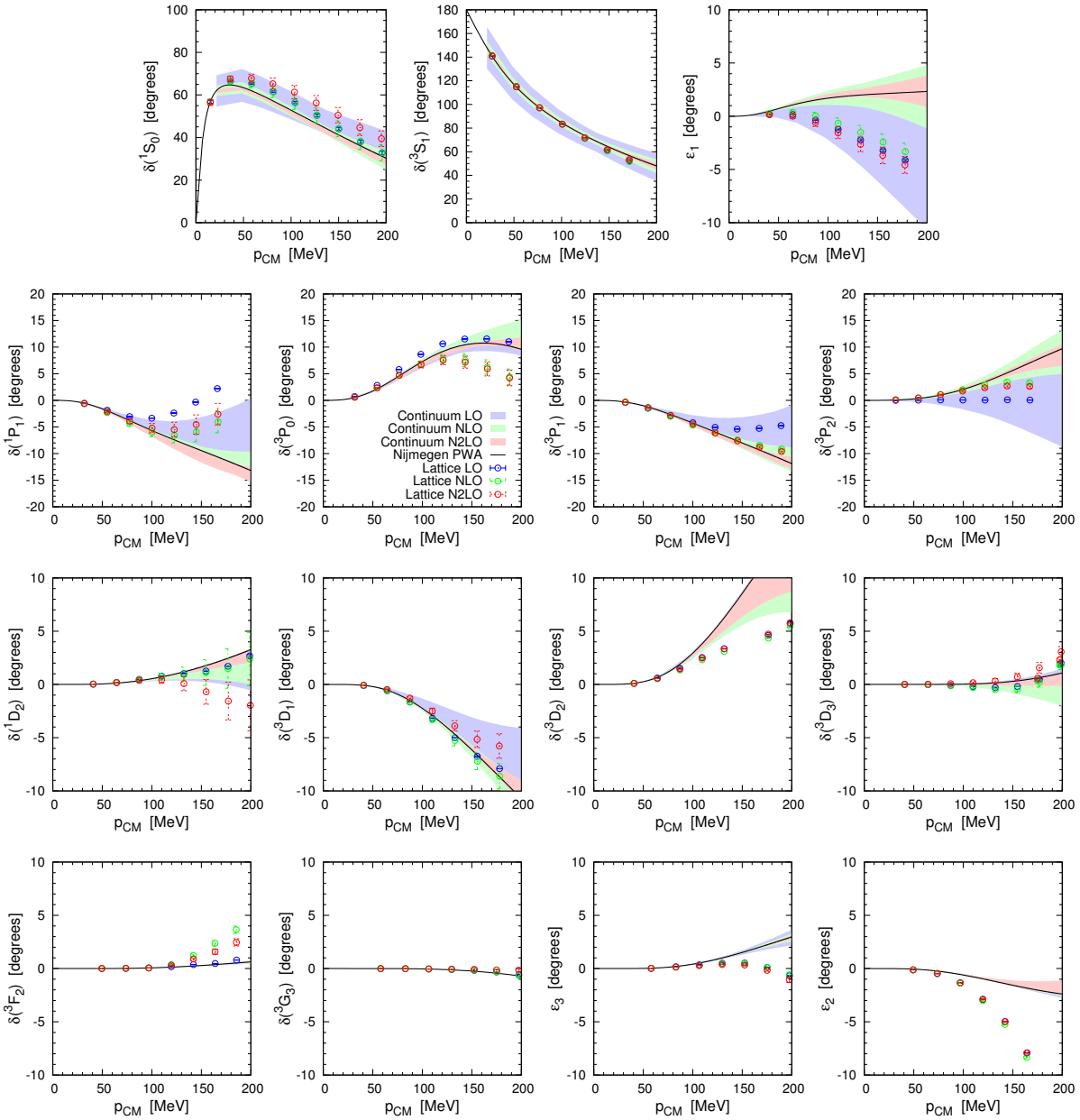

Figure 4.7: Fitted LO + perturbative NLO/N^{2}LO np phase shifts and mixing angles for $a = 1.32$ fm. The shaded bands denote the continuum results of Ref. [37], and the NPWA is given by the black line.

where the PWA is now well described up to $\sim$ 100 MeV. On the other hand, we note that the $^3P_0$ and $^3P_2$ channels, as well as the D-waves, show little improvement. We attribute these features to the deficiencies in the OPE as mentioned above. The description of the S-wave channels is found to improve at intermediate momenta, which is mainly due to the NLO CTs and to the parts of the NLO TPE potential that contribute to the S-waves.

At N^{2}LO, while no new unknown parameters contribute, the sub-leading TPE potential enters as a prediction from πN scattering in χEFT. Thus, the NLO constants are refitted at N^{2}LO in order to absorb the strong short-distance isoscalar contributions from the πN LECs. The NLO and N^{2}LO results appear in most cases virtually indistinguishable (as shown in Fig. 4.5) as far as the level of agreement with the PWA is concerned, except for the ^{1}D$_2$ channel where the high-momentum tail is noticeably improved.

For our perturbative analysis, we have also compared the computed scattering observables at different orders in NLEFT with the continuum results of Ref. [37]. We find that our S-waves agree with the continuum results (within errors) up to at least $p_{\mathrm{CM}} \simeq 100$ MeV, and in some cases over the entire range of momenta considered. The P-waves show good agreement within errors only for some channels, and only for NLO/N^{2}LO. As already mentioned, this is mainly due to the non-optimal description of OPE at LO. For the D-wave channels, only ^{3}D$_1$ shows good agreement with the continuum calculations. For the ^{1}D$_2$ channel, the LO and NLO results overshoot the continuum error band, while the N^{2}LO result is in agreement due to the large uncertainty. For ^{3}D$_2$, the NLO/N^{2}LO terms do not contribute at all and hence cannot improve the result. Further, for ^{3}D$_3$ the lattice calculations start to deviate from the PWA and the continuum results for $p_{\mathrm{CM}} > 100$ MeV.

Finally, it is important to stress that for cms momenta below 150 MeV, the phase shifts agree within the uncertainties (with the exception of ϵ_1, were deviations set in at about 110 MeV). This validates the statements made in Ref. [27] about the lattice spacing independence of observables in the NN sector.

4.6 Further Improvements

Next, we shall discuss two problems that require further study to resolve. First, while a clear improvement was observed in the non-perturbative case for the scattering observables (and fitted parameters) as a was decreased, a similar improvement is not found in the perturbative analysis. At LO, the quality of the description improves in general with decreasing a, particularly for the ^{3}S$_1$-^{3}D$_1$ coupled channel. However, at NLO/N^{2}LO the picture is more complicated. We note that the P-waves and remaining D-wave channels do improve, but the description of the ^{1}S$_0$ and ^{3}S$_1$-^{3}D$_1$ channels may in fact deteriorate for smaller a. We attribute this effect to the increasing influence of the TPE potential. While the effect of TPE on the S-waves can be absorbed by smeared contact interactions as was done in the non-perturbative calculation, in the perturbative case we only have standard (without smearing) contact interactions available. This is sufficient for $a = 1.97$ fm, as the TPE potential contribution then closely resembles a contact interaction.

Table 4.9: Summary of fit results with perturbatively improved OPE (in units of a) for the perturbative NLO+N^{2}LO analysis at $a = 1.97$ fm. Notation as in Table 4.6.

	LO	NLO	N^{2}LO
$C_{^1S_0}$	−0.462(8)	–	–
$C_{^3S_1}$	−0.633(6)	–	–
b_s	0.054(3)	–	–
ΔC	–	−0.2(3)	−0.0(3)
ΔC_{I^2}	–	−0.1(1)	0.03(9)
C_{q^2}	–	−0.03(7)	0.05(7)
C_{I^2,q^2}	–	0.09(3)	0.06(3)
C_{S^2,q^2}	–	−0.05(6)	0.00(6)
C_{S^2,I^2,q^2}	–	0.00(2)	−0.03(3)
$C_{(q\cdot S)^2}$	–	0.02(2)	−0.03(3)
$C_{I^2,(q\cdot S)^2}$	–	−0.07(2)	0.10(3)
$C^{I=1}_{(q\times S)\cdot k}$	–	0.014(7)	0.012(5)
E_d [MeV]	−2.02(4)	−2.224(3)†	−2.224(3)†

A possible solution for smaller a would be to include a smeared version of the NLO/N^{2}LO contact interactions. Alternatively, one could use exact momentum operators for the NLO CTs, which do have a higher influence at larger momenta. This was not necessary nor observable for $a = 1.97$ fm, but may improve the $^3S_1$ channel once a is decreased. Finally, we note that the choice of c_1, c_3 and c_4 may also have an effect, as it influences the strength of the different contribution to TPE potential. However, to use the full power of χEFT, one should utilize the values determined from pion-nucleon scattering.

Second, we show preliminary results including a perturbative improvement of the OPE operator. In order to remedy the aforementioned discrepancies in the peripheral partial waves such that consistency with the MC calculation is maintained, we introduce a new operator at NLO that accounts for the difference between OPE potential with the momenta of Eq. (4.25) and (4.26) and the "exact" lattice momentum $\mathbf{q}_{\text{ex}} \equiv 2\pi\mathbf{k}/L$. This gives

$$\Delta V_{\text{OPE}} \equiv -\frac{g_A^2}{4F_\pi^2}\,\boldsymbol{\tau}_1\cdot\boldsymbol{\tau}_2 \quad \left[\frac{(\boldsymbol{\sigma}_1\cdot\mathbf{q}_{\text{ex}})(\boldsymbol{\sigma}_2\cdot\mathbf{q}_{\text{ex}})}{\mathbf{q}_{\text{ex}}^2+M_\pi^2} - \frac{(\boldsymbol{\sigma}_1\cdot\mathbf{q})(\boldsymbol{\sigma}_2\cdot\mathbf{q})}{\mathbf{q}^2+M_\pi^2}\right], \tag{4.59}$$

so that by adding ΔV_{OPE} to V_{OPE}, one recovers OPE potential with the exact momentum. It should be noted that this differs slightly from treating OPE potential at LO with the exact momentum, since

$\Delta V_{\rm OPE}$ is treated as a perturbation, while $V_{\rm OPE}$ is implemented non-perturbatively. Also, $\mathbf{q}$ approaches $\mathbf{q}_{\rm ex}$ as $a \to 0$. This means that, simultaneously, $\Delta V_{\rm OPE}$ becomes less important, and $V_{\rm OPE}$ gives a better description of the P-waves, as we approach the continuum limit. This is consistent with Figs. 4.2-4.4 of the non-perturbative calculation, where the P-waves clearly improve as a decreases.

Our perturbative results with $\Delta V_{\rm OPE}$ included are given in Fig. 4.8 and Table 4.9, where as expected one can observe a clear improvement in the description of the P-waves. The experimental results for the ^{1}P$_1$, ^{3}P$_0$ and ^{3}P$_1$ channels are now well reproduced for the range of fitted momenta $p_{\rm CM} < 150$ MeV. In general, we find that all the P-wave channels and the ϵ_1 mixing angle appear much closer to the PWA at NLO with improved OPE, than without this correction. Additionally, we find that the D-waves (except for the ^{3}D$_3$ channel) also improve significantly with respect to the LO result. In the case of ^{3}D$_3$, the correction is too large and so the computed values fall below the PWA ones. Again, this improvement is mostly attributable to $\Delta V_{\rm OPE}$, although we recall that the first order of TPE potential (NLO) also contributes to the high-momentum tails in some of the D-wave channels.

4.7 Nuclear Binding Energies

In MC simulations of NLEFT, the binding energies of nuclei receive perturbative energy shifts that depend on the NLO constants C_i and their uncertainties, in addition to any inherent MC uncertainties. For instance, in Ref. [41], only the MC errors were taken into account, and the C_i were assumed to be accurately known and uncorrelated. Since our analysis provides us with the complete variance-covariance matrix of the NLO parameters C_i, we are now in a position to estimate the uncertainties of the nuclear binding energies at N^{2}LO, due to uncertainties and correlations of the C_i. From our present results, we observe larger correlations between ΔC and C_q^2, between ΔC_I^2 and $C_{\rm I^2,q^2}$, between ΔC_I^2 and $C_{\rm S^2,q^2}$, and also between $C_{\rm (q\cdot S)^2}$ and $C_{\rm I^2,(q\cdot S)^2}$.

In order to obtain a first, rough estimate of the relative magnitude of MC and fitting errors in calculations of nuclear binding energies E_B, we recall that these are calculated according to

$$E_B^{\rm N^2LO} = E_B^{\rm LO} + C_i \frac{\partial E_B}{\partial C_i}\bigg|_{C_i=0}, \tag{4.60}$$

where summation over i is assumed. In the MC calculation, the LO binding energies are computed non-perturbatively, and the second term in Eq. (4.60) represents the perturbative shift due to the NLO

constants C_i in the 2NF, which we take from Ref. [41]. We note that

$$E_B^{\mathrm{N^2LO}} \equiv E_B(C_{^1\mathrm{S}_0}, C_{^3\mathrm{S}_1}, b_s, C_i)\,, \tag{4.61}$$

is a function of all the coupling constants up to N^{2}LO, while the LO values

$$E_B^{\mathrm{LO}} \equiv E_B(C_{^1\mathrm{S}_0}, C_{^3\mathrm{S}_1}, b_s, C_i = 0)\,, \tag{4.62}$$

equal to the binding energies at $C_i = 0$. In terms of the variance-covariance matrix from the perturbative analysis in Section 4.5,

$$\Delta E_B^{\mathrm{N^2LO}} = \sqrt{\left.\frac{\partial E_B}{\partial C_i}\right|_{C_i=0} \mathcal{E}_{ij} \left.\frac{\partial E_B}{\partial C_j}\right|_{C_j=0}}\,, \tag{4.63}$$

gives us the uncertainties in the N^{2}LO energy shifts due to the fitting errors of the C_i. The results so obtained are given in Table 4.10.

We note that the errors due to the uncertainties in the C_i are of comparable magnitude to the MC errors, even when $\mathcal{E}_{ij}$ has been evaluated without consideration of the systematical errors encoded by the Birge factor. This may suggest that the procedure of fixing the C_i from NN data may, at present, be the main factor limiting the accuracy of NLEFT calculations beyond LO for heavier nuclei. This issue is currently under further investigation. It should also be noted that the quoted NLEFT binding energies in Table 4.10 are not expected to coincide with the empirical ones, as the three-nucleon (3N) and higher-order contributions have been neglected (see Ref. [41] for further discussion).

Table 4.10: Nuclear binding energies with 2N forces up to N^{2}LO in the NLEFT expansion for $a = 1.97$ fm, data taken from Ref. [41]. The first parenthesis gives the estimated Monte Carlo error in the calculation of $E_B^{\mathrm{N^2LO}}$, and the second parenthesis the error due to variance-covariance matrix in Eq. (4.63). For reference, we also show the experimental binding energies.

	$E_B^{\mathrm{N^2LO}}$(2N)	E_B(exp)
^{4}He	−25.60(6)(2)	−28.30
^{8}Be	−48.6(1)(3)	−56.35
^{12}C	−78.7(2)(5)	−92.16
^{16}O	−121.4(5)(7)	−127.62
^{20}Ne	−163.6(9)(9)	−160.64
^{24}Mg	−208(2)(2)	−198.26
^{28}Si	−275(3)(2)	−236.54

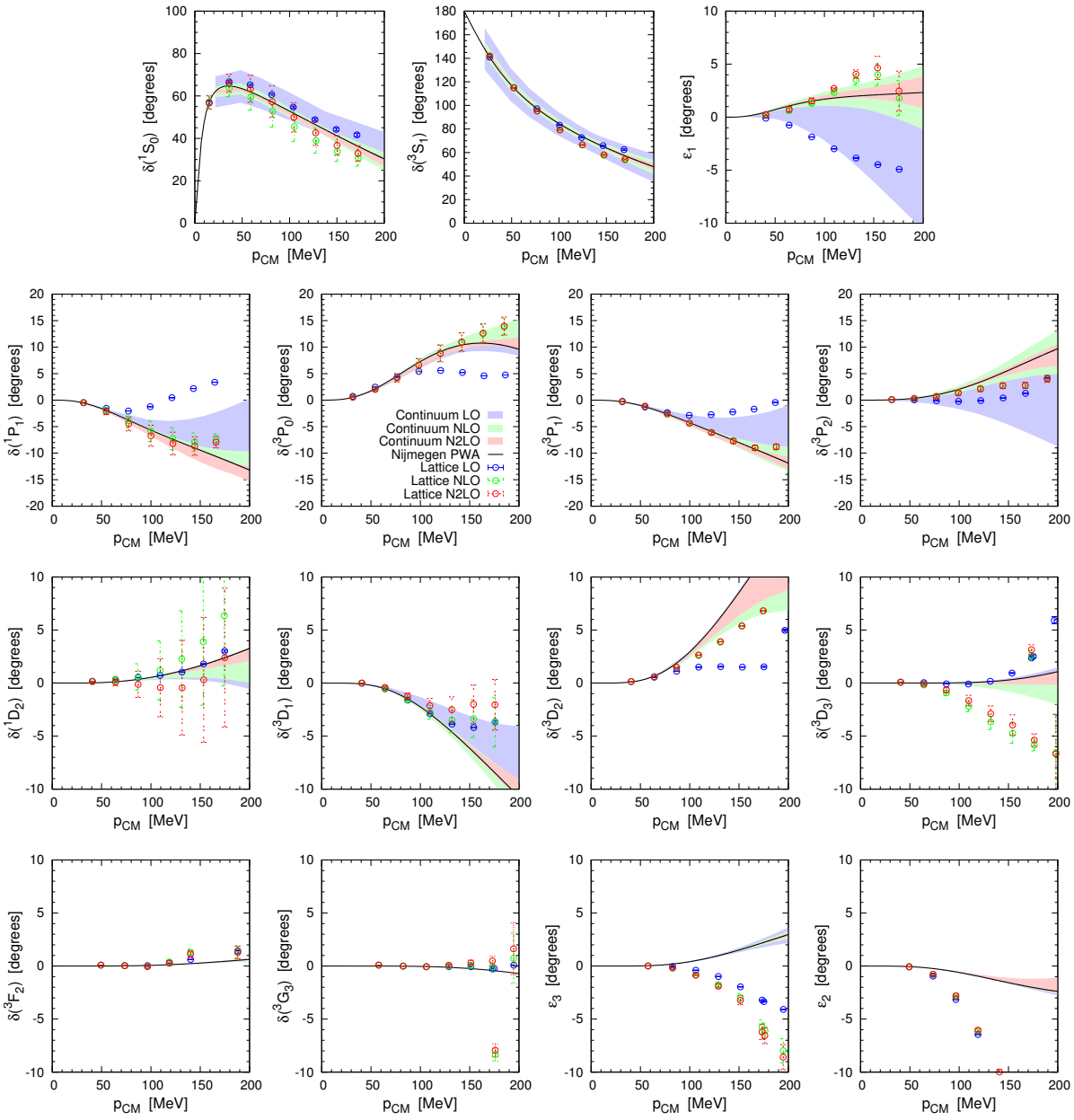

Figure 4.8: Fitted LO + perturbative NLO/N^{2}LO np phase shifts and mixing angles for $a = 1.97$ fm including the improved OPE. The shaded bands denote the continuum results of Ref. [37], and the NPWA is given by the black line.

CHAPTER 5

Two-Nucleon Scattering with Coulomb Potential: Numerical Results

We investigate the two-nucleon (NN) system at N^{3}LO in χEFT which consists of one-, two-, and three pion exchange potential and a set of contact interactions with zero, two and four derivatives. Nucleonic fields and effective interactions are located on the lattice within the framework of spectral function regularization for the multi-pion exchanges. Ref. [31] has shown that three-pion exchange (3PE) is negligibly small so that we do not consider about it. This section is a small extension of Ref. [42, 43] in which the nature of nuclear clustering at LO has been studied. This is the first attempt to give information for N^{3}LO LECs including TPEs with/without Coulomb interaction by fitting phase shifts of neutron-proton (np) or proton-proton (pp) scattering process. We use a definition of contact interactons different from Sec. 4 which has been described in Sec. 3.3.2. We discuss how Coulomb interaction plays its role in NN scattering process, Ref. [15], and further give LECs of high derivatives terms up to N^{3}LO including Coulomb interaction. The fitting results can be used to perturbatively calculate in-depth information for many-body nuclei.

5.1 Lattice Notations

We use a spatial lattice spacing $a = (100\ \mathrm{MeV})^{-1} = 1.97$ fm and time lattice step $a_t = (100\ \mathrm{MeV})^{-1} = 1.97$ fm and write α_t for the ratio a_t/a. Axial-vector coupling constant is $g_\mathrm{A} = 1.29$ as derived from the GTR, the pion decay constant is $f_\pi = 92.2$ MeV, and the neutral, charged and charge-averaged pion mass are $M_{\pi^0} = 134.98$ MeV, $M_{\pi^\pm} = 139.57$ MeV, $M_\pi = 138.03$ MeV, respectively. The nucleon mass is taken as $m = 938.92$ MeV, and the electromagnetic fine structure constant is $\alpha_\mathrm{EM} = 1/137$. We will use lattice units where the quantities are multiplied by the appropriate power of the spatial lattice spacing a to make the combination dimensionless.

Following Ref. [42], we construct a new short-range interactions smeared by nearest neighbors. a_NL denotes a four-component spin-isospin column vector while $a^\dagger_\mathrm{NL}$ is a four-component spin-isospin row vector. For real parameter s_NL, we define the nonlocal (NL) annihilation and creation operators for each spin and isospin component of the nucleon,

$$a_{i,j,s_\mathrm{NL}}(\mathbf{n}) = a_{i,j}(\mathbf{n}) + s_\mathrm{NL} \sum_{|\mathbf{n}'|=1} a_{i,j}(\mathbf{n}+\mathbf{n}')\,, \tag{5.1}$$

$$a^\dagger_{i,j,s_\mathrm{NL}}(\mathbf{n}) = a^\dagger_{i,j}(\mathbf{n}) + s_\mathrm{NL} \sum_{|\mathbf{n}'|=1} a^\dagger_{i,j}(\mathbf{n}+\mathbf{n}')\,, \tag{5.2}$$

For spin indices $S = 1, 2, 3$, and isospin indices $I = 1, 2, 3$, we define point-like densities,

$$\rho(\mathbf{n}) = a^\dagger(\mathbf{n})a(\mathbf{n})\,, \tag{5.3}$$

$$\rho_S(\mathbf{n}) = a^\dagger(\mathbf{n})[\sigma_S]a(\mathbf{n})\,, \tag{5.4}$$

$$\rho_I(\mathbf{n}) = a^\dagger(\mathbf{n})[\tau_I]a(\mathbf{n})\,, \tag{5.5}$$

$$\rho_{S,I}(\mathbf{n}) = a^\dagger(\mathbf{n})[\sigma_S \otimes \tau_I]a(\mathbf{n})\,. \tag{5.6}$$

and also the smeared nonlocal densities,

$$\rho_\mathrm{NL}(\mathbf{n}) = a^\dagger_\mathrm{NL}(\mathbf{n})a_\mathrm{NL}(\mathbf{n})\,, \tag{5.7}$$

$$\rho_{S,\mathrm{NL}}(\mathbf{n}) = a^\dagger_\mathrm{NL}(\mathbf{n})[\sigma_S]a_\mathrm{NL}(\mathbf{n})\,, \tag{5.8}$$

$$\rho_{I,\mathrm{NL}}(\mathbf{n}) = a^\dagger_\mathrm{NL}(\mathbf{n})[\tau_I]a_\mathrm{NL}(\mathbf{n})\,, \tag{5.9}$$

$$\rho_{S,I,\mathrm{NL}}(\mathbf{n}) = a^\dagger_\mathrm{NL}(\mathbf{n})[\sigma_S \otimes \tau_I]a_\mathrm{NL}(\mathbf{n})\,. \tag{5.10}$$

We focus on the Hamiltonian of interest in this section

$$\begin{aligned} H = H_{\text{free}} + V_0 + V_{1\pi} + V_{\text{coul}} \quad &\rightarrow \text{(LO)} \\ + \left(\Delta V_{\text{ct},0} + V_{\text{ct},2}\right) + V_{2\pi,2} + V_{1\pi,\text{IB}} \quad &\rightarrow \text{(NLO)} \\ + \left(V_{\text{pp}} + V_{\text{nn}}\right) \quad + V_{2\pi,3} \quad &\rightarrow \text{(N}^2\text{LO)} \\ + \left(V_{\text{ct},4}\right) \quad\quad + V_{2\pi,4} \quad &\rightarrow \text{(N}^3\text{LO)} \end{aligned} \tag{5.11}$$

with $V_{1\pi,\text{IB}}$ denoting isospin-breaking OPE and $V_{\text{ct},4}$ contact interactions at order Q^4. The kinetics of nucleons H_{free} takes the form as Eq. (4.1). The OPE interaction $V_{1\pi}$ has the form

$$V_{1\pi} = \frac{1}{2} : \sum_{\mathbf{n_1},\mathbf{n_2},S_1,S_2,I} \rho_{S_1,I}(\mathbf{n_1}) f_{S_1S_2}(\mathbf{n_1}-\mathbf{n_2}) \rho_{S_2,I}(\mathbf{n_2}) : , \tag{5.12}$$

where $f_{S_1S_2}$ is defined as

$$f_{S_1S_2}(\mathbf{n_1}-\mathbf{n_2}) = \frac{1}{L^3} \sum_{\mathbf{k}} \exp\left[i\frac{2\pi}{L}\mathbf{k}\cdot(\mathbf{n_1}-\mathbf{n_2})\right] \times F^{(1\pi)}_{S_1S_2}(\mathbf{k}) \tag{5.13}$$

with

$$F^{(1\pi)}_{S_1S_2}(\mathbf{k}) = -\frac{g_A^2}{4f_\pi^2}\frac{q_{S_1}q_{S_2}}{\mathbf{q}^2+M_{\pi^0}^2} \times \exp\left[-b_\pi \mathbf{q}^2\right] , \tag{5.14}$$

and each lattice momentum component q_S is an integer k_S multiplied by $2\pi/L$. The :: symbol indicates normal ordering, where the annihilation operators are on the right-hand side and the creation operators are on the left-hand side. There is a subtle difference from the pion exchanges used in Sec. 4, as well as Ref. [25], that those used in this section are all smeared by a Gaussian factor with parameter b_π in order to remove short-distance lattice artifacts. It results in better preservation of rotational symmetry and will be especially useful at smaller lattice spacings, Ref. [27]. Two-pion exchanges at order Q^2 and Q^3, $V_{2\pi,2}$ and $V_{2\pi,3}$, are given by Eqs. (4.29) and (4.40) along with the Gaussian smearing. In this work, we use the value of $b_\pi = 0.700$.

We have a series of TPE diagrams at N^{3}LO, Fig. 2.1. The full TPE at N^{3}LO of nucleon-nucleon potential are presented in Ref. [44] using dimensional regularization. In Ref. [31], another scheme of the spectral function regularization is used to derive the divergent loop integrals in order to improve the singularity of short-range behavior. In this work, we only take the bubble diagram and two-loop diagram

into account. Their expressions in terms of transfer and average momenta $\{\mathbf{q}, \mathbf{k}\}$ are given in App. B so that we have $V_{2\pi,4}(\mathbf{q})$ by summing Eqs. (B.10)-(B.15) with their corresponding spin-isopin structures. We present these pion exchange interactions in position space by density operators. The bubble diagram (bbl) is

$$V_{2\pi}^{(4,\mathrm{bbl})} = \frac{1}{2} : \sum_{\mathbf{n}_1,\mathbf{n}_2} V_{\mathrm{C}}^{(4,\mathrm{bbl})}(\mathbf{n}_1-\mathbf{n}_2)\rho(\mathbf{n}_1)\rho(\mathbf{n}_2) : + \frac{1}{2} : \sum_{\mathbf{n}_1,\mathbf{n}_2}\sum_{S,I} W_{\mathrm{S}}^{(4,\mathrm{bbl})}(\mathbf{n}_1-\mathbf{n}_2)\rho_{S,I}(\mathbf{n}_1)\rho_{S,I}(\mathbf{n}_2) :$$
$$+ \frac{1}{2} : \sum_{\mathbf{n}_1,\mathbf{n}_2}\sum_{S_1,S_2,I} T_{S_1,S_2}^{(4,\mathrm{bbl})}(\mathbf{n}_1-\mathbf{n}_2)\rho_{S_1,I}(\mathbf{n}_1)\rho_{S_2,I}(\mathbf{n}_2) : , \tag{5.15}$$

and the two-loop diagram (lp) regularized by spectral funtion is

$$V_{2\pi}^{(4,\mathrm{lp})} = \frac{1}{2} : \sum_{\mathbf{n}_1,\mathbf{n}_2} V_{\mathrm{C}}^{(4,\mathrm{lp})}(\mathbf{n}_1-\mathbf{n}_2)\rho(\mathbf{n}_1)\rho(\mathbf{n}_2) : + \frac{1}{2} : \sum_{\mathbf{n}_1,\mathbf{n}_2}\sum_{I} W_{\mathrm{C}}^{(4,\mathrm{lp})}(\mathbf{n}_1-\mathbf{n}_2)\rho_I(\mathbf{n}_1)\rho_I(\mathbf{n}_2) : \tag{5.16}$$
$$+ \frac{1}{2} : \sum_{\mathbf{n}_1,\mathbf{n}_2}\sum_{S} V_{\mathrm{S}}^{(4,\mathrm{lp})}(\mathbf{n}_1-\mathbf{n}_2)\rho_S(\mathbf{n}_1)\rho_S(\mathbf{n}_2) : + \frac{1}{2} : \sum_{\mathbf{n}_1,\mathbf{n}_2}\sum_{S,I} W_{\mathrm{S}}^{(4,\mathrm{lp})}(\mathbf{n}_1-\mathbf{n}_2)\rho_{S,I}(\mathbf{n}_1)\rho_{S,I}(\mathbf{n}_2) :$$
$$+ \frac{1}{2} : \sum_{\mathbf{n}_1,\mathbf{n}_2}\sum_{S_1,S_2} T_{S_1,S_2}^{(4,\mathrm{lp1})}(\mathbf{n}_1-\mathbf{n}_2)\rho_{S_1}(\mathbf{n}_1)\rho_{S_2}(\mathbf{n}_2) : + \frac{1}{2} : \sum_{\mathbf{n}_1,\mathbf{n}_2}\sum_{S_1,S_2,I} T_{S_1,S_2}^{(4,\mathrm{lp2})}(\mathbf{n}_1-\mathbf{n}_2)\rho_{S_1,I}(\mathbf{n}_1)\rho_{S_2,I}(\mathbf{n}_2) : ,$$

where V_{C}, W_{C}, V_{S}, W_{S}, T are fourier transformation of Eqs. (B.10)-(B.15) with a Gaussian smearing factor similar to Eq. (5.14). E.G.,

$$W_{\mathrm{S}}^{(4,\mathrm{bbl})}(\mathbf{n}_1-\mathbf{n}_2) = \frac{1}{L^3}\sum_{\mathbf{k}} \exp\left[i\frac{2\pi}{L}\mathbf{k}\cdot(\mathbf{n_1}-\mathbf{n_2})\right] \times W_{\mathrm{S}}^{(4,\mathrm{bbl})}(\mathbf{k}) , \tag{5.17}$$
$$T_{S_1,S_2}^{(4,\mathrm{bbl})}(\mathbf{n}_1-\mathbf{n}_2) = \frac{1}{L^3}\sum_{\mathbf{k}} \exp\left[i\frac{2\pi}{L}\mathbf{k}\cdot(\mathbf{n_1}-\mathbf{n_2})\right] \times T_{S_1S_2}^{(4,\mathrm{bbl})}(\mathbf{k}) , \tag{5.18}$$
$$T_{S_1,S_2}^{(4,\mathrm{lp1})}(\mathbf{n}_1-\mathbf{n}_2) = \frac{1}{L^3}\sum_{\mathbf{k}} \exp\left[i\frac{2\pi}{L}\mathbf{k}\cdot(\mathbf{n_1}-\mathbf{n_2})\right] \times T_{S_1S_2}^{(4,\mathrm{lp1})}(\mathbf{k}) , \tag{5.19}$$
$$T_{S_1,S_2}^{(4,\mathrm{lp2})}(\mathbf{n}_1-\mathbf{n}_2) = \frac{1}{L^3}\sum_{\mathbf{k}} \exp\left[i\frac{2\pi}{L}\mathbf{k}\cdot(\mathbf{n_1}-\mathbf{n_2})\right] \times T_{S_1S_2}^{(4,\mathrm{lp2})}(\mathbf{k}) , \tag{5.20}$$

with

$$W_{\mathrm{S}}^{(4,\mathrm{bbl})}(\mathbf{k}) = W_{\mathrm{S}}^{(4,\mathrm{bbl})}(q)\ \exp\left[-b_\pi\mathbf{q}^2\right] , \quad T_{S_1S_2}^{(4,\mathrm{bbl})}(\mathbf{k}) = q_{S_1}q_{S_2}\ W_{\mathrm{T}}^{(4,\mathrm{bbl})}(q)\ \exp\left[-b_\pi\mathbf{q}^2\right] ,$$
$$T_{S_1S_2}^{(4,\mathrm{lp1})}(\mathbf{k}) = q_{S_1}q_{S_2}\ V_{\mathrm{T}}^{(4,\mathrm{lp})}(q)\ \exp\left[-b_\pi\mathbf{q}^2\right] , \quad T_{S_1S_2}^{(4,\mathrm{lp2})}(\mathbf{k}) = q_{S_1}q_{S_2}\ W_{\mathrm{T}}^{(4,\mathrm{lp})}(q)\ \exp\left[-b_\pi\mathbf{q}^2\right] .$$

where $\mathbf{q}$ equals to integers $\mathbf{k}$ multiplied by $2\pi/L$ and q is modulus of $\mathbf{q}$. LECs in TPE are extracted from

the accurate Roy-Steiner analysis of pion-nucleon scattering, Ref. [6]. We make use of $c_1 = -1.10(3) \times 10^{-3}\text{MeV}^{-1}$, $c_3 = -5.54(6) \times 10^{-3}\text{MeV}^{-1}$, $c_4 = 4.17(4) \times 10^{-3}\text{MeV}^{-1}$, $\bar{d}_1 + \bar{d}_2 = 6.18(8) \times 10^{-6}\text{MeV}^{-2}$, $\bar{d}_3 = -8.91(9) \times 10^{-6}\text{MeV}^{-2}$, $\bar{d}_5 = 0.86(5) \times 10^{-6}\text{MeV}^{-2}$, $\bar{d}_{14} - \bar{d}_{15} = -12.18(12) \times 10^{-6}\text{MeV}^{-2}$.

The LO short-range interactions are developed from the zero-range interactions.

$$V_0 = \frac{c_0}{2} \sum_{\mathbf{n}',\mathbf{n},\mathbf{n}''} : \rho_{\text{NL}}(\mathbf{n}') f_{s_{\text{L}}}(\mathbf{n}' - \mathbf{n}) f_{s_{\text{L}}}(\mathbf{n} - \mathbf{n}'') \rho_{\text{NL}}(\mathbf{n}'') : \tag{5.21}$$

where $f_{s_{\text{L}}}$ is defined for real parameter s_{L} as

$$\begin{aligned} f_{s_{\text{L}}}(\mathbf{n}) &= 1 \text{ for } |\mathbf{n}| = 0 \,, \\ &= s_{\text{L}} \text{ for } |\mathbf{n}| = 1 \,, \\ &= 0 \text{ otherwise} \,. \end{aligned} \tag{5.22}$$

In Ref. [42] the parameters s_{NL}, s_{L}, c_0 are fitted by the average inverse scattering length and effective range of the two s-wave channels, as well as the finite-volume energies of ^{8}Be. Throughout this work, they are taken as $s_{\text{NL}} = 0.0800$, $s_{\text{L}} = 0.0800$, and $c_0 = -18.50 \times 10^{-6}\text{MeV}^{-2}$.

High order contact interactions are contructed in Sec. 3.3.2 and listed in detail in App. C, Eqs. (C.5)-(C.28), by point-like annihilation and creation operators which are replaced for nonlocal smeared formalism, Eqs. (5.1)-(5.2), in this work,

$$\Delta V_{\text{ct},0} = \Delta C_{0,{}^1\text{S}_0} V^{(0)}_{{}^1\text{S}_0} + \Delta C_{0,{}^3\text{S}_1} V^{(0)}_{{}^3\text{S}_1} \tag{5.23}$$

$$\begin{aligned} V_{\text{ct},2} = {} & C_{2,{}^1\text{S}_0} V^{(2)}_{{}^1\text{S}_0} + C_{2,{}^3\text{S}_1} V^{(2)}_{{}^3\text{S}_1} + C_{2,{}^1\text{P}_1} V^{(2)}_{{}^1\text{P}_1} \\ & + C_{2,{}^3\text{P}_0} V^{(2)}_{{}^3\text{P}_0} + C_{2,{}^3\text{P}_1} V^{(2)}_{{}^3\text{P}_1} + C_{2,{}^3\text{P}_2} V^{(2)}_{{}^3\text{P}_2} + C_{2,{}^3\text{SD}_1} V^{(2)}_{{}^3\text{SD}_1} \end{aligned} \tag{5.24}$$

$$\begin{aligned} V_{\text{ct},4} = {} & D_{4,{}^1\text{S}_0;1} V^{(4)}_{{}^1\text{S}_0;1} + D_{4,{}^1\text{S}_0;2} V^{(4)}_{{}^1\text{S}_0;2} + D_{4,{}^3\text{S}_1;1} V^{(4)}_{{}^3\text{S}_1;1} + D_{4,{}^3\text{S}_1;2} V^{(4)}_{{}^3\text{S}_1;2} \\ & + D_{4,{}^1\text{P}_1} V^{(4)}_{{}^1\text{P}_1} + D_{4,{}^3\text{P}_0} V^{(4)}_{{}^3\text{P}_0} + D_{4,{}^3\text{P}_1} V^{(4)}_{{}^3\text{P}_1} + D_{4,{}^3\text{P}_2} V^{(4)}_{{}^3\text{P}_2} \\ & + D_{4,{}^1\text{D}_2} V^{(4)}_{{}^1\text{D}_2} + D_{4,{}^3\text{D}_1} V^{(4)}_{{}^3\text{D}_1} + D_{4,{}^3\text{D}_2} V^{(4)}_{{}^3\text{D}_2} + D_{4,{}^3\text{D}_3} V^{(4)}_{{}^3\text{D}_3} \\ & + D_{4,{}^3\text{SD}_1;1} V^{(4)}_{{}^3\text{SD}_1;1} + D_{4,{}^3\text{SD}_1;2} V^{(4)}_{{}^3\text{SD}_1;2} + D_{4,{}^3\text{PF}_2} V^{(4)}_{{}^3\text{PF}_2} \end{aligned} \tag{5.25}$$

IB has been addressed in Ref. [45]. In this work, the IB is taken from NLO, of the same size as $O(Q^2)$, into account except Coulomb potential. For the sake of simplicity, we consider the first order isospin-breaking

contribution of OPE taking place at $O(Q^2)$ and that of short-range interactions taking place at $O(Q^3)$. The IB effect of OPE originates from the different masses of pion triplet, Eq. (3.7). In OPE potential, the pion mass is neutral, $M_{\pi^0} = 134.98$ MeV, and we know from Eq. (3.91) that the difference between isospin-symmetric OPE, Eq. (5.12), and isospin-breaking OPE can be written as, Ref. [15],

$$V_{1\pi,\mathrm{IB}} = \frac{1}{2} : \sum_{\mathbf{n_1},\mathbf{n_2}} \sum_{S_1,S_2} \sum_{I=\{1,2\}} \rho_{S_1,I}(\mathbf{n_1}) T^{(\mathrm{IB})}_{S_1S_2}(\mathbf{n_1}-\mathbf{n_2}) \rho_{S_2,I}(\mathbf{n_2}) : , \tag{5.26}$$

and

$$T^{(1\pi,\mathrm{IB})}_{S_1S_2}(\mathbf{n_1}-\mathbf{n_2}) = \frac{1}{L^3} \sum_{\mathbf{k}} \exp\left[i \frac{2\pi}{L} \mathbf{k} \cdot (\mathbf{n_1}-\mathbf{n_2}) \right] \times T^{(1\pi,\mathrm{IB})}_{S_1S_2}(\mathbf{k}) \tag{5.27}$$

with

$$\begin{aligned} T^{(1\pi,\mathrm{IB})}_{S_1S_2}(\mathbf{k}) = -\frac{g_\mathrm{A}^2}{4f_\pi^2} q_{S_1} q_{S_2} \left(\frac{1}{\mathbf{q}^2 + M^2_{\pi^\pm}} - \frac{1}{\mathbf{q}^2 + M^2_{\pi^0}} \right) \\ \times \exp\left[-b_\pi \mathbf{q}^2 \right] , \end{aligned} \tag{5.28}$$

where $\mathbf{q}$ equals to $\mathbf{k}$ multipled by $2\pi/L$. The first IB CTs apprear at $O(Q^3)$ which take the form as, following Ref. [15]

$$V_{\mathrm{pp}} = C_{3,\mathrm{pp}} O_{\mathrm{pp}} \tag{5.29}$$

$$O_{\mathrm{pp}} = \frac{1}{2} : \sum_{\mathbf{n}} \left[\frac{1}{2}\rho_{\mathrm{NL}}(\mathbf{n}) + \frac{1}{2}\rho_{I=3,\mathrm{NL}}(\mathbf{n}) \right] \left[\frac{1}{2}\rho_{\mathrm{NL}}(\mathbf{n}) + \frac{1}{2}\rho_{I=3,\mathrm{NL}}(\mathbf{n}) \right] : , \tag{5.30}$$

for isospin state pp and

$$V_{\mathrm{nn}} = C_{3,\mathrm{nn}} O_{\mathrm{nn}} \tag{5.31}$$

$$O_{\mathrm{nn}} = \frac{1}{2} : \sum_{\mathbf{n}} \left[\frac{1}{2}\rho_{\mathrm{NL}}(\mathbf{n}) - \frac{1}{2}\rho_{I=3,\mathrm{NL}}(\mathbf{n}) \right] \left[\frac{1}{2}\rho_{\mathrm{NL}}(\mathbf{n}) - \frac{1}{2}\rho_{I=3,\mathrm{NL}}(\mathbf{n}) \right] : . \tag{5.32}$$

for isospin state neutron-neutron. Due to the practical consideration that the empirical phase shifts for neutron-neutron scattering cannot be easily measured, we deal with $C_{3,\mathrm{nn}}$ approximately as $-C_{3,\mathrm{pp}}$ The left part can be attributed to Q^4 or higher order contributions, see Ref. [45], so that $V_{\mathrm{pp}} + V_{\mathrm{nn}} \to C_{3,\mathrm{pp}}(O_{\mathrm{pp}} - O_{\mathrm{nn}})$. We do not consider IB of TPEs so that the pion mass in TPE is simply taken as

charge-averaged, $M_\pi = 138.03$ MeV.

Our task in this section is to fit coefficients of subleading or higher order short-range interactions $\Delta V_{\text{ct},0}$, $V_{\text{ct},2}$, $V_{\text{ct},4}$ and V_{pp} by pp and np phase shifts.

5.2 Interactions on the Lattice: Coulomb Potential

In pp scattering process, Coulomb interaction between the electronic chargers, $V_{\text{coul}} = \alpha_{\text{EM}}/r$, should be included for the pp case with the fine structure constant taken as $1/137$. The singularity of Coulomb potential originated from the zero-range interaction is supposed to be carefully removed in our lattice simulation. A naïve convention is to take the zero-range Coulomb potential as zero, whereas other conventions are allowed for that it can be absorted by the CTs irrelative to momentum.

In this study, Coulomb effective potential is written as

$$V_{\text{coul}} = -\frac{\alpha_{\text{EM}}}{2} \sum_{\mathbf{n_1},\mathbf{n_2}} : \left[\frac{1}{2}\rho(\mathbf{n_1}) + \frac{1}{2}\rho_{I=3}(\mathbf{n_1})\right] \frac{1}{d(\mathbf{n_1} - \mathbf{n_2})} \left[\frac{1}{2}\rho(\mathbf{n_2}) + \frac{1}{2}\rho_{I=3}(\mathbf{n_2})\right] : , \tag{5.33}$$

where $d(\mathbf{n_1} - \mathbf{n_2})$ is the shortest length of $\mathbf{n_1} - \mathbf{n_2}$ as measured on the periodic lattice, and we define the value of d at the origin to be $1/2$. The notation $\rho_{I=3}$ refers to the $I = 3$ isospin component of the density operator with isospin ρ_I.

We measure phase shifts and mixing angles by fitting asymptotical behavior of the nucleonic wave functions. Spherical bessel functions are combined into wave functions in the non-interactive region for the case of np process, Eq. (3.152), because they are solutions of Helmholtz equation. Long-range Coulomb potential influences the motion of chargers no matter how much long their distance is. Thus we decompose the radial wave functions into the combination of solutions of Helmholtz equation with Coulomb potential, Ref. [15],

$$\psi(r) \cong A\, g_L^-(kr) - B\, g_L^+(kr) \tag{5.34}$$

where

$$g_L^\pm(kr) = -G_L \pm iF_L \tag{5.35}$$

with

$$\eta = \frac{\alpha_{\rm EM} m}{2k} \,, \tag{5.36}$$

$$F_L(\eta, kr) = (kr)^L e^{-ikr} c_L(\eta)\, {}_1F_1(L+1-i\eta, 2L+2, 2ikr) \,, \tag{5.37}$$

$$G_L(\eta, kr) = \frac{(2i)^{2L+1}\,(kr)^L e^{-ikr}\Gamma(L+1-i\eta)}{\Gamma(2L+2)c_L(\eta)} U(L+1-i\eta, 2L+2, 2ikr) + iF_L(\eta, kr) \,, \tag{5.38}$$

and

$$c_L(\eta) = \frac{2^L e^{-\pi\eta/2}\,|\Gamma(L+1+i\eta)|}{\Gamma(2L+2)} \,. \tag{5.39}$$

The function ${}_1F_1$ is Kummer's confluent hypergeometric function of the first kind, and the function U is Kummer's confluent hypergeometric function of the second kind.

Then a story similar in Sec. 3.4.2 goes, the coefficients A and B satisfy the relation $B = SA$ with S indicating the scattering matrix, $S = e^{2i\delta_L}$.

5.3 Neutron-Proton Scattering at N^{3}LO

Let us now present results for np scattering at N^{3}LO. From the TPE contributions we only consider the bubble diagrams with two dimension-three insertions and the two-loop diagram built from LO insertions. We need to include the D-waves in the fitting procedure now. The resulting LECs are shown in Tab. 5.1. The resulting phase shifts are shown in Fig. 5.1. As expected, we find an improvement in the description of most partial waves. However, a thorough error analysis along the lines of Ref. [37] should be done in the future.

5.4 Proton-Proton Scattering up to N^{3}LO

Next we consider pp scattering at N^{3}LO. Of course there are fewer partial waves in this case due to the Pauli principle. From the TPE contributions we only consider the bubble diagrams with two dimension-three insertions and the two-loop diagram built from LO insertions. Here we only consider the lowest partial waves where the Coulomb effect is most pronounced. The relevant LECs are shown in Tab. 5.2. The lowest partial waves for pp scattering are depicted in Fig. 5.2. Note that the Coulomb interaction only appears at NLO in our counting, therefore the LO description of the $^1S_0$ partial wave is far off the empirical result. Having said this, we observe a trend similar to the np case, namely the N^{3}LO description is the best. We notice again that this should be supplemented by a thorough error analysis.

Table 5.1: LECs for np scattering at NLO, N^2LO, and N^3LO. The values of LECs at LO, NLO, N^3LO, are given in units of $[10^{-4}\text{MeV}^{-2}]$, $[10^{-8}\text{MeV}^{-4}]$, $[10^{-12}\text{MeV}^{-6}]$, respectively.

	NLO	N^2LO	N^3LO
$\Delta C_{0,^1S_0}$	0.10919669	0.15273328	0.14984439
$\Delta C_{0,^3S_1}$	−.02922424	−.02853001	−.03099366
$C_{2,^1S_0}$	0.00199304	0.01022774	0.01106095
$C_{2,^3S_1}$	0.00104715	−.00156102	−.00145621
$C_{2,^3SD_1}$	−.05209445	−.07268494	−.06972326
$C_{2,^1P_1}$	0.20520544	0.23023119	0.21317679
$C_{2,^3P_0}$	0.00274363	0.01279163	0.01186457
$C_{2,^3P_1}$	0.16263367	0.17204053	0.17226589
$C_{2,^3P_2}$	0.04998091	0.06492118	0.07461369
$D_{4,^1S_0;1}$	–	–	−.00031571
$D_{4,^1S_0;2}$	–	–	0.00168885
$D_{4,^3S_1;1}$	–	–	−.00180739
$D_{4,^3S_1;2}$	–	–	−.00145621
$D_{4,^3SD_1;1}$	–	–	0.00607977
$D_{4,^3SD_1;2}$	–	–	−.03109305
$D_{4,^1P_1}$	–	–	−.00497417
$D_{4,^3P_0}$	–	–	−.00171225
$D_{4,^3P_1}$	–	–	−.00001781
$D_{4,^3P_2}$	–	–	0.00498841
$D_{4,^3PF_2}$	–	–	0.01999829
$D_{4,^1D_2}$	–	–	0.01203088
$D_{4,^3D_1}$	–	–	0.00050418
$D_{4,^3D_2}$	–	–	−.04000000
$D_{4,^3D_3}$	–	–	0.00250397

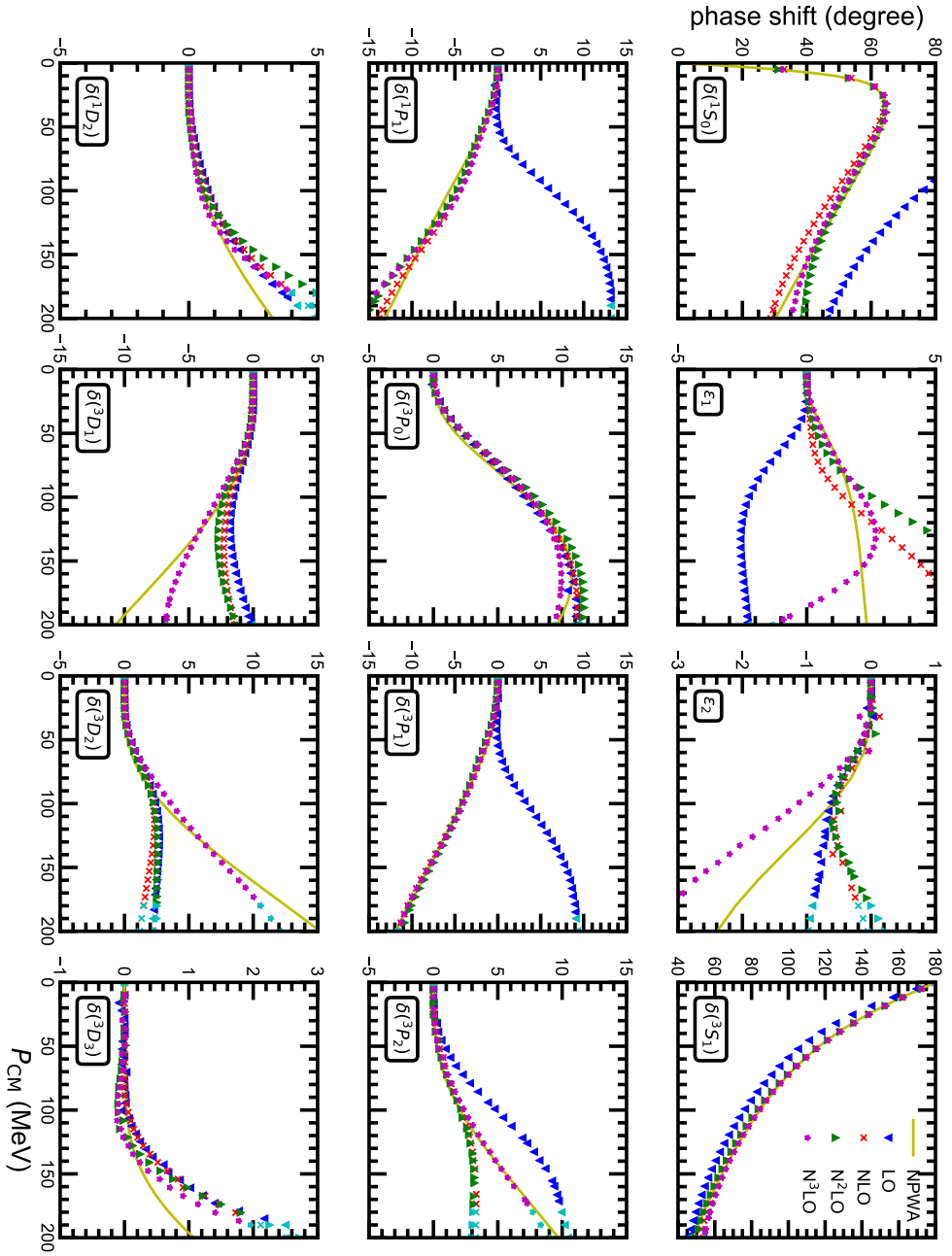

Figure 5.1: Phase shifts for np scattering at LO (downward blue triangles), NLO (red crosses), N^{2}LO (green triangles), N^{3}LO (magenta stars) as a function of CM momentum. The NPWA results are shown by the solid (yellow) curves.

Table 5.2: LECs for pp scattering at NLO, N^2LO, and N^3LO. The values of LECs at LO, NLO, N^3LO, are given in units of $[10^{-4}\text{MeV}^{-2}]$, $[10^{-8}\text{MeV}^{-4}]$, $[10^{-12}\text{MeV}^{-6}]$, respectively.

	NLO	N^2LO	N^3LO
$\Delta C_{0,^1S_0}$	0.11577718	0.15515046	0.14307987
$C_{2,^1S_0}$	0.00183307	0.00887531	0.01201563
$C_{2,^3P_0}$	−.00659107	0.01004595	0.01186403
$C_{2,^3P_1}$	0.15798787	0.17368014	0.16726571
$C_{2,^3P_2}$	0.04498001	0.05998001	0.06961663
$D_{4,^1S_0;1}$	–	–	−.00031474
$D_{4,^1S_0;2}$	–	–	0.00179488
$D_{4,^3P_0}$	–	–	0.00178983
$D_{4,^3P_1}$	–	–	−.00017810
$D_{4,^3P_2}$	–	–	0.00498864
$D_{4,^3PF_2}$	–	–	0.00999893
$D_{4,^1D_2}$	–	–	0.00250394

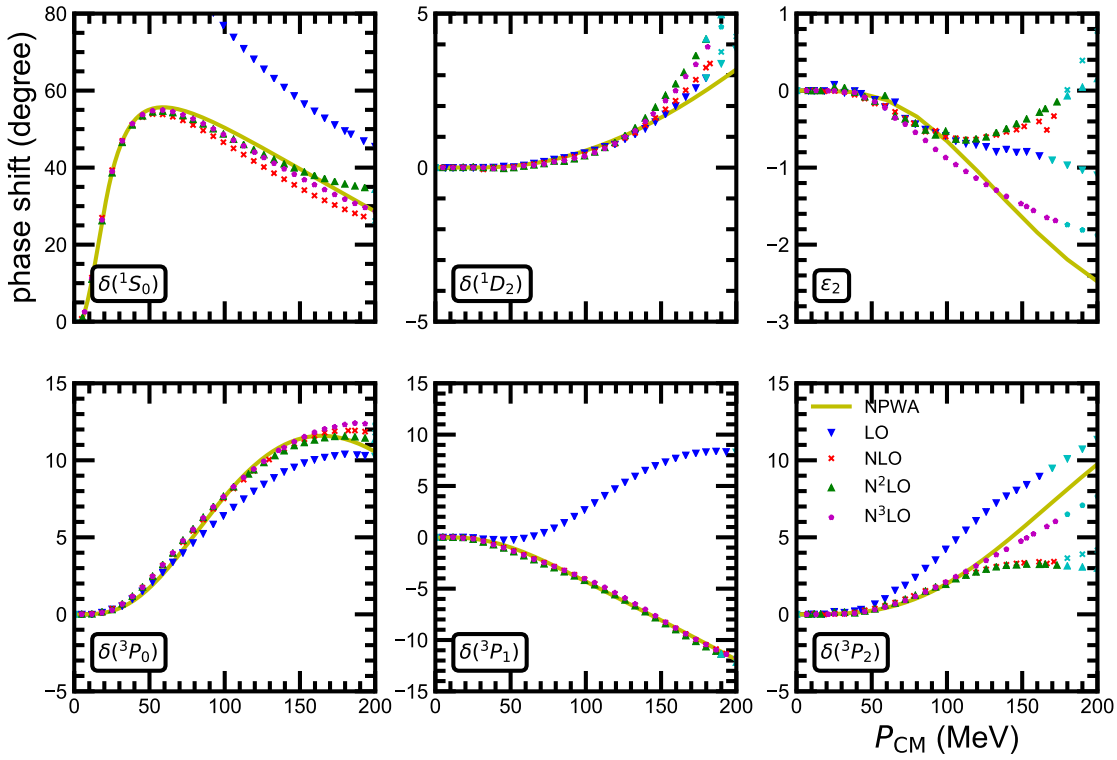

Figure 5.2: Phase shifts for the low partial waves of pp scattering at LO (downward blue triangles), NLO (red crosses), N^{2}LO (green triangles), N^{3}LO (magenta stars) as a function of CM momentum. The NPWA results are shown by the solid (yellow) curves.

CHAPTER 6

Nuclear Binding Near A Quantum Phase Transition

In this section[1] we discover an unexpected twist in the story of how nucleons self-assemble into nuclei. Lattice MC simulation results are presented using lattice interactions at LO in chiral effective field theory, together with Coulomb interactions between protons. In the lattice calculations discussed here we use a spatial lattice spacing of 1.97 fm and time lattice spacing of 1.32 fm. We are using natural units where the reduced Planck constant $\hbar$ and the speed of light c equal 1. We consider two different variants of the LO action, one with a new type of non-local smearing of the contact interactions. This was originally intended to suppress the remaining sign oscillations, but in fact leads to new insights about the nature of nuclear binding.

6.1 A Leading Order Action with Local and Nonlocal Contact Interactions

Our starting point is two lattice interactions A and B at LO in chiral effective field theory which are by design similar to each other and tuned to experimental low-energy nucleon-nucleon scattering phase shifts. The details of these interactions and scattering phase shifts are presented below, here we note

[1] The work of this chapter is based on the publication [43].

some important points. The interactions appear at LO in chiral effective field theory and consist of short-range interactions as well as the potential energy due to the exchange of a pion. As the short-range interactions are not truly point-like, they are actually what we call improved LO interactions. We write the nucleon-nucleon interactions as $V_{\rm A}(\mathbf{r}', \mathbf{r})$ and $V_{\rm B}(\mathbf{r}', \mathbf{r})$, where $\mathbf{r}$ is the spatial separation of the two incoming nucleons and $\mathbf{r}'$ is the spatial separation of the two outgoing nucleons. The short-range interactions in $V_{\rm A}(\mathbf{r}', \mathbf{r})$ consist of nonlocal (NL) terms, which means that $\mathbf{r}'$ and $\mathbf{r}$ are in general different. In contrast, the short-range interactions in $V_{\rm B}(\mathbf{r}', \mathbf{r})$ include nonlocal terms and also local terms where $\mathbf{r}'$ and $\mathbf{r}$ are fixed to be equal. The main difference between interactions A and B is the degree of locality of the short-range interactions. Another difference is that there are extra parameters contained in interaction B, and these are used to reproduce S-wave scattering for two alpha particles.

For our LO lattice calculations we use a spatial lattice spacing $a = (100 \text{ MeV})^{-1} = 1.97$ fm and time lattice step $a_t = (150 \text{ MeV})^{-1} = 1.32$ fm. Our axial-vector coupling constant is $g_{\rm A} = 1.29$ as derived from the GTR, the pion decay constant is $f_\pi = 92.2$ MeV, and the pion mass is $M_\pi = M_{\pi^0} = 134.98$ MeV. For the nucleon mass we use $m = 938.92$ MeV, and the electromagnetic fine structure constant is $\alpha_{\rm EM} = (137.04)^{-1}$. We do not consider any IB terms other than the Coulomb interaction in these LO calculations. We use σ_S with $S = 1, 2, 3$ for the Pauli matrices acting upon spin, and τ_I with $I = 1, 2, 3$ for the Pauli matrices acting upon isospin. We will use lattice units where the quantities are multiplied by the appropriate power of the spatial lattice spacing a to make the combination dimensionless. We write $\alpha_{\rm t}$ for the ratio $a_{\rm t}/a$. We use the notation $\sum_{\langle \mathbf{n}' \mathbf{n} \rangle}$ to denote the summation over nearest-neighbor lattice sites of $\mathbf{n}$. We write $\sum_{\langle \mathbf{n}' \mathbf{n} \rangle_i}$ to indicate the sum over nearest-neighbor lattice sites of $\mathbf{n}$ along the $i^{\rm th}$ spatial axis. Similarly, we define $\sum_{\langle\langle \mathbf{n}' \mathbf{n} \rangle\rangle_i}$ as the sum over next-to-nearest-neighbor lattice sites of $\mathbf{n}$ along the $i^{\rm th}$ axis and $\sum_{\langle\langle\langle \mathbf{n}' \mathbf{n} \rangle\rangle\rangle_i}$ as the sum over next-to-next-to-nearest-neighbor lattice sites of $\mathbf{n}$ along the $i^{\rm th}$ axis. Our lattice geometry is chosen to be an L^3 periodic lattice, and so the summations over $\mathbf{n}'$ are defined using periodic boundary conditions.

For each lattice site $\mathbf{n}$ on our lattice and real parameter $s_{\rm NL}$, we define nonlocal annihilation and creation operators for each spin and isospin component of the nucleon,

$$a_{\rm NL}(\mathbf{n}) = a(\mathbf{n}) + s_{\rm NL} \sum_{\langle \mathbf{n}' \mathbf{n} \rangle} a(\mathbf{n}') \,, \tag{6.1}$$

$$a^\dagger_{\rm NL}(\mathbf{n}) = a^\dagger(\mathbf{n}) + s_{\rm NL} \sum_{\langle \mathbf{n}' \mathbf{n} \rangle} a^\dagger(\mathbf{n}') \,. \tag{6.2}$$

For spin indices $S = 1, 2, 3$, and isospin indices $I = 1, 2, 3$, we define point-like densities,

$$\rho(\mathbf{n}) = a^\dagger(\mathbf{n})a(\mathbf{n}) \,, \tag{6.3}$$

$$\rho_S(\mathbf{n}) = a^\dagger(\mathbf{n})[\sigma_S]a(\mathbf{n}) \,, \tag{6.4}$$

$$\rho_I(\mathbf{n}) = a^\dagger(\mathbf{n})[\tau_I]a(\mathbf{n}) \,, \tag{6.5}$$

$$\rho_{S,I}(\mathbf{n}) = a^\dagger(\mathbf{n})[\sigma_S \otimes \tau_I]a(\mathbf{n}) \,. \tag{6.6}$$

For spin indices $S = 1, 2, 3$, and isospin indices $I = 1, 2, 3$, we also define smeared nonlocal densities,

$$\rho_{\rm NL}(\mathbf{n}) = a^\dagger_{\rm NL}(\mathbf{n})a_{\rm NL}(\mathbf{n}) \,, \tag{6.7}$$

$$\rho_{S,{\rm NL}}(\mathbf{n}) = a^\dagger_{\rm NL}(\mathbf{n})[\sigma_S]a_{\rm NL}(\mathbf{n}) \,, \tag{6.8}$$

$$\rho_{I,{\rm NL}}(\mathbf{n}) = a^\dagger_{\rm NL}(\mathbf{n})[\tau_I]a_{\rm NL}(\mathbf{n}) \,, \tag{6.9}$$

$$\rho_{S,I,{\rm NL}}(\mathbf{n}) = a^\dagger_{\rm NL}(\mathbf{n})[\sigma_S \otimes \tau_I]a_{\rm NL}(\mathbf{n}) \,, \tag{6.10}$$

and smeared local densities for real parameter $s_{\rm L}$,

$$\rho_{\rm L}(\mathbf{n}) = a^\dagger(\mathbf{n})a(\mathbf{n}) + s_{\rm L} \sum_{\langle \mathbf{n}' \mathbf{n} \rangle} a^\dagger(\mathbf{n}')a(\mathbf{n}') \,, \tag{6.11}$$

$$\rho_{S,{\rm L}}(\mathbf{n}) = a^\dagger(\mathbf{n})[\sigma_S]a(\mathbf{n}) + s_{\rm L} \sum_{\langle \mathbf{n}' \mathbf{n} \rangle} a^\dagger(\mathbf{n}')[\sigma_S]a(\mathbf{n}') \,, \tag{6.12}$$

$$\rho_{I,{\rm L}}(\mathbf{n}) = a^\dagger(\mathbf{n})[\tau_I]a(\mathbf{n}) + s_{\rm L} \sum_{\langle \mathbf{n}' \mathbf{n} \rangle} a^\dagger(\mathbf{n}')[\tau_I]a(\mathbf{n}') \,, \tag{6.13}$$

$$\rho_{S,I,{\rm L}}(\mathbf{n}) = a^\dagger(\mathbf{n})[\sigma_S \otimes \tau_I]a(\mathbf{n}) + s_{\rm L} \sum_{\langle \mathbf{n}' \mathbf{n} \rangle} a^\dagger(\mathbf{n}')[\sigma_S \otimes \tau_I]a(\mathbf{n}') \,. \tag{6.14}$$

The nonlocal short-range interactions are written as

$$V_{\rm NL} = \frac{c_{\rm NL}}{2} \sum_{\mathbf{n}} : \rho_{\rm NL}(\mathbf{n})\rho_{\rm NL}(\mathbf{n}) : + \frac{c_{\rm I,NL}}{2} \sum_{\mathbf{n},I} : \rho_{I,{\rm NL}}(\mathbf{n})\rho_{I,{\rm NL}}(\mathbf{n}) : \,, \tag{6.15}$$

while the local short-range interactions are

$$V_{\rm L} = \frac{c_{\rm L}}{2} \sum_{\mathbf{n}} :\rho_{\rm L}(\mathbf{n})\rho_{\rm L}(\mathbf{n}): + \frac{c_{\rm S,L}}{2} \sum_{\mathbf{n},S} :\rho_{S,{\rm L}}(\mathbf{n})\rho_{S,{\rm L}}(\mathbf{n}): + \frac{c_{\rm I,L}}{2} \sum_{\mathbf{n},I} :\rho_{I,{\rm L}}(\mathbf{n})\rho_{I,{\rm L}}(\mathbf{n}): + \frac{c_{\rm SI,L}}{2} \sum_{\mathbf{n},S,I} :\rho_{S,I,{\rm L}}(\mathbf{n})\rho_{S,I,{\rm L}}(\mathbf{n}): \ . \tag{6.16}$$

The :: symbol indicates normal ordering, where the annihilation operators are on the right-hand side and the creation operators are on the left-hand side. As described in previous work, Ref. [15], we take special combinations of the four local short-range operator coefficients so that the interaction in odd partial waves vanish completely. For our work here, we also make the strength of the local short-range interactions equal in the two S-wave channels. As a result, we have only one independent coefficient, $c_{\rm S,L} = c_{\rm I,L} = c_{\rm SI,L} = -\frac{1}{3}c_{\rm L}$. In future work it may be useful to consider relaxing this condition.

The OPE interaction has the form

$$V_{\rm OPE} = -\frac{g_{\rm A}^2}{8f_\pi^2} \sum_{\mathbf{n}',\mathbf{n},S',S,I} :\rho_{S',I}(\mathbf{n}')f_{S'S}(\mathbf{n}'-\mathbf{n})\rho_{S,I}(\mathbf{n}): , \tag{6.17}$$

where $f_{S'S}$ is defined as

$$f_{S'S}(\mathbf{n}'-\mathbf{n}) = \frac{1}{L^3}\sum_{\mathbf{q}} \frac{\exp[-i\mathbf{q}\cdot(\mathbf{n}'-\mathbf{n}) - b_\pi \mathbf{q}^2] q_{S'} q_S}{\mathbf{q}^2 + M_\pi^2} , \tag{6.18}$$

and each lattice momentum component q_S is an integer multiplied by $2\pi/L$. The parameter b_π is included to remove short-distance lattice artifacts in the OPE interaction. It results in better preservation of rotational symmetry and will be especially useful at smaller lattice spacings, Ref. [27].

We use a free lattice Hamiltonian, Ref. [15], of the form,

$$H_{\rm free} = \frac{49}{12m}\sum_{\mathbf{n}} a^\dagger(\mathbf{n})a(\mathbf{n}) - \frac{3}{4m}\sum_{\mathbf{n},i}\sum_{\langle \mathbf{n}'\,\mathbf{n}\rangle_i} a^\dagger(\mathbf{n}')a(\mathbf{n}) + \frac{3}{40m}\sum_{\mathbf{n},i}\sum_{\langle\langle \mathbf{n}'\,\mathbf{n}\rangle\rangle_i} a^\dagger(\mathbf{n}')a(\mathbf{n}) - \frac{1}{180m}\sum_{\mathbf{n},i}\sum_{\langle\langle\langle \mathbf{n}'\,\mathbf{n}\rangle\rangle\rangle_i} a^\dagger(\mathbf{n}')a(\mathbf{n}) . \tag{6.19}$$

For interaction A at LO, the lattice Hamiltonian is

$$H_{\rm A} = H_{\rm free} + V_{\rm NL} + V_{\rm OPE} , \tag{6.20}$$

with $s_{\rm NL} = 0.07700$, $c_{\rm NL} = -0.2268$, $c_{\rm I,NL} = 0.02184$, and $b_\pi = 0.7000$. These parameters are determined by fitting to the low-energy nucleon-nucleon phase shifts and the observed deuteron energy. For the corresponding LO + Coulomb interactions, we simply add $V_{\rm Coulomb}$ to $H_{\rm A}$.

For interaction B at LO, we have

$$H_{\rm B} = H_{\rm free} + V_{\rm NL} + V_{\rm L} + V_{\rm OPE} \,, \tag{6.21}$$

with $s_{\rm NL} = 0.07700$, $s_{\rm L} = 0.8100$, $c_{\rm NL} = -0.1171$, $c_{\rm I,NL} = 0.02607$, $c_{\rm L} = -0.01013$, and $b_\pi = 0.7000$. For the corresponding LO + Coulomb interactions, we simply add $V_{\rm Coulomb}$ to $H_{\rm B}$. These parameters are determined by fitting to the low-energy nucleon-nucleon phase shifts, the observed deuteron energy, and the low-energy alpha-alpha S-wave phase shifts.

6.2 Neutron-Proton Scattering

In Fig. 6.1 we show the LO lattice phase shifts for proton-neutron scattering versus the center-of-mass relative momentum for interactions A (red triangles) and B (blue squares). For comparison we also plot the phase shifts extracted from the Nijmegen PWA [40] (black lines) and a continuum version of interaction A (green dashed lines). In the first row, the data in panels **a**,**b**,**c**,**d** correspond to ${}^1{\rm S}_0, {}^3{\rm S}_1, {}^1{\rm P}_1, {}^3{\rm P}_0$ respectively. In the second row, panels **e**,**f**, **g**,**h** correspond to ${}^3{\rm P}_1, {}^3{\rm P}_2, {}^1{\rm D}_2, {}^3{\rm D}_1$ respectively. In the third row, panels **i**, **j**,**k**,**l** correspond to ${}^3{\rm D}_2, {}^3{\rm D}_3, \varepsilon_1, \varepsilon_2$ respectively. The level of agreement with the experimental phase shifts for interactions A and B is typical for LO chiral effective field theory at our cutoff momentum of $\pi/a \approx 314$ MeV. The agreement would be somewhat better if we were to use a smaller value of the smearing parameter b_π in the OPE potential. However, we prefer the higher value of b_π to reduce sign oscillations in the MC lattice simulations. The LO interactions are more than sufficient to illustrate the ideas of this work but not sufficient for precision calculations. For precision calculations, this would be just the first step in the chiral effective field theory expansion, and the phase shifts would be systematically improved at each higher order, NLO, N^{2}LO, and so on. We note the good agreement between the continuum results in green dashed lines and lattice interaction A results. This is a good indication that we have successfully reduced lattice artifacts from the calculations and was part of the motivation for introducing the parameter b_π. The nonlocal smeared interaction $V_{\rm NL}$ makes a non-negligible contribution to the S-wave interactions only. Furthermore, the local smeared interaction $V_{\rm L}$ makes a nonzero contribution to only the even partial waves (S, D, $\cdots$). Hence the interactions A and

Figure 6.1: Nucleon-nucleon scattering phase shifts. We plot LO lattice phase shifts for proton-neutron scattering versus the center-of-mass relative momentum for interactions A (red triangles) and B (blue squares). For comparison we also plot the phase shifts extracted from the Nijmegen PWA, Ref. [40] (black lines) and a continuum version of interaction A (green dashed lines). In the first row, the data in panels **a**, **b**,**c**,**d** correspond to $^1S_0$, $^3S_1$, $^1P_1$, $^3P_0$ respectively. In the second row, panels **e**,**f**,**g**,**h** correspond to $^3P_1$, $^3P_2$, $^1D_2$, $^3D_1$ respectively. In the third row, panels **i**, **j**,**k**,**l** correspond to $^3D_2$, $^3D_3$, ε_1, ε_2 respectively.

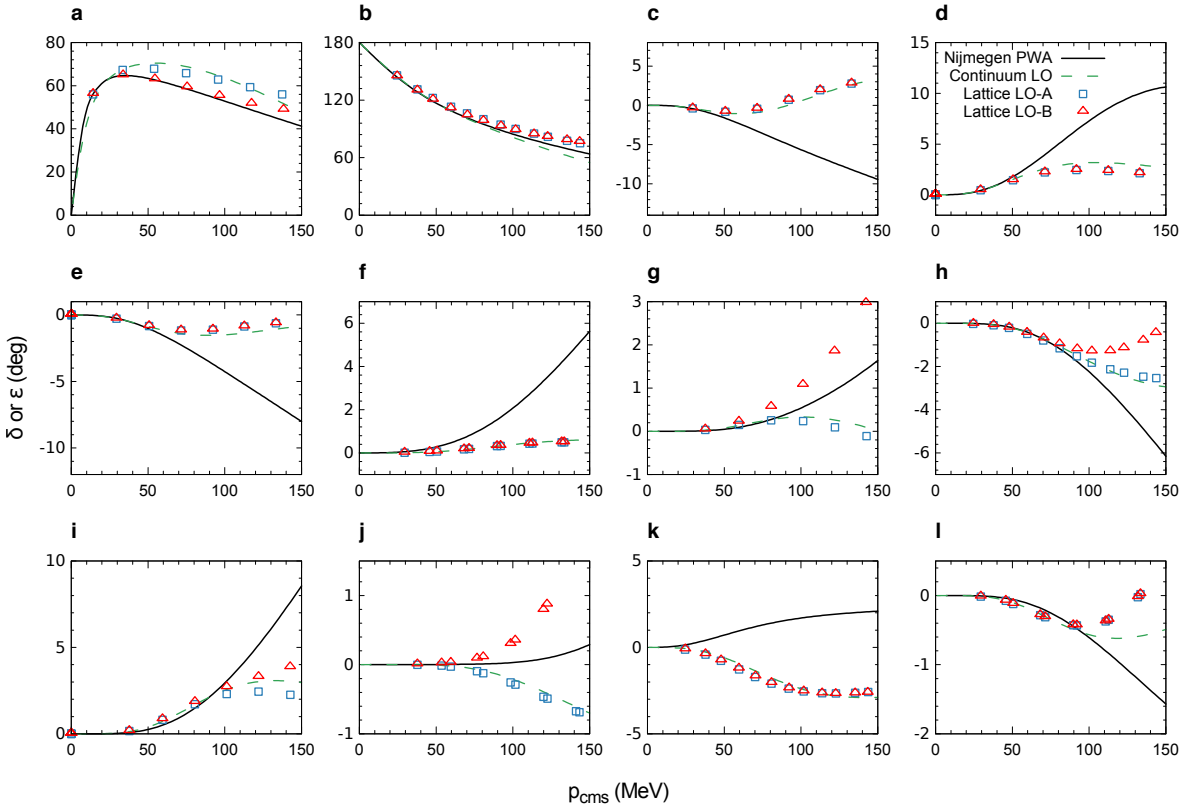

B are exactly the same in all odd partial waves. We see that the S-wave interactions for interactions A and B are also quite similar, though the $^1S_0$ partial wave scattering is somewhat more attractive for interaction A. On the other hand, the D-wave partial waves are more attractive for interaction B.

6.3 Ground State Engergies of Nuclei

Based on these LO interactions, we know calculate the ground state energies of various nuclei, in particluar alpha-cluster type ones. This will lead to somesurprising findings.

We let $a^\dagger_{\uparrow,p}(\mathbf{n})$, $a^\dagger_{\downarrow,p}(\mathbf{n})$, $a^\dagger_{\uparrow,n}(\mathbf{n})$, and $a^\dagger_{\downarrow,n}(\mathbf{n})$ be the creation operators for a spin-up proton, spin-down

proton, spin-up neutron, and spin-down neutron. We write $\tilde{a}^\dagger_{\uparrow,p}(0)$, $\tilde{a}^\dagger_{\downarrow,p}(0)$, $\tilde{a}^\dagger_{\uparrow,n}(0)$, and $\tilde{a}^\dagger_{\downarrow,n}(0)$ for the corresponding zero-momentum creation operators. We also write $\prod \tilde{a}^\dagger$ as shorthand for the product

$$\prod \tilde{a}^\dagger = \tilde{a}^\dagger_{\uparrow,p}(0)\tilde{a}^\dagger_{\downarrow,p}(0), \tilde{a}^\dagger_{\uparrow,n}(0)\tilde{a}^\dagger_{\downarrow,n}(0) \,. \tag{6.22}$$

For the ground state energy calculations of ^{3}H and ^{3}He we use a lattice volume of (16 fm)^3. The initial states we choose are

$$|\Psi_i^{^3\mathrm{H}}\rangle = \sum_{\mathbf{n},\mathbf{n}',\mathbf{n}'',\mathbf{n}'''} e^{-\alpha|\mathbf{n}-\mathbf{n}'|} e^{-\alpha|\mathbf{n}-\mathbf{n}''|} e^{-\alpha|\mathbf{n}-\mathbf{n}'''|} a^\dagger_{\uparrow,p}(\mathbf{n}') a^\dagger_{\uparrow,n}(\mathbf{n}'') a^\dagger_{\downarrow,n}(\mathbf{n}''') |0\rangle \,, \tag{6.23}$$

$$|\Psi_i^{^3\mathrm{He}}\rangle = \sum_{\mathbf{n},\mathbf{n}',\mathbf{n}'',\mathbf{n}'''} e^{-\alpha|\mathbf{n}-\mathbf{n}'|} e^{-\alpha|\mathbf{n}-\mathbf{n}''|} e^{-\alpha|\mathbf{n}-\mathbf{n}'''|} a^\dagger_{\uparrow,n}(\mathbf{n}') a^\dagger_{\uparrow,p}(\mathbf{n}'') a^\dagger_{\downarrow,p}(\mathbf{n}''') |0\rangle \,, \tag{6.24}$$

with $\alpha = 2$ in lattice units. In panel **a** of Fig. 6.2 we show the energy versus projection time $t = L_t a_t$ for ^{3}He for the LO interaction A (blue plus signs and dashed lines), LO interaction B (red squares and dashed lines), LO + Coulomb interaction A (blue crosses and solid lines), and LO + Coulomb interaction B (red triangles and solid lines). As we are not including IB effects other than Coulomb interactions, the LO and LO + Coulomb results for ^{3}H are exactly the same as the LO results for ^{3}He. The error bars indicate one standard deviation errors due to the stochastic noise of the MC simulations. The lines are extrapolations to infinite projection time using the ansatz,

$$E(t) = E_0 + c \exp[-\Delta E\, t] \,, \tag{6.25}$$

where E_0 is the ground state energy that we wish to determine. The results for the ground state energies are shown in Table 6.1. For the ground state energy calculations of ^{4}He we use a lattice volume of (12 fm)^3. The initial state we choose is

$$|\Psi_i^{^4\mathrm{He}}\rangle = \prod \tilde{a}^\dagger |0\rangle \,. \tag{6.26}$$

In panel **b** of Fig. 6.2 we show the energy versus projection time $t = L_t a_t$ for ^{4}He for the LO interaction A (blue plus signs and dashed lines), LO interaction B (red squares and dashed lines), LO + Coulomb interaction A (blue crosses and solid lines), and LO + Coulomb interaction B (red triangles and solid lines). The error bars indicate one standard deviation errors of the MC simulations, and the lines are extrapolations to infinite projection time using the ansatz in Eq. (6.25). The results for the ground state

Figure 6.2: Energy versus projection time for ^{3}H,^{3}He, and ^{4}He. In panels **a** and **b** we plot the energy versus projection time $t = L_t a_t$ for ^{3}He and ^{4}He respectively for the LO interaction A (blue plus signs and dashed lines), LO interaction B (red squares and dashed lines), LO + Coulomb interaction A (blue crosses and solid lines), and LO + Coulomb interaction B (red triangles and solid lines). The LO and LO + Coulomb results ^{3}H are the same as the LO results for ^{3}He. The error bars indicate one standard deviation errors from the stochastic noise of the MC simulations, and the lines show extrapolations to infinite projection time.

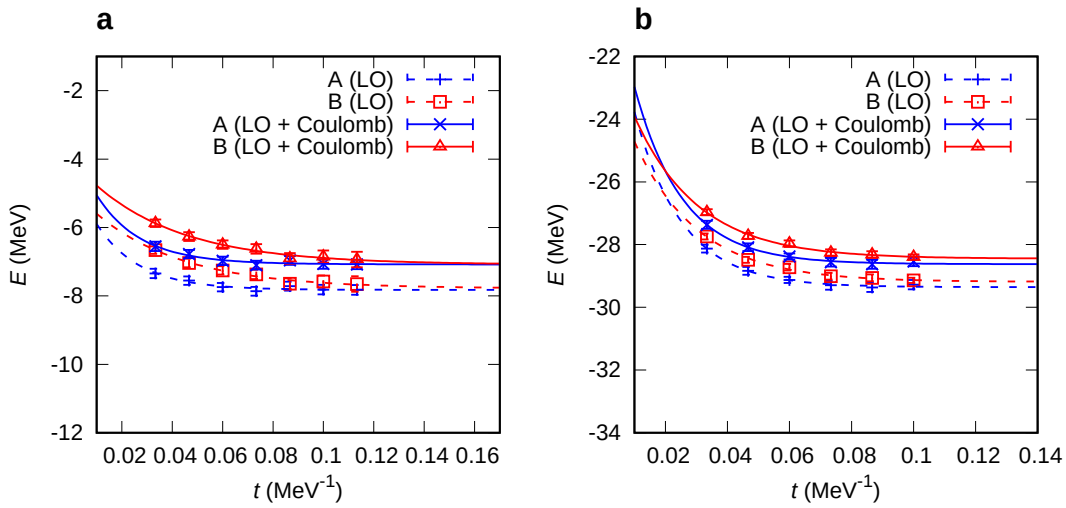

energies are shown in Table 6.1.

We note that while that the ^{3}H energies for interactions A and B are underbound, the energies for ^{4}He are near the physical value. This may seem puzzling since in continuum-space calculations there is a well-known universal correlation between the ^{3}H and ^{4}He energies called the Tjon line, Refs. [46–48]. Our lattice results show some deviation from this universal behavior due to lattice artifacts associated with our lattice spacing of 1.97 fm. This is not a new observation. The same behavior has been analyzed previously at the same lattice spacing but with a different lattice interaction, Refs. [15, 49]. In order to match the physical ^{3}H and ^{4}He energies at the same time, higher-order short-range 3N interactions at N^{4}LO and possibly the LO short-range four-nucleon interaction at N^{5}LO are needed. However a much simpler solution is to use a smaller lattice spacing, as these lattice deviations from the continuum-space Tjon line decrease very rapidly with the lattice spacing.

For the ground state energy calculations of ^{8}Be, ^{12}C, ^{16}O, and ^{20}Ne we use a lattice volume of (12 fm)^3.

The initial states we use are

$$|\Psi_i^{^8\mathrm{Be}}\rangle = \prod \tilde{a}^\dagger \cdot M_* \prod \tilde{a}^\dagger |0\rangle \ , \tag{6.27}$$

$$|\Psi_i^{^{12}\mathrm{C}}\rangle = \prod \tilde{a}^\dagger \cdot M_* \prod \tilde{a}^\dagger \cdot M_* \prod \tilde{a}^\dagger |0\rangle \ , \tag{6.28}$$

$$|\Psi_i^{^{16}\mathrm{O}}\rangle = \prod \tilde{a}^\dagger \cdot M_* \prod \tilde{a}^\dagger \cdot M_* \prod \tilde{a}^\dagger \cdot M_* \prod \tilde{a}^\dagger |0\rangle \ , \tag{6.29}$$

$$|\Psi_i^{^{20}\mathrm{Ne}}\rangle = \prod \tilde{a}^\dagger \cdot M_* \prod \tilde{a}^\dagger \cdot M_* \prod \tilde{a}^\dagger \cdot M_* \prod \tilde{a}^\dagger \cdot M_* \prod \tilde{a}^\dagger |0\rangle \ . \tag{6.30}$$

The interspersing of the transfer matrix M_* in between the products of creation operators allows us to create all nucleons with zero momentum without violating the Pauli exclusion principle. In panels **a**, **b**, **c**, **d** of Fig. 6.3 we show the energy versus projection time $t = L_t a_t$ for ^{8}Be, ^{12}C, ^{16}O, and ^{20}Ne respectively for the LO interaction A (blue plus signs and dashed lines), LO interaction B (red squares and dashed lines), LO + Coulomb interaction A (blue crosses and solid lines), and LO + Coulomb interaction B (red triangles and solid lines). The error bars indicate one standard deviation errors from the stochastic noise of the MC simulations, and the lines are extrapolations to infinite projection time using the ansatz in Eq. (6.25). The results for the ground state energies are shown in Table 6.1. The LO + Coulomb results for interaction B are in good agreement with experimental results, better overall than the N^{2}LO results in Ref. [41]. However, there is significant underbinding for interaction A with increasing nucleon number. For interaction A, it is illuminating to compute the ratio of the LO energy for each of the alpha-like nuclei to that of the alpha particle. For ^{8}Be the ratio is 1.997(6), for ^{12}C the ratio is 3.00(1), for ^{16}O it is 4.00(2), and for ^{20}Ne we have 5.03(3). These simple integer ratios indicate that the ground state for interaction A in each case is a weakly-interacting Bose gas of alpha particles. This interpretation is also confirmed by calculations of NN spatial correlations and local four-nucleon correlations.

To understand how interactions A and B can produce such completely different physics, we consider their alpha-alpha S-wave phase shifts. While interaction fails at describing these phase shifts, this is different for interaction B. In fact, Interaction B was tuned to the nucleon-nucleon phase shifts and the alpha-alpha S-wave phase shifts, and so the agreement with experimental data is very good. This difference in the description of the alpha-alpha S-wave phase shifts explains the large differences between interactions A and B for the energies of the larger alpha-like nuclei.

For both interactions A and B, the auxiliary-field MC simulations presented here have far milder MC sign cancellations than in previous lattice simulations of the same systems, Ref. [41]. This very promising development will allow for much larger and previously difficult simulations in the future. The

Figure 6.3: Energy versus projection time for ^{8}Be,^{12}C,^{16}O, and ^{20}Ne. In panels **a**,**b**,**c**,**d** we plot the energy versus projection time $t = L_t a_t$ for ^{8}Be, ^{12}C, ^{16}O, and ^{20}Ne respectively for the LO interaction A (blue plus signs and dashed lines), LO interaction B (red squares and dashed lines), LO + Coulomb interaction A (blue crosses and solid lines), and LO + Coulomb interaction B (red triangles and solid lines). The error bars indicate one standard deviation errors from the stochastic noise of the MC simulations, and the lines show extrapolations to infinite projection time.

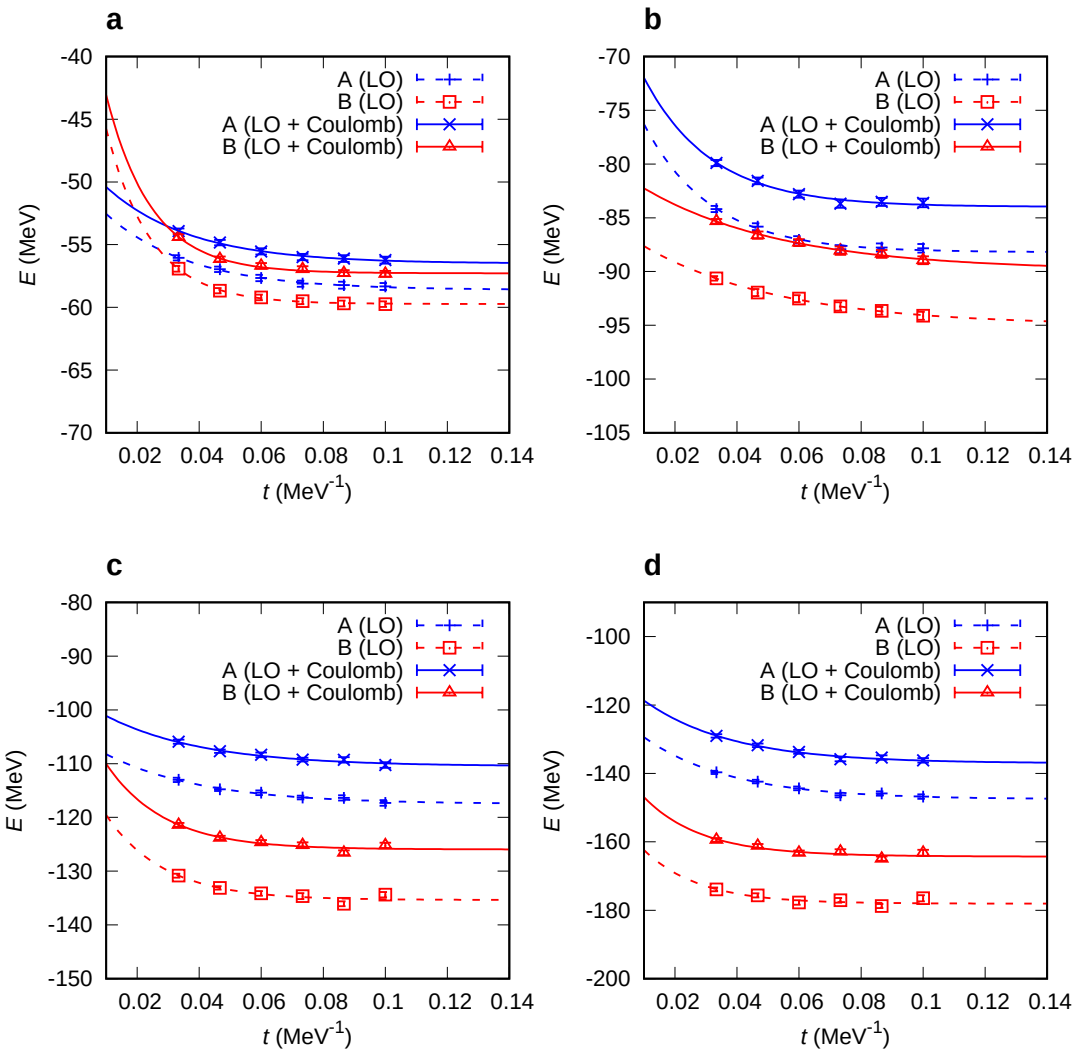

savings come from two innovations. The first is the introduction of the nonlocal interactions in $V_{\rm NL}$. Ironically, the implementation of general nonlocal interactions in quantum MC simulations have long been problematic due to sign oscillations. However, the auxiliary-field implementation of the interactions in $V_{\rm NL}$ are extremely favorable from the point of view of sign oscillations. The reason for this is the very simple structure of the terms in $V_{\rm NL}$. This leads to fewer issues with so-called interference sign problems as discussed in Ref. [50]. The other innovation reducing the sign problem is the introduction

of the parameter b_π in the OPE interaction. This decreases the short-distance repulsion in the S-wave channels responsible for some sign oscillations.

What we have discovered is that alpha-alpha scattering is very sensitive to the degree of locality of the nucleon-nucleon lattice interactions. It can be shown that this dependence on the degree of locality is due to the compactness of the alpha-particle wave function. In contrast, the nucleon-nucleon scattering phase shifts make no constraint on the degree of locality of the nucleon-nucleon interactions. For example, if one starts with a purely local interaction, a unitary transformation can be used to define a new interaction which is highly nonlocal but having exactly the same phase shifts. The differences only become apparent in systems with more than two nucleons and can be understood as arising from three-body and higher-body interactions. Interaction A is a perfectly valid starting point for describing nucleon-nucleon interactions. However, substantial higher-nucleon interactions will be needed to rectify the missing strength of the alpha-alpha interactions and the additional binding energy in nuclei. These resultssuggests a strategy for improving future *ab initio* nuclear structure and reaction calculations by incorporating low-energy light-nucleus scattering data in addition to nucleon-nucleon scattering data.

6.4 Ground State Energies as A Function of λ

To further elucidate the physics behind this different LO interaction, let us consider the one-parameter family of interactions, $V_\lambda = (1-\lambda)V_\mathrm{A} + \lambda V_\mathrm{B}$ with the Coulomb interactions switched off. While the properties of the two, three, and four nucleon systems vary only slightly with λ, the many-body ground state of V_λ undergoes a quantum phase transition from a Bose-condensed gas to a nuclear liquid. This phase transition occurs when the alpha-alpha S-wave scattering length $a_{\alpha\alpha}$ crosses zero, and the Bose gas collapses due to the attractive interactions. At slightly larger λ, finite alpha-like nuclei also become bound, starting with the largest nuclei first. The last alpha-like nucleus to be bound is ^{8}Be at the so-called unitarity point where $|a_{\alpha\alpha}| = \infty$. Empirically we find that the quantum phase transition occurs at the point $\lambda_\infty = 0.0(1)$. The uncertainty of ± 0.1 is due to the energy levels having a slow dependence on λ near $\lambda = 0.0$. Since any V_λ represents a seemingly reasonable starting point for the effective field theory at LO, one may end up crossing the phase transition when considering higher-order effects beyond LO. It is in this sense that we say nature is near a quantum phase transition.

Let us study this phase transition in more detail At the phase transition point the alpha clusters become non-interacting in the dilute limit, and so we should find the following simple relationship among the

ground state energies provided that the finite volume is sufficiently large:

$$E_{^4\mathrm{He}} = 1/2\ E_{^8\mathrm{Be}} = 1/3\ E_{^{12}\mathrm{C}} = 1/4\ E_{^{16}\mathrm{O}} = 1/5\ E_{^{20}\mathrm{Ne}}\ . \tag{6.31}$$

In Fig. 6.4 we plot the LO ground state energies $E_{^4\mathrm{He}}$, $1/2\ E_{^8\mathrm{Be}}$, $1/3\ E_{^{12}\mathrm{C}}$, $1/4\ E_{^{16}\mathrm{O}}$, $1/5\ E_{^{20}\mathrm{Ne}}$ versus λ. We see that the phase transition occurs at $\lambda_\infty = 0.0(1)$.

Figure 6.4: Ground state energies versus λ. We plot the LO ground state energies $E_{^4\mathrm{He}}$, $1/2\ E_{^8\mathrm{Be}}$, $1/3\ E_{^{12}\mathrm{C}}$, $1/4\ E_{^{16}\mathrm{O}}$, $1/5\ E_{^{20}\mathrm{Ne}}$ versus the parameter λ which interpolates between V_A and V_B.

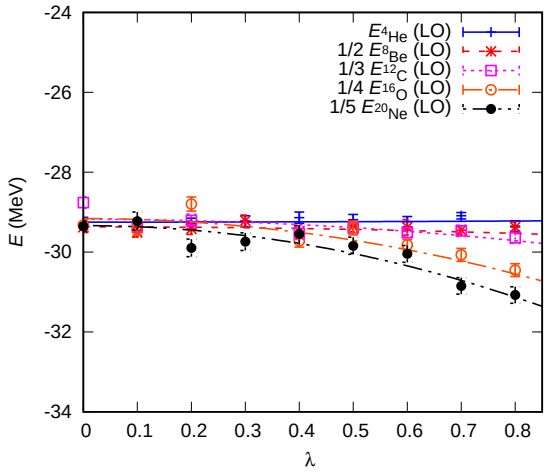

To determine the critical point λ_{20} when ^{20}Ne becomes bound, we compare $E_{^{20}\mathrm{Ne}}$ with the threshold energy $E_{^{16}\mathrm{O}} + E_{^4\mathrm{He}}$. For this analysis we also include the finite-volume energy one obtains at infinite S-wave scattering length for the ^{16}O + ^{4}He system. At infinite scattering length the energy of any two-body system with reduced mass μ in a periodic box of size L is, Ref. [51, 52]

$$\Delta E = \frac{4\pi^2 d_1}{mL^2}\ , \tag{6.32}$$

where

$$d_1 \approx -0.095901\ . \tag{6.33}$$

We find that the critical point for the binding of ^{20}Ne is $\lambda_{20} = 0.2(1)$. A similar analysis for the binding of the other alpha nuclei finds $\lambda_{16} = 0.2(1)$ for ^{16}O, $\lambda_{12} = 0.3(1)$ for ^{12}C, and $\lambda_8 = 0.7(1)$ for ^{8}Be. One finds a sudden change in the nucleon-nucleon density correlations at long distances as λ crosses the critical point, going from a continuum state to a self-bound system. As λ increases further beyond this

Table 6.1: Ground state energies of ^{3}H, ^{3}He, ^{4}He, ^{8}Be, ^{12}C, ^{16}O, ^{20}Ne for interactions A and B. We show LO results, LO + Coulomb results, and experimental data. All energies are in units of MeV. The error bars denote one standard deviation errors.

Nucleus	A (LO)	B (LO)	A (LO + Coulomb)	B (LO + Coulomb)	Experiment
^{3}H	−7.82(5)	−7.78(12)	−7.82(5)	−7.78(12)	−8.482
^{3}He	−7.82(5)	−7.78(12)	−7.08(5)	−7.09(12)	−7.718
^{4}He	−29.36(4)	−29.19(6)	−28.62(4)	−28.45(6)	−28.296
^{8}Be	−58.61(14)	−59.73(6)	−56.51(14)	−57.29(7)	−56.591
^{12}C	−88.2(3)	−95.0(5)	−84.0(3)	−89.9(5)	−92.162
^{16}O	−117.5(6)	−135.4(7)	−110.5(6)	−126.0(7)	−127.619
^{20}Ne	−148(1)	−178(1)	−137(1)	−164(1)	−160.645

critical value, the nucleus becomes more tightly bound, gradually losing its alpha cluster substructure and becoming more like a nuclear liquid droplet. The quantum phase transition at $\lambda_\infty = 0.0(1)$ is the corresponding phenomenon in the many-body system, a first-order phase transition occurring for infinite matter.

CHAPTER 7

Summary

In this thesis we first presented a systematic study of neutron-proton scattering up to N^{2}LO in the scheme of NLEFT in Sec. 4. We obtained the corresponding LECs that parametrize the short-distance interaction by fitting phase shifts and mixing angles. Previous works at a coarse lattice spacing $a \simeq 2\,\text{fm}$, see Refs. [13, 14], had shown good agreement with empirical data at momenta up to the pion mass. Here, the full TPE was included in order to improve the trends of phase shifts at high momenta. Also, we could lower the lattice spacing to $a \simeq 1\,\text{fm}$, which requires the full inclusion of the TPE, whereas for coarse lattices its contribution can be absorbed into the LECs of the four-nucleon terms. Quantitative uncertainties of the fitted LECs were estimated by a statistical analysis, and a technical discussion about systematical errors was given. Deviations of the phase shifts from data originate from the uncertainties of LECs and loss of contributions of high order interactions. We showed that the former dominates at low momenta while the latter dominates at high momenta and is therefore treated as systematic errors. Effects of finite lattice spacings were scrutinized in the range of $1 - 2$ fm and it was found that a coarse lattice has slight impact on the phase shifts either at low momenta (less than 100 MeV) or at low partial waves (S-waves), whereas a fine lattice can improve the scattering behavior in the opposite situation. We have also presented a comparison of fully non-perturbative N^{2}LO calculations with a perturbative treatment of contributions beyond LO for pratical reasons, such as sign oscillation problems and increasing computational complexity in MC simulation on many-body system. It can be stated that the physics of the two-nucleon system (nucleon-nucleon scattering and the deuteron) is independent

of the lattice spacing for momenta below the pion mass. This can be made more precise at N^{3}LO. In Sec. 5, we presented first results at this order based on the improved, though incomplete, TPE and the contribution from the new contact interactions. We also included the Coulomb force in the proton-proton system. As expected, these corrections improve the description of the data, though a thorough error estimation still has to be performed.

In Sec. 6 we presented numerical evidence from *ab initio* lattice simulations showing that nature is near a quantum phase transition, a zero-temperature transition driven by quantum fluctuations. Using lattice effective field theory, we perform MC simulations for systems with up to twenty nucleons. For even and equal numbers of protons and neutrons, we discover a first-order transition at zero temperature from a Bose-condensed gas of alpha particles (^{4}He nuclei) to a nuclear liquid. Whether one has an alpha-particle gas or nuclear liquid is determined by the strength of the alpha-alpha interactions, and we show that the alpha-alpha interactions depend on the strength and locality of the nucleon-nucleon interactions. This insight should be useful in improving calculations of nuclear structure and important astrophysical reactions involving alpha capture on nuclei. Our findings also provide a tool to probe the structure of alpha cluster states such as the Hoyle state responsible for the production of carbon in red giant stars and point to a connection between nuclear states and the universal physics of bosons at large scattering length.

This work offers rich perspectives. First, for precision nuclear studies, it is mandatoy to include the two-nucleon forces at N^{3}LO as developed here, supplemented by the corresponding contributions of the three-nucleon forces not discussed here. Further, improving the actions by more refined smearing procedures will allow to reduce the constributions from the three- and four-body forces and eventually lead to a precise calculation of the proton and neutron driplines up to the mid-mass region of the nuclear chart.

Bibliography

[1] V. G. J. Stoks et al., *Construction of high-quality NN potential models*,
Phys. Rev. C **49** (1994) p. 2950,
URL: https://link.aps.org/doi/10.1103/PhysRevC.49.2950 (cit. on p. 3).

[2] R. Machleidt, *High-precision, charge-dependent Bonn nucleon-nucleon potential*,
Phys. Rev. C **63** (2001) p. 024001,
URL: https://link.aps.org/doi/10.1103/PhysRevC.63.024001 (cit. on pp. 3, 53, 55).

[3] R. B. Wiringa, V. G. J. Stoks, and R. Schiavilla,
Accurate nucleon-nucleon potential with charge-independence breaking,
Phys. Rev. C **51** (1995) p. 38, URL: https://link.aps.org/doi/10.1103/PhysRevC.51.38
(cit. on p. 3).

[4] S. A. Coon and M. T. Peña, *Momentum and coordinate space three-nucleon potentials*,
Phys. Rev. C **48** (1993) p. 2559,
URL: https://link.aps.org/doi/10.1103/PhysRevC.48.2559 (cit. on p. 3).

[5] B. S. Pudliner et al., *Quantum Monte Carlo calculations of nuclei with $ A< 7$* ,
Phys. Rev. C **56** (1997) p. 1720,
URL: https://link.aps.org/doi/10.1103/PhysRevC.56.1720 (cit. on p. 3).

[6] M. Hoferichter et al.,
Matching Pion-Nucleon Roy-Steiner Equations to Chiral Perturbation Theory,
Phys. Rev. Lett. **115** (2015) p. 192301,
URL: http://link.aps.org/doi/10.1103/PhysRevLett.115.192301
(cit. on pp. 8, 49, 73).

[7] E. Epelbaum, H.-W. Hammer, and U.-G. Meißner, *Modern theory of nuclear forces*, Rev. Mod. Phys. **81** (2009) p. 1773, URL: http://link.aps.org/doi/10.1103/RevModPhys.81.1773 (cit. on pp. 8, 9, 46).

[8] S. Weinberg, *Nuclear forces from chiral Lagrangians*, Phys.Lett. **B251** (1990) p. 288 (cit. on p. 8).

[9] K. G. Wilson, *Confinement of quarks*, Phys. Rev. D **10** (1974) p. 2445, URL: https://link.aps.org/doi/10.1103/PhysRevD.10.2445 (cit. on p. 11).

[10] D. Lee, *Lattice methods and the nuclear few- and many-body problem*, arXiv:1609.00421 [hep-lat, physics:nucl-th] **936** (2017) p. 237, URL: http://arxiv.org/abs/1609.00421 (cit. on p. 24).

[11] E. Epelbaum, *The nucleon-nucleon interaction in a chiral effective field theory*, PhD thesis: University Bochum, 2000 (cit. on p. 27).

[12] P. Reinert, H. Krebs, and E. Epelbaum, *Semilocal momentum-space regularized chiral two-nucleon potentials up to fifth order*, arXiv:1711.08821 [hep-ph, physics:nucl-ex, physics:nucl-th] (2017), arXiv: 1711.08821, URL: http://arxiv.org/abs/1711.08821 (cit. on p. 28).

[13] B. Borasoy et al., *Lattice Simulations for Light Nuclei: Chiral Effective Field Theory at Leading Order*, Eur.Phys.J. **A31** (2007) p. 105 (cit. on pp. 30, 41, 42, 45, 95).

[14] B. Borasoy et al., *Chiral effective field theory on the lattice at next-to-leading order*, Eur.Phys.J. **A35** (2008) p. 343 (cit. on pp. 30, 31, 41, 44, 59, 95).

[15] E. Epelbaum et al., *Lattice calculations for A = 3 , 4, 6, 12 nuclei using chiral effective field theory*, Eur. Phys. J. A **45** (2010) p. 335, ISSN: 1434-6001, 1434-601X, URL: https://link.springer.com/article/10.1140/epja/i2010-11009-x (cit. on pp. 36, 69, 74, 75, 84, 88).

[16] B.-N. Lu et al., *Precise determination of lattice phase shifts and mixing angles*, Physics Letters B **760** (2016) p. 309, ISSN: 0370-2693, URL: http://www.sciencedirect.com/science/article/pii/S0370269316303422 (cit. on pp. 37, 39).

[17] M. Lüscher, *Volume Dependence of the Energy Spectrum in Massive Quantum Field Theories. 1. Stable Particle States*, Commun. Math. Phys. **104** (1986) p. 177 (cit. on p. 37).

[18] M. Lüscher, *Volume Dependence of the Energy Spectrum in Massive Quantum Field Theories. 2. Scattering States*, Commun. Math. Phys. **105** (1986) p. 153 (cit. on p. 37).

[19] M. Lüscher and U. Wolff, *How to calculate the elastic scattering matrix in two-dimensional quantum field theories by numerical simulation*, Nuclear Physics B **339** (1990) p. 222, ISSN: 0550-3213, URL: http://www.sciencedirect.com/science/article/pii/055032139090540T (cit. on p. 37).

[20] M. Lüscher, *Two particle states on a torus and their relation to the scattering matrix*, Nucl. Phys. **B354** (1991) p. 531 (cit. on p. 37).

[21] T. Luu and M. J. Savage, *Extracting Scattering Phase-Shifts in Higher Partial-Waves from Lattice QCD Calculations*, Physical Review D **83** (2011), arXiv: 1101.3347, ISSN: 1550-7998, 1550-2368, URL: http://arxiv.org/abs/1101.3347 (cit. on p. 37).

[22] B. Borasoy et al., *Two-particle scattering on the lattice: Phase shifts, spin-orbit coupling, and mixing angles*, Eur.Phys.J. **A34** (2007) p. 185 (cit. on pp. 37, 38).

[23] H. P. Stapp, T. J. Ypsilantis, and N. Metropolis, *Phase-Shift Analysis of 310-Mev Proton-Proton Scattering Experiments*, Phys. Rev. **105** (1957) p. 302, URL: http://link.aps.org/doi/10.1103/PhysRev.105.302 (cit. on p. 38).

[24] J. Carlson, V. R. Pandharipande, and R. B. Wiringa, *Variational calculations of resonant states in 4He*, Nuclear Physics A **424** (1984) p. 47, ISSN: 0375-9474, URL: http://www.sciencedirect.com/science/article/pii/0375947484901271 (cit. on p. 38).

[25] J. M. Alarcón et al., *Neutron-proton scattering at next-to-next-to-leading order in Nuclear Lattice Effective Field Theory*, Eur. Phys. J. A **53** (2017) p. 83, ISSN: 1434-6001, 1434-601X,

URL: https://link.springer.com/article/10.1140/epja/i2017-12273-x
(cit. on pp. 41, 71).

[26] S. K. Bogner et al., *Is nuclear matter perturbative with low-momentum interactions?*, Nuclear Physics A **763** (2005) p. 59, ISSN: 0375-9474,
URL: http://www.sciencedirect.com/science/article/pii/S0375947405010651
(cit. on p. 41).

[27] N. Klein et al., *Regularization methods for Nuclear Lattice Effective Field Theory*, Physics Letters B **747** (2015) p. 511, ISSN: 0370-2693,
URL: http://www.sciencedirect.com/science/article/pii/S0370269315004621
(cit. on pp. 41, 56, 58, 64, 71, 84).

[28] D. Lee, *Lattice simulations for few- and many-body systems*, Progress in Particle and Nuclear Physics **63** (2009) p. 117, ISSN: 0146-6410,
URL: http://www.sciencedirect.com/science/article/pii/S014664100800094X
(cit. on pp. 42, 45).

[29] B. Borasoy et al.,
Dilute neutron matter on the lattice at next-to-leading order in chiral effective field theory, The European Physical Journal A **35** (2008) p. 357, ISSN: 1434-6001,
URL: http://dx.doi.org/10.1140/epja/i2008-10545-2 (cit. on p. 43).

[30] E. Epelbaum et al., *Ground-state energy of dilute neutron matter at next-to-leading order in lattice chiral effective field theory*, Eur. Phys. J. A **40** (2009) p. 199,
URL: http://dx.doi.org/10.1140/epja/i2009-10755-0 (cit. on p. 43).

[31] E. Epelbaum, W. Glöckle, and U.-G. Meißner,
The two-nucleon system at next-to-next-to-next-to-leading order, Nuclear Physics A **747** (2005) p. 362, ISSN: 0375-9474,
URL: http://www.sciencedirect.com/science/article/pii/S0375947404010747
(cit. on pp. 46, 49, 69, 71).

[32] J. L. Friar and S. Coon,
Non-adiabatic contributions to static two-pion-exchange nuclear potentials, Phys.Rev. **C49** (1994) p. 1272 (cit. on p. 46).

[33] N. Kaiser, R. Brockmann, and W. Weise,
Peripheral nucleon-nucleon phase shifts and chiral symmetry, Nucl.Phys. **A625** (1997) p. 758 (cit. on p. 46).

[34] E. Epelbaum, W. Gloeckle, and U.-G. Meißner,
Improving the convergence of the chiral expansion for nuclear forces. 1. Peripheral phases, Eur. Phys. J. **A19** (2004) p. 125 (cit. on p. 46).

[35] A. Gezerlis et al.,
Quantum Monte Carlo Calculations with Chiral Effective Field Theory Interactions, Phys. Rev. Lett. **111** (2013) p. 032501,
URL: https://link.aps.org/doi/10.1103/PhysRevLett.111.032501 (cit. on p. 46).

[36] A. Gezerlis et al.,
Local chiral effective field theory interactions and quantum Monte Carlo applications, Phys. Rev. C **90** (2014) p. 054323,
URL: https://link.aps.org/doi/10.1103/PhysRevC.90.054323 (cit. on p. 46).

[37] E. Epelbaum, H. Krebs, and U.-G. Meißner,
Improved chiral nucleon-nucleon potential up to next-to-next-to-next-to-leading order, The European Physical Journal A **51** (2015), ISSN: 1434-6001,
URL: http://dx.doi.org/10.1140/epja/i2015-15053-8
(cit. on pp. 46, 50, 55, 61–64, 68, 76, 108).

[38] C. Van Der Leun and C. Alderliesten, *The deuteron binding energy*, Nuclear Physics A **380** (1982) p. 261, ISSN: 0375-9474,
URL: http://www.sciencedirect.com/science/article/pii/0375947482901051
(cit. on p. 53).

[39] E. Epelbaum, H. Krebs, and U.-G. Meißner,
Precision Nucleon-Nucleon Potential at Fifth Order in the Chiral Expansion, Phys. Rev. Lett. **115** (2015) p. 122301,
URL: https://link.aps.org/doi/10.1103/PhysRevLett.115.122301 (cit. on p. 50).

[40] V. G. J. Stoks et al., *Partial-wave analysis of all nucleon-nucleon scattering data below 350 MeV*, Phys. Rev. C **48** (1993) p. 792,
URL: http://link.aps.org/doi/10.1103/PhysRevC.48.792 (cit. on pp. 50, 85, 86).

[41] T. A. Lähde et al., *Lattice effective field theory for medium-mass nuclei*, Physics Letters B **732** (2014) p. 110, ISSN: 0370-2693, URL: http://www.sciencedirect.com/science/article/pii/S0370269314001798 (cit. on pp. 66, 67, 89).

[42] S. Elhatisari et al., *Ab initio calculations of the isotopic dependence of nuclear clustering*, arXiv:1702.05177 [astro-ph, physics:hep-lat, physics:nucl-ex, physics:nucl-th] (2017), URL: http://arxiv.org/abs/1702.05177 (cit. on pp. 69, 70, 73).

[43] S. Elhatisari et al., *Nuclear Binding Near a Quantum Phase Transition*, Phys. Rev. Lett. **117** (2016) p. 132501, URL: https://link.aps.org/doi/10.1103/PhysRevLett.117.132501 (cit. on pp. 69, 81).

[44] D. R. Entem and R. Machleidt, *Accurate charge-dependent nucleon-nucleon potential at fourth order of chiral perturbation theory*, Phys. Rev. C **68** (2003) p. 041001, URL: http://link.aps.org/doi/10.1103/PhysRevC.68.041001 (cit. on p. 71).

[45] E. Epelbaum and U.-G. Meißner, *Isospin-violating nucleon-nucleon forces using the method of unitary transformation*, Phys. Rev. C **72** (2005) p. 044001, URL: https://link.aps.org/doi/10.1103/PhysRevC.72.044001 (cit. on pp. 73, 74).

[46] J. A. Tjon, *Bound states of 4He with local interactions*, Physics Letters B **56** (1975) p. 217, ISSN: 0370-2693, URL: http://www.sciencedirect.com/science/article/pii/0370269375903780 (cit. on p. 88).

[47] A. Nogga, H. Kamada, and W. Glöckle, *Modern Nuclear Force Predictions for the $ \mathit{\ensuremath{\alpha}}$ Particle*, Phys. Rev. Lett. **85** (2000) p. 944, URL: https://link.aps.org/doi/10.1103/PhysRevLett.85.944 (cit. on p. 88).

[48] L. Platter, H.-W. Hammer, and U.-G. Meißner, *On the correlation between the binding energies of the triton and the alpha-particle*, Physics Letters B **607** (2005) p. 254, ISSN: 0370-2693, URL: http://www.sciencedirect.com/science/article/pii/S0370269304017484 (cit. on p. 88).

[49] E. Epelbaum et al., *Lattice Effective Field Theory Calculations for A=3, 4, 6, 12 Nuclei*, Phys. Rev. Lett. **104** (2010) p. 142501, URL: https://link.aps.org/doi/10.1103/PhysRevLett.104.142501 (cit. on p. 88).

[50] T. A. Lähde et al., *Nuclear lattice simulations using symmetry-sign extrapolation*, Eur. Phys. J. A **51** (2015) p. 92, ISSN: 1434-6001, 1434-601X, URL: https://link.springer.com/article/10.1140/epja/i2015-15092-1 (cit. on p. 90).

[51] D. Lee, *Ground-state energy of spin-$\frac12$ fermions in the unitary limit*, Phys. Rev. B **73** (2006) p. 115112, URL: http://link.aps.org/doi/10.1103/PhysRevB.73.115112 (cit. on p. 92).

[52] S. R. Beane et al., *Two nucleons on a lattice*, Physics Letters B **585** (2004) p. 106, ISSN: 0370-2693, URL: http://www.sciencedirect.com/science/article/pii/S0370269304002618 (cit. on p. 92).

[53] R. Navarro Pérez, J. E. Amaro, and E. Ruiz Arriola, *Statistical error analysis for phenomenological nucleon-nucleon potentials*, Phys. Rev. C **89** (2014) p. 064006, URL: https://link.aps.org/doi/10.1103/PhysRevC.89.064006 (cit. on p. 106).

[54] R. T. Birge, *The Calculation of Errors by the Method of Least Squares*, Phys. Rev. **40** (1932) p. 207, URL: https://link.aps.org/doi/10.1103/PhysRev.40.207 (cit. on p. 106).

APPENDIX A

Uncertainty Analysis

From the definition of χ^2 given in Eq. (4.51), we note that χ^2 is a function of the LO and NLO coupling constants

$$\chi^2 \equiv \chi^2(C_{^1\mathrm{S}_0}, C_{^3\mathrm{S}_1}, \widetilde{C}_1, \ldots, \widetilde{C}_7)\,, \tag{A.1}$$

such that if χ^2 is expanded around its minimum, one finds

$$\chi^2 = \chi^2_{\mathrm{min}} + \frac{1}{2}\sum_{i,j} h_{ij}(C_i - C_i^{\mathrm{min}})(C_j - C_j^{\mathrm{min}}) + \ldots\,, \tag{A.2}$$

where the Hessian matrix is given by

$$h_{ij} \equiv \frac{\partial^2 \chi^2}{\partial C_i \partial C_j}\,, \tag{A.3}$$

and C_i^{min} denotes the set of parameters that minimizes the χ^2 function. Given that χ^2 reaches its minimum value for $C_i = C_i^{\mathrm{min}}$, the terms with one derivative vanish. Keeping terms up to second order, we obtain the Hessian approximation to the error (or variance-covariance) matrix

$$\mathcal{E}_{ij} \equiv \frac{1}{2} h^{-1}_{ij}\,, \tag{A.4}$$

and the standard deviations

$$\sigma_i = \sqrt{\sigma_i^2} = \sqrt{\mathcal{E}_{ii}}\,, \tag{A.5}$$

of the fitted constants are obtained from the diagonal elements of the error matrix.

In the absence of systematical errors, we expect to find a normalized chi-square of $\tilde{\chi}^2 \equiv \chi^2/N_{\text{dof}} \approx 1$, where N_{dof} is the number of degrees of freedom (number of fitted data - number of free parameters) in the fit. However, in our analysis $\tilde{\chi}^2 > 1$ in most cases, particularly at LO and for larger values of the lattice spacing a. Such a systematical error suggests that the uncertainties computed from Eq. (A.5) are underestimated. Following Ref. [53], we therefore rescale the input errors by the Birge factor [54], according to

$$\Delta_i \to \Delta_i \sqrt{\tilde{\chi}^2_{\text{min}}}\,, \tag{A.6}$$

which leads to the replacement

$$\chi^2 \to \frac{\chi^2}{\tilde{\chi}^2_{\text{min}}} = N_{\text{dof}} \frac{\chi^2}{\chi^2_{\text{min}}}\,, \tag{A.7}$$

such that $\chi^2/N_{\text{dof}} \approx 1$ for $C_i = C_i^{\text{min}}$. For a given observable O, we assign an uncertainty according to

$$\Delta O \equiv \sqrt{(J_O^T)_i \mathcal{E}_{ij} (J_O)_j}\,, \tag{A.8}$$

where

$$(J_O)_i \equiv \frac{\partial O}{\partial C_i}\,, \tag{A.9}$$

is the Jacobian vector of O with respect to the C_i.

APPENDIX B

Two-Pion Exchange Potential

The chiral expansion of the TPE potential (TPEP) starts at next-to-leading order, The TPEP in momentum space can be decomposed as

$$\begin{aligned} V_{2\pi} &= [V_C + \boldsymbol{\tau}_1 \cdot \boldsymbol{\tau}_2 W_C] + [V_S + \boldsymbol{\tau}_1 \cdot \boldsymbol{\tau}_2 W_S]\, \boldsymbol{\sigma}_1 \cdot \boldsymbol{\sigma}_2 \\ &\quad + [V_T + \boldsymbol{\tau}_1 \cdot \boldsymbol{\tau}_2 W_T]\, \boldsymbol{\sigma}_1 \cdot \mathbf{q}\, \boldsymbol{\sigma}_2 \cdot \mathbf{q} + [V_{LS} + \boldsymbol{\tau}_1 \cdot \boldsymbol{\tau}_2 W_{LS}]\, i\, (\boldsymbol{\sigma}_1 + \boldsymbol{\sigma}_2) \cdot \mathbf{q} \times \mathbf{k}\,. \end{aligned} \tag{B.1}$$

$V_{2\pi}^{(2)}$, which denotes TPEP at NLO, takes the form Eq. (B.1), where

$$W_C^{(2)} = -\frac{L(q)}{384\pi^2 f_\pi^4}\left[4M_\pi^2(5g_A^4 - 4g_A^2 - 1) + q^2(23g_A^4 - 10g_A^2 - 1) + \frac{48 g_A^4 M_\pi^4}{4M_\pi^2 + q^2}\right], \tag{B.2}$$

$$V_T^{(2)} = -\frac{1}{q^2} V_S^{(2)} = -\frac{3g_A^4}{64\pi^2 f_\pi^4} L(q)\,, \tag{B.3}$$

$$V_C^{(2)} = V_{LS}^{(2)} = W_S^{(2)} = W_T^{(2)} = W_{LS}^{(2)} = 0\,. \tag{B.4}$$

The loop function $L(q)$ is defined as

$$L(q) = \frac{\sqrt{4M_\pi^2 + q^2}}{q} \log \frac{\sqrt{4M_\pi^2 + q^2} + q}{2M_\pi}\,. \tag{B.5}$$

As for $V_{2\pi}^{(3)}$, which denotes TPEP at N^{2}LO, we have,

$$V_{\rm C}^{(3)} = -\frac{3g_{\rm A}^2}{16\pi f_\pi^4}[2M_\pi^2(2c_1-c_2)-c_3q^2](2M_\pi^2+q^2)A(q)\,, \tag{B.6}$$

$$W_{\rm T}^{(3)} = -\frac{1}{q^2}W_{\rm S}^{(3)} = -\frac{g_{\rm A}^2}{32\pi f_\pi^4}c_4(4M_\pi^2+q^2)A(q)\,, \tag{B.7}$$

$$V_{\rm S}^{(3)} = V_{\rm T}^{(3)} = V_{\rm LS}^{(3)} = W_{\rm C}^{(3)} = W_{\rm LS}^{(3)} = 0\,, \tag{B.8}$$

with

$$A(q) = \frac{1}{2q}\arctan\frac{q}{2M_\pi}\,, \tag{B.9}$$

where $\mathbf{k} = (\mathbf{p}+\mathbf{p}')/2$, $\boldsymbol{\tau}_i$ denotes the Pauli matrices in isospin space of the nucleon i, and $\boldsymbol{\sigma}_i$ the ones in spin space.

At N^{3}LO, only one-loop bubble diagram (bbl), which has two dimension-three insertions, and two-loop diagram (lp), built from LO insertions only, in the scheme of spectral function regularization, Ref. [37], are taken into account in this work:

$$V_{\rm C}^{(4,{\rm bbl})} = \frac{3}{16\pi^2 f_\pi^4}L(q)\left\{\left[\frac{c_2}{6}(4M_\pi^2+q^2)+c_3(2M_\pi^2+q^2)-4c_1M_\pi^2\right]^2+\frac{c_2^2}{45}(4M_\pi^2+q^2)^2\right\}\,, \tag{B.10}$$

$$W_{\rm T}^{(4,{\rm bbl})} = -\frac{1}{q^2}W_{\rm S}^{(4,{\rm bbl})} = \frac{c_4^2}{96\pi^2 f_\pi^4}(4M_\pi^2+q^2)^2\,; \tag{B.11}$$

and

$$V_{\rm C,S}^{(4,{\rm lp})}(q) = -\frac{2q^6}{\pi}\int_{2M_\pi}^{\infty}{\rm d}\mu\frac{\rho_{\rm C,S}(\mu)}{\mu^5(\mu^2+q^2)}\,, \tag{B.12}$$

$$V_{\rm T}^{(4,{\rm lp})}(q) = \frac{2q^4}{\pi}\int_{2M_\pi}^{\infty}{\rm d}\mu\frac{\rho_{\rm T}(\mu)}{\mu^3(\mu^2+q^2)}\,, \tag{B.13}$$

$$W_{\rm C,S}^{(4,{\rm lp})}(q) = -\frac{2q^6}{\pi}\int_{2M_\pi}^{\infty}{\rm d}\mu\frac{\eta_{\rm C,S}(\mu)}{\mu^5(\mu^2+q^2)}\,, \tag{B.14}$$

$$W_{\rm T}^{(4,{\rm lp})}(q) = \frac{2q^4}{\pi}\int_{2M_\pi}^{\infty}{\rm d}\mu\frac{\eta_{\rm T}(\mu)}{\mu^3(\mu^2+q^2)}\,, \tag{B.15}$$

where ρ_i and η_i denotes the corresponding spectral functions,

$$
\begin{aligned}
\rho_{\rm C}(\mu) &= -\frac{3g_{\rm A}^4(\mu^2-2M_\pi^2)}{\pi\mu(4f_\pi)^6} \\
&\quad\times\left\{(M_\pi^2-2\mu^2)\left[2M_\pi+\frac{2M_\pi^2-\mu^2}{2\mu}\log\frac{\mu+2M_\pi}{\mu-2M_\pi}\right]+4g_{\rm A}^2M_\pi(2M_\pi^2-\mu^2)\right\}\,, \\
\eta_{\rm S}(\mu) &= \mu^2\eta_{\rm T}(\mu) = -\frac{g_{\rm A}^4(\mu^2-4M_\pi^2)}{\pi(4f_\pi)^6}\left\{\left(M_\pi^2-\frac{\mu^2}{4}\right)\log\frac{\mu+2M_\pi}{\mu-2M_\pi}+(1+2g_{\rm A}^2)\mu M_\pi\right\}\,, \\
\rho_{\rm S}(\mu) &= \mu^2\rho_{\rm T}(\mu) = -\left\{\frac{g_{\rm A}^2r^3\mu}{8\pi f_\pi^4}(\bar{d}_{14}-\bar{d}_{15})-\frac{2g_{\rm A}^6\mu r^3}{(8\pi f_\pi^2)^3}\left[\frac{1}{9}-J_1+J_2\right]\right\}\,, \\
\eta_{\rm C}(\mu) &= \left\{\frac{rt^2}{24\pi f_\pi^4\mu}[2(g_{\rm A}^2-1)r^2-3g_{\rm A}^2t^2](\bar{d}_1+\bar{d}_2)+\frac{r^3}{60\pi f_\pi^4\mu}[6(g_{\rm A}^2-1)r^2-5g_{\rm A}^2t^2]\bar{d}_3\right. \\
&\quad-\frac{M_\pi^2r}{6\pi f_\pi^4\mu}[2(g_{\rm A}^2-1)r^2-3g_{\rm A}^2t^2]\bar{d}_5 \\
&\quad-\frac{1}{92160\pi^3{\rm f}_\pi^6\mu^2}[-320(1+2g_{\rm A}^2)^2M_\pi^6+240(1+6g_{\rm A}^2+8g_{\rm A}^4)M_\pi^4\mu^2 \\
&\quad-60g_{\rm A}^2(8+15g_{\rm A}^2)M_\pi^2\mu^4+(-4+29g_{\rm A}^2+122g_{\rm A}^4+3g_{\rm A}^6)\mu^6]\log\frac{2r+\mu}{2M_\pi} \\
&\quad-\frac{r}{2700(8\pi f_\pi^2)^3\mu}\Big[-16(171+2g_{\rm A}^2(1+g_{\rm A}^2)(327+49g_{\rm A}^2))M_\pi^4 \\
&\quad+4(-73+1748g_{\rm A}^2+2549g_{\rm A}^4+726g_{\rm A}^6)M_\pi^2\mu^2-(-64+389g_{\rm A}^2+1782g_{\rm A}^4+1093g_{\rm A}^6)\mu^4\Big] \\
&\quad\left.+\frac{2r}{3(8\pi f_\pi^2)^3\mu}\left[g_{\rm A}^6t^4J_1-2g_{\rm A}^4(2g_{\rm A}^2-1)r^2t^2J_2\right]\right\}\,, \qquad \text{(B.16)}
\end{aligned}
$$

where we have

$$
r=\frac{1}{2}\sqrt{\mu^2-4M_\pi^2}\,,\quad t=\sqrt{\mu^2-2M_\pi^2}\,, \qquad \text{(B.17)}
$$

and

$$
\begin{aligned}
J_1 &= \int_0^1 {\rm d}x\left\{\frac{M_\pi^2}{r^2x^2}-(1+\frac{M_\pi^2}{r^2x^2})^{\frac{3}{2}}\log\frac{rx+\sqrt{M_\pi^2+r^2x^2}}{M_\pi}\right\}\,, \\
J_2 &= \int_0^1 {\rm d}x\,x^2\left\{\frac{M_\pi^2}{r^2x^2}-(1+\frac{M_\pi^2}{r^2x^2})^{\frac{3}{2}}\log\frac{rx+\sqrt{M_\pi^2+r^2x^2}}{M_\pi}\right\}\,. \qquad \text{(B.18)}
\end{aligned}
$$

APPENDIX C

Contact Interactions in Spherical Harmonics Basis in Position Space

We define contact operators in coordinate space for any order. $a_{ij,n}$ and $a^{\dagger}_{ij,n}$ denote the annihilation and creation operators on lattice site n with spin $i = 0, 1$ (up, down) and isospin $j = 0, 1$ (proton, neutron). The pair annihilation operators $[a_n a_{n'}]_{S,S_z;I,I_z}$ read

$$[a_n a_{n'}]_{S,S_z;I,I_z} = \sum_{ii'jj'} a_{ij,n} M_{ii'}(S,S_z) M_{jj'}(I,I_z) a_{i'j',n'} \ . \tag{C.1}$$

The operators P and O take information for total spin, total isospin and orbital angular momentum or total angular momentum of the 2-body system.

$$[P_n]^{2M}_{S,S_z;L,L_z;I,I_z} = [a_n \nabla^{2M} R^{*}_{L,L_z}(\nabla)\, a_n]_{S,S_z;I,I_z} \ , \tag{C.2}$$

$$[O_n]^{2M}_{S,L,J,J_z;I,I_z} = \sum_{S_z L_z} C^{J,J_z}_{L,L_z,S,S_z} [P_n]^{2M}_{S,S_z;L,L_z;I,I_z} \ , \tag{C.3}$$

where R_{L,L_z} is solid harmonics and C^{J,J_z}_{L,L_z,S,S_z} CG coefficients. The zero-ranged contact potential with quantum numbers $(J, S, I, L_\mathrm{i}, L_\mathrm{o}, m_\mathrm{i}, m_\mathrm{o})$ at order Q^{2N} in position space is built as

$$[V_{2N}]^{\{2m_\mathrm{o},2m_\mathrm{i}\}}_{2S+1(L_\mathrm{i}L_\mathrm{o})_J,I}(J_z,I_z) = \frac{1}{2}\left[O^{2m_\mathrm{o}}_{S,L_\mathrm{o},J,J_z;I,I_z}\right]^{\dagger} O^{2m_\mathrm{i}}_{S,L_\mathrm{i},J,J_z;I,I_z} + \frac{1}{2}\left\{(L_\mathrm{o},m_\mathrm{o}) \leftrightarrow (L_\mathrm{i},m_\mathrm{i})\right\} \ . \tag{C.4}$$

Operators at Order Q^0

S-wave spin singlet, $V^{(0)}_{^1\mathrm{S}_0}$,

$$[V_0]^{\{0,0\}}_{^1\mathrm{S}_0,1}(0,I_z) = \left[O^0_{0,0,0,0;1,I_z}\right]^\dagger O^0_{0,0,0,0;1,I_z} \tag{C.5}$$

S-wave spin triplet, $V^{(0)}_{^3\mathrm{S}_1}$,

$$[V_0]^{\{0,0\}}_{^3\mathrm{S}_1,0}(J_z,0) = \left[O^0_{1,0,1,J_z;0,0}\right]^\dagger O^0_{1,0,1,J_z;0,0} \tag{C.6}$$

Operators at Order Q^2

S-wave spin singlet, $V^{(2)}_{^1\mathrm{S}_0}$,

$$[V_2]^{\{2,0\}}_{^1\mathrm{S}_0,1}(0,I_z) = \frac{1}{2}\left[O^2_{0,0,0,0;1,I_z}\right]^\dagger O^0_{0,0,0,0;1,I_z} + \frac{1}{2}\left[O^0_{0,0,0,0;1,I_z}\right]^\dagger O^2_{0,0,0,0;1,I_z} \tag{C.7}$$

S-wave spin triplet, $V^{(2)}_{^3\mathrm{S}_1}$,

$$[V_2]^{\{2,0\}}_{^3\mathrm{S}_1,0}(J_z,0) = \frac{1}{2}\left[O^2_{1,0,1,J_z;0,0}\right]^\dagger O^0_{1,0,1,J_z;0,0} + \frac{1}{2}\left[O^0_{1,0,1,J_z;0,0}\right]^\dagger O^2_{1,0,1,J_z;0,0} \tag{C.8}$$

P-wave spin singlet, $V^{(2)}_{^1\mathrm{P}_1}$,

$$[V_2]^{\{0,0\}}_{^1\mathrm{P}_1,0}(J_z,0) = \left[O^0_{0,1,1,J_z;0,0}\right]^\dagger O^0_{0,1,1,J_z;0,0} \tag{C.9}$$

P-wave spin triplet, $V^{(2)}_{^3\mathrm{P}_0}$, $V^{(2)}_{^3\mathrm{P}_1}$, $V^{(2)}_{^3\mathrm{P}_3}$,

$$[V_2]^{\{0,0\}}_{^3\mathrm{P}_0,1}(0,I_z) = \left[O^0_{1,1,0,0;1,I_z}\right]^\dagger O^0_{1,1,0,0;1,I_z} \tag{C.10}$$

$$[V_2]^{\{0,0\}}_{^3\mathrm{P}_1,1}(J_z,I_z) = \left[O^0_{1,1,1,J_z;1,I_z}\right]^\dagger O^0_{1,1,1,J_z;1,I_z} \tag{C.11}$$

$$[V_2]^{\{0,0\}}_{^3\mathrm{P}_2,1}(J_z,I_z) = \left[O^0_{1,1,2,J_z;1,I_z}\right]^\dagger O^0_{1,1,2,J_z;1,I_z} \tag{C.12}$$

SD-wave mixing channel, $V^{(2)}_{^3\mathrm{SD}_1}$,

$$[V_2]^{\{0,0\}}_{^3\mathrm{SD}_1,0}(J_z,0) = \frac{1}{2}\left[O^0_{1,0,1,J_z;0,0}\right]^\dagger O^0_{1,2,1,J_z;0,0} + \frac{1}{2}\left[O^0_{1,2,1,J_z;0,0}\right]^\dagger O^0_{1,0,1,J_z;0,0} \tag{C.13}$$

Operators at Order Q^4

S-wave spin singlet, $V^{(4)}_{^1\mathrm{S}_0;1}$, $V^{(4)}_{^1\mathrm{S}_0;2}$

$$[V_4]^{\{4,0\}}_{^1\mathrm{S}_0,1;1}(0,I_z) = \frac{1}{2}\left[O^4_{0,0,0,0;1,I_z}\right]^\dagger O^0_{0,0,0,0;1,I_z} + \frac{1}{2}\left[O^0_{0,0,0,0;1,I_z}\right]^\dagger O^4_{0,0,0,0;1,I_z} \tag{C.14}$$

$$[V_4]^{\{2,2\}}_{^1\mathrm{S}_0,1;2}(0,I_z) = \left[O^2_{0,0,0,0;1,I_z}\right]^\dagger O^2_{0,0,0,0;1,I_z} \tag{C.15}$$

S-wave spin triplet, $V^{(4)}_{^3\mathrm{S}_1;1}$, $V^{(4)}_{^3\mathrm{S}_1;2}$,

$$[V_4]^{\{4,0\}}_{^3\mathrm{S}_1,0;1}(J_z,0) = \frac{1}{2}\left[O^4_{1,0,1,J_z;0,0}\right]^\dagger O^0_{1,0,1,J_z;0,0} + \frac{1}{2}\left[O^0_{1,0,1,J_z;0,0}\right]^\dagger O^4_{1,0,1,J_z;0,0} \tag{C.16}$$

$$[V_4]^{\{2,2\}}_{^3\mathrm{S}_1,0;2}(J_z,0) = \left[O^2_{1,0,1,J_z;0,0}\right]^\dagger O^2_{1,0,1,J_z;0,0} \tag{C.17}$$

P-wave spin singlet, $V^{(4)}_{^1\mathrm{P}_1}$,

$$[V_4]^{\{2,0\}}_{^1\mathrm{P}_1,0}(J_z,0) = \frac{1}{2}\left[O^2_{0,1,1,J_z;0,0}\right]^\dagger O^0_{0,1,1,J_z;0,0} + \frac{1}{2}\left[O^0_{0,1,1,J_z;0,0}\right]^\dagger O^2_{0,1,1,J_z;0,0} \tag{C.18}$$

P-wave spin triplet, $V^{(4)}_{^3\mathrm{P}_0}$, $V^{(4)}_{^3\mathrm{P}_1}$, $V^{(4)}_{^3\mathrm{P}_2}$,

$$[V_4]^{\{2,0\}}_{^3\mathrm{P}_0,1}(0,I_z) = \frac{1}{2}\left[O^2_{1,1,0,0;I,I_z}\right]^\dagger O^0_{1,1,0,0;I,I_z} + \frac{1}{2}\left[O^0_{1,1,0,0;I,I_z}\right]^\dagger O^2_{1,1,0,0;I,I_z} \tag{C.19}$$

$$[V_4]^{\{2,0\}}_{^3\mathrm{P}_1,1}(J_z,I_z) = \frac{1}{2}\left[O^2_{1,1,1,J_z;I,I_z}\right]^\dagger O^0_{1,1,1,J_z;I,I_z} + \frac{1}{2}\left[O^0_{1,1,1,J_z;I,I_z}\right]^\dagger O^2_{1,1,1,J_z;I,I_z} \tag{C.20}$$

$$[V_4]^{\{2,0\}}_{^3\mathrm{P}_2,1}(J_z,I_z) = \frac{1}{2}\left[O^2_{1,1,2,J_z;I,I_z}\right]^\dagger O^0_{1,1,2,J_z;I,I_z} + \frac{1}{2}\left[O^0_{1,1,2,J_z;I,I_z}\right]^\dagger O^2_{1,1,2,J_z;I,I_z} \tag{C.21}$$

D-wave spin singlet, $V^{(4)}_{^1\mathrm{D}_2}$,

$$[V_4]^{\{0,0\}}_{^1\mathrm{D}_2,1}(J_z,0) = \left[O^0_{0,2,2,J_z;1,I_z}\right]^\dagger O^0_{0,2,2,J_z;1,I_z} \tag{C.22}$$

D-wave spin triplet, $V^{(4)}_{^3\mathrm{D}_1}$, $V^{(4)}_{^3\mathrm{D}_2}$, $V^{(4)}_{^3\mathrm{D}_3}$,

$$[V_4]^{\{0,0\}}_{^3\mathrm{D}_1,0}(J_z,0) = \left[O^0_{1,2,1,J_z;0,0}\right]^\dagger O^0_{1,2,1,J_z;0,0} \tag{C.23}$$

$$[V_4]^{\{0,0\}}_{^3\mathrm{D}_2,0}(J_z,0) = \left[O^0_{1,2,2,J_z;0,0}\right]^\dagger O^0_{1,2,2,J_z;0,0} \tag{C.24}$$

$$[V_4]^{\{0,0\}}_{^3\mathrm{D}_3,0}(J_z,0) = \left[O^0_{1,2,3,J_z;0,0}\right]^\dagger O^0_{1,2,3,J_z;0,0} \tag{C.25}$$

SD-wave mixing channel, $V^{(4)}_{^3\mathrm{SD}_1;1}$, $V^{(4)}_{^3\mathrm{SD}_1;2}$

$$[V_4]^{\{2,0\}}_{^3\mathrm{SD}_1,0;1}(J_z,0) = \frac{1}{2}\left[O^2_{1,0,1,J_z;0,0}\right]^\dagger O^0_{1,2,1,J_z;0,0} + \frac{1}{2}\left[O^0_{1,2,1,J_z;0,0}\right]^\dagger O^2_{1,0,1,J_z;0,0} \tag{C.26}$$

$$[V_4]^{\{0,2\}}_{^3\mathrm{SD}_1,0;2}(J_z,0) = \frac{1}{2}\left[O^0_{1,0,1,J_z;0,0}\right]^\dagger O^2_{1,2,1,J_z;0,0} + \frac{1}{2}\left[O^2_{1,2,1,J_z;0,0}\right]^\dagger O^0_{1,0,1,J_z;0,0} \tag{C.27}$$

PF-wave mixing channel, $V^{(4)}_{^3\mathrm{PF}_2}$,

$$[V_4]^{\{0,0\}}_{^3\mathrm{PF}_2,1}(J_z,I_z) = \left[O^0_{1,1,2,J_z;1,I_z}\right]^\dagger O^0_{1,3,2,J_z;1,I_z} \tag{C.28}$$

List of Figures

2.1 Chiral expansion of the two-nucleon force. Here solid/dashed lines denote nucleons/pions. The interactions of different dimensions are depicted by different symbols, see Ref. [7] for details. 9

3.1 Worldline description of the interaction of four nucleons with explicit pion exchanges and contact interactions. 25

3.2 Worldline description in erms of auxiliary fields. As can be seen, such a description is particularly suited for paralell computing. 25

3.3 (a)spherical wall (b)Auxiliary potential for the improved spherical wall as described in the text. 39

4.1 Phase shifts and mixing angles for np scattering up to N^2LO in NLEFT, for our smallest (spatial) lattice spacing of $a = 0.98$ fm $= (200\ \text{MeV})^{-1}$ and a temporal lattice spacing $a_t = (600\ \text{MeV})^{-1}$. The (blue) squares, (green) circles and (red) triangles denote LO, NLO and N^2LO results, respectively. The NPWA is shown by the solid black line. . . 54

4.2 Phase shifts and mixing angles for np scattering up to N^2LO in NLEFT, for $a = 1.32$ fm $= (150\ \text{MeV})^{-1}$. For notations, see Fig. 4.1. 55

4.3 Phase shifts and mixing angles for np scattering up to N^2LO in NLEFT, for $a = 1.64$ fm $= (120\ \text{MeV})^{-1}$. For notations, see Fig. 4.1. 56

4.4 Phase shifts and mixing angles for np scattering up to N^2LO in NLEFT, for a (spatial) lattice spacing $a = 1.97$ fm $= (100\ \text{MeV})^{-1}$ and a temporal lattice spacing $a_t = (150\ \text{MeV})^{-1}$. For notations, see Fig. 4.1. 57

4.5 Fitted LO + perturbative NLO/N^{2}LO np phase shifts and mixing angles for $a = 1.97$ fm. The shaded bands denote the continuum results of Ref. [37], and the NPWA is given by the black line. 61

4.6 Fitted LO + perturbative NLO/N^{2}LO np phase shifts and mixing angles for $a = 1.64$ fm. The shaded bands denote the continuum results of Ref. [37], and the NPWA is given by the black line. 62

4.7 Fitted LO + perturbative NLO/N^{2}LO np phase shifts and mixing angles for $a = 1.32$ fm. The shaded bands denote the continuum results of Ref. [37], and the NPWA is given by the black line. 63

4.8 Fitted LO + perturbative NLO/N^{2}LO np phase shifts and mixing angles for $a = 1.97$ fm including the improved OPE. The shaded bands denote the continuum results of Ref. [37], and the NPWA is given by the black line. 68

5.1 Phase shifts for np scattering at LO (downward blue triangles), NLO (red crosses), N^{2}LO (green triangles), N^{3}LO (magenta stars) as a function of CM momentum. The NPWA results are shown by the solid (yellow) curves. 78

5.2 Phase shifts for the low partial waves of pp scattering at LO (downward blue triangles), NLO (red crosses), N^{2}LO (green triangles), N^{3}LO (magenta stars) as a function of CM momentum. The NPWA results are shown by the solid (yellow) curves. 80

6.1 Nucleon-nucleon scattering phase shifts. We plot LO lattice phase shifts for proton-neutron scattering versus the center-of-mass relative momentum for interactions A (red triangles) and B (blue squares). For comparison we also plot the phase shifts extracted from the Nijmegen PWA, Ref. [40] (black lines) and a continuum version of interaction A (green dashed lines). In the first row, the data in panels **a**, **b**,**c**,**d** correspond to $^1S_0$, $^3S_1$, $^1P_1$, $^3P_0$ respectively. In the second row, panels **e**,**f**,**g**,**h** correspond to $^3P_1$, $^3P_2$, $^1D_2$, $^3D_1$ respectively. In the third row, panels **i**, **j**,**k**,**l** correspond to $^3D_2$, $^3D_3$, ε_1, ε_2 respectively. 86

6.2 Energy versus projection time for ^{3}H,^{3}He, and ^{4}He. In panels **a** and **b** we plot the energy versus projection time $t = L_t a_t$ for ^{3}He and ^{4}He respectively for the LO interaction A (blue plus signs and dashed lines), LO interaction B (red squares and dashed lines), LO + Coulomb interaction A (blue crosses and solid lines), and LO + Coulomb interaction B (red triangles and solid lines). The LO and LO + Coulomb results ^{3}H are the same as the LO results for ^{3}He. The error bars indicate one standard deviation errors from the stochastic noise of the MC simulations, and the lines show extrapolations to infinite projection time. 88

6.3 Energy versus projection time for ^{8}Be,^{12}C,^{16}O, and ^{20}Ne. In panels **a**,**b**,**c**,**d** we plot the energy versus projection time $t = L_t a_t$ for ^{8}Be, ^{12}C, ^{16}O, and ^{20}Ne respectively for the LO interaction A (blue plus signs and dashed lines), LO interaction B (red squares and dashed lines), LO + Coulomb interaction A (blue crosses and solid lines), and LO + Coulomb interaction B (red triangles and solid lines). The error bars indicate one standard deviation errors from the stochastic noise of the MC simulations, and the lines show extrapolations to infinite projection time. 90

6.4 Ground state energies versus λ. We plot the LO ground state energies $E_{^4\mathrm{He}}$, 1/2 $E_{^8\mathrm{Be}}$, 1/3 $E_{^{12}\mathrm{C}}$, 1/4 $E_{^{16}\mathrm{O}}$, 1/5 $E_{^{20}\mathrm{Ne}}$ versus the parameter λ which interpolates between V_{A} and V_{B}. 92

List of Tables

3.1 Hopping coefficients ω_j and θ_j for ν-order of finite difference 13

3.2 Operator basis for the contact interactions at various orders. 36

4.1 Summary of lattice spacings a (spatial) and a_t (temporal) and box dimensions L. The physical spatial lattice volume V is kept constant at $(La)^3 \simeq (63\ \mathrm{fm})^3$. 49

4.2 Summary of the fitting procedure, indicating which parameters are fitted to what scattering channel at each order in NLEFT, and the resulting χ^2/N_{dof} (for $a = 0.98$ fm). 50

4.3 Fitted constants and low-energy parameters for $a = 0.98$ fm. The LO constants $C_{^1\mathrm{S}_0}$ and $C_{^3\mathrm{S}_1}$ are given in units of $[10^{-4}\ \mathrm{MeV}^{-2}]$, and the C_i of the NLO interaction in units of $[10^{-8}\ \mathrm{MeV}^{-4}]$. Due to the large lattice ($L = 64$) for $a = 0.98$ fm, an uncertainty analysis using the variance-covariance matrix as in Table 4.4 was numerically unfeasible. Hence, an estimated uncertainty of 2% has been assigned, which is consistent with the uncertainties for larger a. For entries with a dagger (†), the deuteron energy E_d has been included as an additional constraint. 51

4.4 Fitted constants and low-energy S-wave parameters for $a = 0.98$ fm. The LO constants $C_{^1\mathrm{S}_0}$ and $C_{^3\mathrm{S}_1}$ are given in units of $[10^{-4}\ \mathrm{MeV}^{-2}]$, and the C_i of the NLO interaction in units of $[10^{-8}\ \mathrm{MeV}^{-4}]$. The smearing parameter b_s of the LO contact interactions is determined by the LO fit, and thereafter kept fixed at NLO and N^{2}LO. The values in parentheses are the uncertainties calculated using the variance-covariance matrix according to Eq. (A.5). 52

4.5 Low-energy S-wave parameters, as a function of the lattice spacing a and the order of the NLEFT expansion. E_d is the deuteron binding energy, and the a_i and r_i denote the scattering lengths and effective ranges in channel i. The experimental value of E_d is from Ref. [38], and the scattering lengths and effective ranges are from Ref. [2]. For entries marked with a dagger (†), the empirical deuteron energy E_d has been included in the fit as an additional constraint. 53

4.6 Summary of fit results (in units of a) for the perturbative NLO+N^{2}LO analysis at $a = 1.97$ fm. Fitted values of E_d are indicated by a dagger (†). Note that the values of $C_{^1\mathrm{S}_0}$, $C_{^3\mathrm{S}_1}$ and b_s are fixed by the LO fit. 58

4.7 Summary of fit results (in units of a) for the perturbative NLO+N^{2}LO analysis at $a = 1.64$ fm. Notation as in Table 4.6. 59

4.8 Summary of fit results (in units of a) for the perturbative NLO+N^{2}LO analysis at $a = 1.32$ fm. Notation as in Table 4.6. 60

4.9 Summary of fit results with perturbatively improved OPE (in units of a) for the perturbative NLO+N^{2}LO analysis at $a = 1.97$ fm. Notation as in Table 4.6. 65

4.10 Nuclear binding energies with 2N forces up to N^{2}LO in the NLEFT expansion for $a = 1.97$ fm, data taken from Ref. [41]. The first parenthesis gives the estimated Monte Carlo error in the calculation of $E_B^{\mathrm{N^2LO}}$, and the second parenthesis the error due to variance-covariance matrix in Eq. (4.63). For reference, we also show the experimental binding energies. 67

5.1 LECs for np scattering at NLO, N^{2}LO, and N^{3}LO. The values of LECs at LO, NLO, N^{3}LO, are given in units of [10^{-4}MeV^{-2}], [10^{-8}MeV^{-4}], [10^{-12}MeV^{-6}], respectively. 77

5.2 LECs for pp scattering at NLO, N^{2}LO, and N^{3}LO. The values of LECs at LO, NLO, N^{3}LO, are given in units of [10^{-4}MeV^{-2}], [10^{-8}MeV^{-4}], [10^{-12}MeV^{-6}], respectively. 79

6.1 Ground state energies of ^{3}H, ^{3}He, ^{4}He, ^{8}Be, ^{12}C, ^{16}O, ^{20}Ne for interactions A and B. We show LO results, LO + Coulomb results, and experimental data. All energies are in units of MeV. The error bars denote one standard deviation errors. 93

Acronyms

χEFT chiral effective field theory. 2, 3, 8, 9, 11, 13, 19, 21, 23, 24, 27, 28, 46, 64, 65, 69

χPT chiral perturbation theory. 13

χ^2 chi-square. 41

3N three-nucleon. 67, 88

3PE three-pion exchange. 69

CG Clebsch-Gordan. 34, 111

CM center-of-mass. 2, 22, 27, 37

CT contact term / contact operator / contact interaction. 23, 25–27, 34, 35, 41, 44, 46, 63, 65, 74, 75

DR dimensional regularization. 46, 48, 49

EFT effective field theory. 2, 3, 9, 11, 41, 46

GTR Goldberger-Treiman relation. 49, 70, 82

HMC hybrid Monte Carlo. 2

IB isospin-breaking. 3, 46, 73, 74, 82, 87

LEC low-energy constant. 8, 10, 41, 45, 48, 49, 60, 64, 69, 72, 76, 95

LO leading order. 3, 8, 10, 13, 19, 23, 24, 26–29, 35, 41, 43, 45, 46, 50, 51, 53–56, 59–62, 64–67, 69, 73, 76, 80–82, 84–89, 91, 92, 95, 105, 106, 108, 116

MC Monte Carlo. 1–3, 29, 59, 62, 65–67, 81, 85, 87–90, 95, 96, 117

N^{2}LO next-to-next-to-leading order / NNLO. 3, 9, 28, 41, 45, 46, 48–55, 59, 60, 64–67, 80, 85, 89, 95, 108, 116

N^{3}LO next-to-next-to-next-to-leading order / NNNLO. 3, 27, 28, 32, 58, 69, 71, 76, 80, 96, 108, 116

NCSM no-core shell model. 3

NLO next-to-leading order. 8, 27, 28, 31, 41, 44–47, 49–51, 53–55, 59, 60, 62–66, 73, 76, 80, 85, 105, 107, 116

NN nucleon-nucleon / 2N / two-nucleon. 10, 21, 25, 26, 33, 36, 37, 41, 42, 44, 46, 50, 51, 56, 58, 64, 67, 69, 89

np neutron-proton. 2, 3, 41, 49, 52, 57, 58, 69, 75, 76

OPE one-pion exchange. 2, 10, 19, 41, 45, 46, 54, 61–66, 71, 74, 84, 85, 91

pp proton-proton. 3, 69, 74–76

PWA partial wave analysis. 46, 50, 54, 58, 61, 63, 64, 66, 85

QCD quantum chromodynamics. 1, 2, 5, 8, 11–13, 37

QFT quantum field theory. 11

SFR spectral function regularization. 46

SM standard model. 5, 11

TPE two-pion exchange. 2, 41, 45, 46, 48, 49, 51, 53, 60, 63–66, 69, 71, 72, 74, 76, 95, 96, 107

UV ultraviolet. 46

Acknowledgements

I would like to give my grateful acknowledgment to Prof. Dr. Ulf-G. Meißner, who provided me this position in FZJ to pursue a Ph.D. He always enlightened me with his in-depth knowledge and insights on science when I was a beginner in the field of the research. His rigorous academic style and scientific spirit of suspicion benefited me throughout my Ph.D. study. I am deeply indebted to my second supervisor, Prof. Dr. Thomas Luu, who encouraged and pushed me to finish the thesis when I fell into the dull work and felt frustrated, and gave me suggestions to modify my thesis patiently. Without his persistent inspiration, it might take more months to produce this dissertation.

I would like to acknowledge instructive discussions with all of the collaborators in this subject. Prof. Dr. Dean Lee always brought an avalanche of promising and enlightening ideas when he visited Germany. It made me inspired and excited to talk with him. He always provided unique perspectives and brand new features to address the old-fashioned topics. I am grateful to Dr. Bing-nan Lu, who always gave me useful guidance to revisit the underlying physics when I encountered difficulties and confusion. Thanks to Dr. Ning Li, who helped me to check codes to perform the final simulation in the research. Thanks to Dr. Timo Lähde, who is a skillful programmer, for giving me advice when I started to realize the ideas into scientific results.

I would like to thank my colleagues and friends who concerned me. They helped me a lot in work and in my life and brought me joyful moments.

I give my gratitude to my parents, the ones who concern me about health and happiness. They are the solid foundation of my persistence. They make me tough in the past, present, and future.

Publications of important parts of the dissertation

Published journal articles

- “Nuclear Binding Near a Quantum Phase Transition”,
  Serdar Elhatisari, Ning Li, Alexander Rokash, Jose Manuel Alarcón, **Dechuan Du**, Nico Klein, Bing-nan Lu, Ulf-G. Meißner, Evgeny Epelbaum, Hermann Krebs, Timo A. Lähde, Dean Lee, and Gautam Rupak,
  Phys. Rev. Lett. 117, 132501 (2016);

- “Neutron-proton scattering at next-to-next-to-leading order in Nuclear Lattice Effective Field Theory”,
  Jose Manuel Alarcón, **Dechuan Du**, Nico Klein, Timo A. Lähde, Dean Lee, Ning Li, Bing-Nan Lu, Thomas Luu, Ulf-G. Meißner,
  Eur. Phys. J. A 53 (2017) 83.